

Air Force Institute of Technology

AFIT Scholar

Theses and Dissertations

Student Graduate Works

3-12-2007

A Study of Bi-Directional Reflectance Distribution Functions and Their Effects on Infrared Signature Models

Samuel I. Harkiss

Follow this and additional works at: <https://scholar.afit.edu/etd>



Part of the [Optics Commons](#)

Recommended Citation

Harkiss, Samuel I., "A Study of Bi-Directional Reflectance Distribution Functions and Their Effects on Infrared Signature Models" (2007). *Theses and Dissertations*. 2915.

<https://scholar.afit.edu/etd/2915>

This Thesis is brought to you for free and open access by the Student Graduate Works at AFIT Scholar. It has been accepted for inclusion in Theses and Dissertations by an authorized administrator of AFIT Scholar. For more information, please contact richard.mansfield@afit.edu.



**A STUDY OF
BI-DIRECTIONAL REFLECTANCE DISTRIBUTION FUNCTIONS
AND THEIR EFFECT ON
INFRARED SIGNATURE MODELS**

THESIS

Samuel I. Harkiss, Flight Lieutenant, RAAF

AFIT/GE/ENP/07-01

**DEPARTMENT OF THE AIR FORCE
AIR UNIVERSITY**

AIR FORCE INSTITUTE OF TECHNOLOGY

Wright-Patterson Air Force Base, Ohio

APPROVED FOR PUBLIC RELEASE; DISTRIBUTION UNLIMITED.

The views expressed in this thesis are those of the author and do not reflect the official policy or position of the United States Air Force, Department of Defense, the United States Government, Royal Australian Air Force, Australian Department of Defence, or Government of the Commonwealth of Australia.

AFIT/GE/ENP/07-01

A STUDY OF
BI-DIRECTIONAL REFLECTANCE DISTRIBUTION FUNCTIONS
AND THEIR EFFECT ON
INFRARED SIGNATURE MODELS

THESIS

Presented to the Faculty
Department of Engineering Physics
Graduate School of Engineering and Management
Air Force Institute of Technology
Air University
Air Education and Training Command
In Partial Fulfillment of the Requirements for the
Degree of Master of Science in Electrical Engineering

Samuel I. Harkiss, BE(Elec)(Hons)
Flight Lieutenant, RAAF

March 2007

APPROVED FOR PUBLIC RELEASE; DISTRIBUTION UNLIMITED.

A STUDY OF
BI-DIRECTIONAL REFLECTANCE DISTRIBUTION FUNCTIONS
AND THEIR EFFECT ON
INFRARED SIGNATURE MODELS

Samuel I. Harkiss, BE(Elec)(Hons)
Flight Lieutenant, RAAF

Approved:



Michael A. Marciniak (Chairman)

7 Mar 07

Date



Stephen C. Cain (Member)

9 March 2007

Date



Robert L. Hengehold (Member)

12 Mar '07

Date

Abstract

Since 2004, AFIT has been developing a trend-analysis tool to assess large commercial aircraft infrared (LCAIR) signatures. In many cases, this code predicted signatures to within 10% of measured data. However, other results indicated that the single-bounce, specular-reflection algorithm being used failed to adequately simulate interactions between aircraft parts where either the specular component is dominated by diffuse reflection or part-to-part multiple-bounce reflections contribute significantly to the signature; discrepancies greater than 100% were observed. This research incorporates Bi-Directional Reflectance Distribution Functions (BRDF's) and multiple-bounce calculations into the LCAIR model.

A physical aircraft model was constructed from aluminum, and measurements were taken before and after a surface treatment in gloss black paint. The Sandford-Robertson model is used to parameterize the BRDF's of both the bare aluminum and gloss black paint. Since the most efficient method of integrating a BRDF depends upon the reflectance distribution of the aircraft material, the sampling resolution of the BRDF integral is crucial to an accurate simulation. Additionally, care is taken to ensure that the integration of the hemispherical irradiance onto each facet of the computational model is sampled at a sufficient resolution to achieve convergence in the solution.

Simulations in the mid-wave infrared (MWIR) and long-wave infrared (LWIR) bands validate both the previous specular reflectance simplification for the gloss black simulations and the failure of the previous algorithm for the highly reflective bare aluminum. The necessity of considering multiple bounces in the simulation is also demonstrated amongst part-to-part reflections near the wing root, where three or four bounces are required for the solution to converge.

Finally, three scenarios simulating a man-portable air defence system (MANPADS) system engaging an Airbus A340-300 aircraft landing at a generic airport are performed. The infrared signature of the aircraft is contrasted against the background over the detector's field of view. An irradiance at the detector's optic is calculated for the MWIR and LWIR bands. A maximum noise equivalent irradiance (NEI) of $5 \times 10^{-5} \text{ W/m}^2$ is found to be required to ensure that the MANPADS is able to detect and track the aircraft. An NEI larger than this will prevent the system from detecting the aircraft.

Acknowledgements

I would like to thank everyone who has helped me with ideas, technical tips and subject matter expertise, however, I must single out my advisor Dr. Michael Marciniak who provided guidance and a wealth of knowledge. He was able to guide me around obstacles with only pencil and paper, making my previous hours of toil seem childish.

Additionally, I would like to thank everyone that has made my stay in the US enjoyable, through helping Stacey and myself to integrate into the US Air Force community. Spending nearly two years overseas can be tough, but everyone has been very helpful, and sociable.

Finally, I would like to thank Stacey for her patience and understanding, especially when it seemed like I lived at work and only came home for a few hours a day. A daily routine and normal sleep patterns will return soon!

Samuel I. Harkiss

Table of Contents

	Page
Abstract	iv
Acknowledgements	vi
List of Figures	xi
List of Tables	xv
List of Symbols	xvi
List of Abbreviations	xviii
I. Introduction	1
1.1 Infrared Spectrum	1
1.2 The MANPADS Threat	2
1.3 Problem Description	3
1.3.1 Purpose	3
1.4 Thesis Overview	3
1.5 Literature Review	4
II. Background	6
2.1 Blackbody Radiation	6
2.1.1 Reflectance	7
2.1.2 Emissivity	7
2.2 Radiometry	7
2.3 Bi-Directional Reflectance Distribution Function	8
2.3.1 Dimensionality Reduction	10
2.3.2 Integral Forms of the BRDF	11
2.3.3 Surface Reflectance Distributions	12
2.3.4 Sandford-Robertson Reflectance Model	15
2.3.5 Bare Aluminum Material	18
2.3.6 Gloss Black Painted Aluminum Material	19
2.4 Atmospheric Transmission	26

	Page
2.5	Monte Carlo Integration 27
2.5.1	Numerical Quadrature 27
2.5.2	Monte Carlo Method 29
2.5.3	2-Dimensional Monte Carlo Integration 30
2.5.4	Monte Carlo Integration Example 30
2.6	Spherical and Hemispherical Geometry 30
2.6.1	Hemispherical Integration 31
2.7	Chapter Summary 32
III.	Development of the Infrared Signature Simulation 33
3.1	Infrared Signature Components 33
3.2	Aircraft Model 33
3.2.1	Wireframe Model 34
3.2.2	Blender 3D Program 36
3.2.3	Simulation Models 38
3.2.4	Hemispherical View 44
3.3	Integrating the BRDF 45
3.3.1	Importance Sampled Integration 50
3.3.2	Monte Carlo Integration 52
3.3.3	Stratified Numerical Quadrature 54
3.3.4	Geometry Sampling 55
3.4	Background Construction 57
3.4.1	IR Range 57
3.4.2	World Sphere 58
3.5	Emission and Propagation Algorithms 66
3.5.1	Specular Reflection Assumption 70
3.5.2	Radiosity 70
3.5.3	Point-Of-View Hemispherical Integration 73
3.5.4	Point-Of-View Monte Carlo Hemispherical Integration 73
3.5.5	Point-Of-View Stratified Hemispherical Integration 73
3.5.6	Memory Considerations 76
3.6	Artificial Cavity Blackbody Source Simulation 76

	Page
3.7	A340-300 Simulation Output 79
3.8	Exercising the Model 79
3.8.1	Contrast Detection 80
3.8.2	Flight Path 82
3.8.3	Aircraft Engagement Positions 82
3.9	Chapter Summary 83
IV.	Results and Analysis 84
4.1	Artificial Cavity Blackbody Source Simulations 84
4.2	IR Range Simulations 86
4.2.1	Single Bounce and Specular Reflectance 86
4.2.2	Multiple Bounces and Specular Reflectance 90
4.2.3	Single Bounce and Integrated BRDF 93
4.2.4	Multiple Bounces and Integrated BRDF 95
4.2.5	Algorithm of Choice 95
4.3	A340-300 Simulations 98
4.3.1	Position 1 - MWIR 99
4.3.2	Position 1 - LWIR 102
4.3.3	Position 2 108
4.3.4	Position 3 108
4.3.5	A340-300 Simulation Summary 111
4.4	Chapter Summary 111
V.	Conclusions and Recommendations 116
5.1	LCAIR Algorithm Summary 116
5.2	Lessons Learned 117
5.3	Recommendations for Future Work 118
5.4	Conclusion 119
Appendix A.	Simple Geometric Analytical Proofs 120
A.1	Two Plates 120
A.2	Open Box with Rear Wall Emitting 122

	Page
Appendix B. Blackbody Cavity Source Calculations	124
B.1 s/S Ratios	124
B.2 Emissivity Calculations	124
Appendix C. Ray Tracing	128
C.1 Wireframe Model Primitives	128
C.2 Ray Tracing Algorithm	128
Bibliography	130
Index	132

List of Figures

Figure	Page
1.1. Electromagnetic Spectrum	1
1.2. DHL A330 Baghdad Accident Photos	2
2.1. Blackbody Radiance Curves	7
2.2. BRDF Hemispherical Geometry	9
2.3. Specular and Semi-Specular Reflectance Distributions	12
2.4. Diffuse Reflectance Distribution	13
2.5. Fractional Specularity Reflectance Model	14
2.6. Glint Vector and Alpha Angle	18
2.7. Bare Aluminum DHR	20
2.8. Bare Aluminum Reflectance Curves	21
2.9. Bare Aluminum BRDF (In-plane Reflectance)	22
2.10. Gloss Black Paint DHR	23
2.11. Gloss Black Paint Reflectance Curves	24
2.12. Gloss Black Paint BRDF (In-plane Reflectance)	25
2.13. Infrared Spectral Transmission	26
2.14. MODTRAN Simulated Spectral Transmission - MWIR & LWIR	27
2.15. Deterministic Numerical Quadrature Illustration	28
2.16. Monte Carlo Integration Convergence Example	31
3.1. Azimuth Domain Setup	35
3.2. Blender3D Screenshot of Export Settings	37
3.3. Facet Naming Format	37
3.4. Blender3D Screenshot	37
3.5. Cavity Blackbody Model - Matlab [®]	39
3.6. Cylinder Model - 3-View Drawings	40
3.7. Cylinder Model - Bare Aluminum	41

Figure	Page
3.8. Cylinder Model - Gloss Black Painted	41
3.9. Cylinder Model - Blender3D	42
3.10. Airbus A340-300 Model - Matlab [®]	43
3.11. Engine Exhaust Temperature Profiles	44
3.12. Simple Hemispherical View of Plates	46
3.13. Complex Hemispherical View of Cylinder Model	47
3.14. BRDF Hemispherical Representation in 2- & 3D	48
3.15. Quadrature Integration of the Aluminum BRDF	49
3.16. Importance Sampled Integration Example	51
3.17. BRDF Integration with Normally Distributed Samples	54
3.18. BRDF Integration with Stratified Normally Distributed Samples	55
3.19. Variance of the Peak Integral using Stratified Numerical Quadrature . .	56
3.20. Variance of the Outer Integral using Stratified Numerical Quadrature .	56
3.21. Increased Geometry Hemispherical Sampling Rate	57
3.22. ARFL IR Range Background Model simulated in Matlab [®]	58
3.23. World Sphere Background Model simulated in Matlab [®]	59
3.24. Spectral Radiance of Grass Covered Field	60
3.25. Spectral Apparent Temperature of Concrete	61
3.26. Spectral Apparent Temperature of Asphalt	62
3.27. MWIR Background Spectral Path Radiance	64
3.28. LWIR Background Spectral Path Radiance	65
3.29. Band Integrated Background Path Radiance - Sunny Day	67
3.30. Hemispherical Integration Illustration	69
3.31. Radiosity Algorithm Flowchart	72
3.32. POV Stratified Hemispherical Integration Algorithm Flowchart	75
3.33. Analytical Cavity Blackbody Emissivity	78
3.34. Irradiance Signal at Detector's Optic Plane	81

Figure	Page
3.35. A340-300 Simulation Engagement Positions	83
4.1. Simulated Cavity Blackbody Emissivity	85
4.2. MWIR Gloss Black - Single Specular Bounce	87
4.3. 260K and 300K Blackbody Spectral Radiance Curves	88
4.4. LWIR Bare Aluminum - Single Specular Bounce	89
4.5. LWIR Bare Aluminum - Multiple Specular Bounces	91
4.6. MWIR Bare Aluminum - Multiple Specular Bounces	92
4.7. LWIR Bare Aluminum - Single Integrated BRDF Bounce	94
4.8. LWIR Bare Aluminum - Two BRDF Bounces	96
4.9. MWIR Bare Aluminum - Two BRDF Bounces	97
4.10. Multiple Bounce Convergence	98
4.11. A340-300 Target Intensity - Position 1 MWIR	99
4.12. A340-300 Apparent Irradiance - Position 1 MWIR	100
4.13. Total Apparent Irradiance - Position 1 MWIR	101
4.14. Position 1 - Detector View MWIR	103
4.15. A340-300 Target Intensity - Position 1 LWIR	104
4.16. A340-300 Apparent Irradiance - Position 1 LWIR	105
4.17. Total Apparent Irradiance - Position 1 LWIR	106
4.18. Position 1 - Detector View LWIR	107
4.19. Position 2 - Detector View MWIR	109
4.20. Position 2 - Detector View LWIR	110
4.21. Position 3 - Detector View MWIR	112
4.22. Position 3 - Detector View LWIR	113
4.23. Position 3 - LWIR Multiple Bounce Comparison	114
A.1. Two Plates Simulation Geometry	121
A.2. Two Plates Simulation Results	121
A.3. Open Box Simulation Geometry	122

Figure	Page
A.4. Open Box Simulation Results	123
B.1. Cavity Blackbodies	125
C.1. Ray Tracing Geometry Example	129

List of Tables

Table	Page
2.1. Integral Forms of Radiance	8
2.2. Bare Aluminum Sandford-Robertson BRDF Parameters	19
2.3. Gloss Black Paint Sandford-Robertson BRDF Parameters	20
3.1. Facet Attributes Label Format	38
3.2. Cylinder Model Surface Temperatures	40
3.3. Method of Gouffé Variables	77
4.1. A340-300 Simulation Results - Position 1	102
4.2. A340-300 Simulation Results - Position 2	108
4.3. A340-300 Simulation Results - Position 3	111
B.1. Blackbody Cavity Simulation - s and S Parameters	126

List of Symbols

Symbol		Page
$\varepsilon(\theta)$	Emissivity	7
$\rho(\theta)$	Reflectance	7
A_s	Area of Source	8
Ω_d	Detector Solid Angle	8
I_e	Intensity	8
M_e	Exitance	8
Φ_e	Flux	8
E_e	Irradiance	8
L_r	Reflected Radiance	8
E_i	Incident Irradiance	8
θ_i	Elevation Angle of Incidence	12
θ_r	Elevation Angle of Reflection	12
$\rho_D(\lambda)$	Diffuse Spectral Reflectance	15
$\epsilon(\lambda)$	Spectral Emissivity	16
b	Grazing Angle Reflectivity	16
e	Width of Specular Lobe	16
f_r	BRDF	16
f_d	BRDF Diffuse Component	16
f_s	BRDF Specular Component	16
$\hat{\mathbf{g}}$	Glint Vector	17
α	Glint Angle	17
I	Analytic Integral Result	27
w_i	Numerical Integration Weighting Factor	28
\hat{I}	Analytic Integral Approximation	28
Ω	Solid Angle	31

Symbol		Page
H_2O	Water Vapor	63
CO_2	Carbon Dioxide	63
$Le_{(Observed)}$	Observed Radiance	66
ε_0	Cavity Blackbody Total Observed Emissivity	77
ε	Cavity Blackbody Intrinsic Emissivity	77
l	Cavity Blackbody Cavity Depth	77
r	Cavity Blackbody Aperture Radius	77
s	Cavity Blackbody Aperture Area	77
S	Cavity Blackbody Internal Surface Area	77
S_0	Surface Area of a Sphere with Same Diameter as the Cavity	77
$E_{e \text{ NoTarget}}$	Observed Irradiance - No Target	80

List of Abbreviations

Abbreviation	Page
IR	Infrared 1
MANPADS	Man Portable Air Defence Systems 2
IMG	Issue Motivated Groups 2
LCAIR	Large Commercial Aircraft Infrared Trend Analysis Tool 3
BRDF	Bi-Directional Reflectance Distribution Function 4
BB	Blackbody 6
DHR	Directional Hemispherical Reflectance 11
HDR	Hemispherical Directional Reflectance 11
2D	Two Dimensions 12
3D	Three Dimensions 12
AFRL	Air Force Research Laboratory 15
MWIR	Mid Wave Infrared 18
LWIR	Long Wave Infrared 18
SWIR	Short Wave Infrared 26
PDF	Probability Density Function 29
FOV	Field of View 33
SNR	Signal to Noise Ratio 33
CDF	Cumulative Distribution Function 52
POV	Point of View 66
NEI	Noise Equivalent Irradiance 79
ILS	Instrument Landing System 82
RF	Radio Frequency 82
SPIRITS	Spectral and Inband Radiometric Imaging of Targets and Scenes . 118

A STUDY OF
 BI-DIRECTIONAL REFLECTANCE DISTRIBUTION FUNCTIONS
 AND THEIR EFFECT ON
 INFRARED SIGNATURE MODELS

I. Introduction

1.1 Infrared Spectrum

The infrared (IR) spectrum is a subset of the electromagnetic spectrum between visible radiation (light) and radio waves (millimeter and longer wavelengths) (Figure 1.1). It has been used extensively in the scientific community, with examples of communications, spectroscopy, and the humble remote control.

The most common and widespread application is thermal emission and imaging. Industries including home security, meteorology, night vision and thermal heating rely on the infrared spectrum’s physical properties for their operation. Another application of infrared energy is infrared guided (heat seeking) missiles. These missiles exploit the property that all matter above 0 Kelvin emits radiation. This energy is known as Planckian radiation, and for most objects at realizable temperatures, the emission is in the IR spectrum.



Figure 1.1: The infrared spectrum is a subset of the electromagnetic spectrum. Wavelength is in units of microns (μm). Adapted from [4, Figure 1.1].



Figure 1.2: The DHL A330 aircraft was hit by an SA-14 MANPADS in the left wing and lost all hydraulics. Reproduced from airdisaster.com.

1.2 *The MANPADS Threat*

Since the proliferation of thousands of man portable air defence systems (MANPADS) after the fall of the Soviet Union, there has been a credible threat to commercial and military aviation from terrorist and issue motivated groups (IMGs). Several aircraft have been shot down in past years, and whilst these events have occurred mainly in European and African countries, the current terrorist threat level to the United States and other allied countries is high. A recent incident occurred when a DHL Airbus A330 cargo aircraft was hit by an SA-14 MANPADS after takeoff from Baghdad International Airport on 22 November 2003. The damage was so severe that the aircraft lost all three hydraulic systems, and the aircrew were forced to control the aircraft with only differential thrust. This was the only time an aircraft has safely landed with all hydraulic systems inoperable. In all previous attempts, the aircraft crashed catastrophically with major loss of life. Figure 1.2 shows the damage that the DHL aircraft sustained from the missile hit.

The issue is recognized by governments around the world and the US Department of Homeland Security has expressed a desire to mandate IR countermeasures

be installed on large commercial aircraft in the US. Legislation has been introduced into the US Congress for consideration, (HR. 580, S.311).

1.3 Problem Description

This research topic began in 2004 with Capt Ruben Martinez who created a trend analysis tool, named LCAIR (Large Commercial Aircraft Infrared Trend Analysis Tool) [17]. The tool was developed with the intent to quickly calculate IR signature trends. The trends were hoped to enable low observability properties to be better designed into an aircraft during the design stage, rather than as an afterthought.

Capt Jonathan Bortle, in 2006, validated the LCAIR code using a physical model, where calibrated measurements were made for comparison with the LCAIR prediction for the same parameters. The code performed well and was over 90% accurate, however, it failed in certain situations when a highly reflective surface was used. Additionally, LCAIR only uses a single bounce specular reflectance algorithm, which provides some other limitations that will be discussed in Chapter III.

1.3.1 Purpose. This thesis investigates the effect of Bi-Directional Reflectance Distribution Functions (BRDFs) when incorporated into IR signature simulations, with the intent to analyze and improve on the limitations of LCAIR that Bortle described in [3]. Additionally, several algorithms will be investigated to determine the optimum balance between simulation accuracy and calculation time.

1.4 Thesis Overview

The thesis is divided into five chapters. Chapter I introduced the research topic, the reasons for it, previous research and goals for this thesis. Chapter II will introduce or refresh the reader with concepts and background theory of physical phenomena, mathematical methods and models that are applied in the thesis.

Chapter III develops the method and algorithms that will be used to evaluate the different techniques utilized to calculate the IR signature. A detailed discussion and development of the simulation parameters and assumptions is also included.

Chapter IV provides the detailed results of each of the simulations. Three different simulations are performed;

- Initially, analytical simulations are performed to quantitatively validate the accuracy of the algorithms. These are followed by a simulation which reproduces the properties of an artificial cavity blackbody source,
- The second simulation investigates the limitations of the LCAIR algorithm, by including (BRDF) reflections and multiple bounces into the calculations. The effect of different combinations of these is also shown.
- The simulations conclude with a scenario of a MANPADS engaging an Airbus A340-300 aircraft whilst landing at a generic airport. Three positions are chosen and the IR signature at the three observation angles is calculated to determine the required parameters of the MANPADS to detect and lock-on to the aircraft.

Chapter V provides a summary of the results, recommendations for further work and lessons learned over the course of this thesis.

Several appendices are also included which provide information that helps the reader with mathematical methods and other techniques that are used in the simulations.

1.5 Literature Review

A comprehensive literature review was performed whilst searching for IR simulation techniques and propagation algorithms. Whilst many papers are available in the open literature, their content is concerned with either system level design [7, 8], or focusses on specific properties of BRDFs [2, 24].

Specific code and algorithms of these IR simulation tools were not found, as they are either classified or commercial-in-confidence. For this reason, the computer graphics algorithms found in [5] and [10] were used to improve the LCAIR propagation algorithm of [3] and [17].

Several papers were found late in the thesis effort, [14, 16, 21, 22]. These papers provide a good introduction into IR signature modelling and analyze important aspects of simulation modelling, trend analysis and system parameters. Another paper, [13], discusses signature analysis in the context of aircraft conceptual design. The content of these papers was not included in this thesis due to limited time, however, they would provide a good starting point for the next IR signature student.

II. Background

This chapter provides applicable background theory and information for the reader that is useful in understanding the concepts and methods described in Chapter III.

2.1 Blackbody Radiation

It is assumed that the reader is comfortable with the concepts of blackbody radiation, emissivity and reflectance. The relevant equations will be included in this chapter for reference in subsequent chapters. However, if the reader requires extra information relating to the derivation of the equations, and concepts, they are directed to [3, 4, 17].

A blackbody is a perfect emitter of Planckian radiation. Kirchoff's law states that for a body to be in thermal equilibrium the absorbed equals the emitted energy. Thus the incident flux, $\Phi_{incident}$, equals the sum of the absorbed, reflected, and transmitted flux. If the body is opaque, the transmitted flux equals zero, and then the re-emitted and reflected flux equals the incident flux:

$$\Phi_{incident} = \Phi_{reflected} + \Phi_{absorbed}. \quad (2.1)$$

A perfect blackbody is one that absorbs all incident radiation. To remain in thermal equilibrium, the body must re-emit that radiation. The spectrum of the emitted radiation is dependent upon the temperature of the material. Equation (2.2) shows the expression for spectral radiance, $L_e(\lambda)$, of a perfect blackbody of temperature, T , in Kelvin, where h is Planck's constant, c is the speed of light, k is Boltzmann's constant, and λ is the wavelength of interest. Figure 2.1 shows the emitted spectral radiance of a blackbody (BB) plotted at several temperatures.

$$L_{e \text{ BB Self-Emitted}} = \frac{2hc^2}{\lambda^5 (e^{hc/\lambda kT} - 1)} \left[\frac{W}{cm^2 - sr - \mu m} \right] \quad (2.2)$$

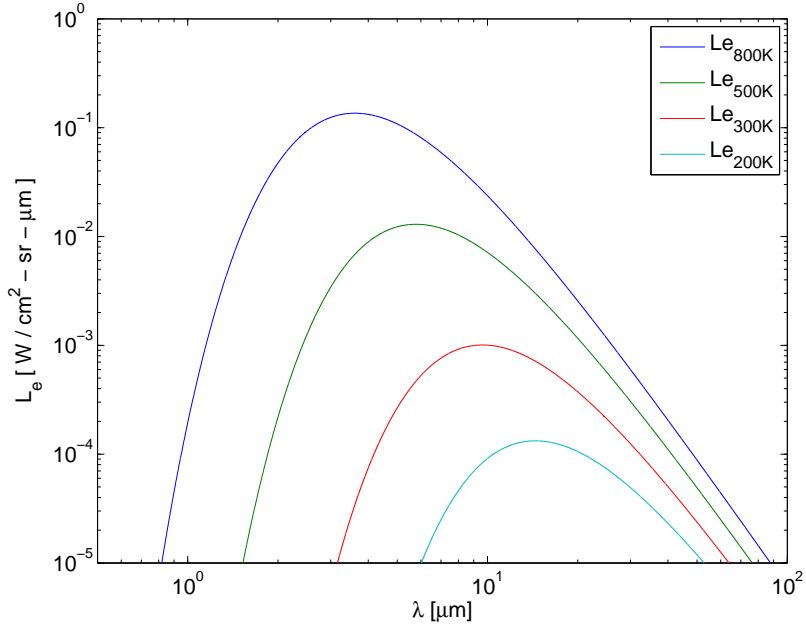


Figure 2.1: Blackbody radiance is a function of both temperature and wavelength. These theoretical curves will be scaled by emissivity, $\varepsilon(\theta)$, to produce greybody emission.

2.1.1 Reflectance. Reflectance, $\rho(\theta)$, is defined as the ratio between incident flux and reflected flux at a given incident elevation angle, θ , from the surface normal. The remaining flux is absorbed.

$$\rho(\theta) = \frac{\Phi_{\text{Reflected}}}{\Phi_{\text{Incident}}} \quad (2.3)$$

2.1.2 Emissivity. Recall from Equation (2.1) that what is not reflected is absorbed. The absorptance factor is the percentage of flux that is absorbed and re-emitted, and for an opaque surface in thermal equilibrium, is defined as the emissivity,

$$\varepsilon(\theta) = 1 - \rho(\theta). \quad (2.4)$$

2.2 Radiometry

Radiometry is the mathematics of calculating energy (electromagnetic flux) transfer from a source to a detector. Exitant flux from a source, incident flux onto

Table 2.1: Integral Forms of Radiance. The e subscript implies power units of Watts, not photon units. A_s is the area of the source and Ω_d is the solid angle subtended by the detector.

Quantity	Variable	Expression	Units
Intensity	I_e	$\int_{A_s} L_e \cos(\theta_s) dA_s$	$[\frac{W}{sr}]$
Exitance	M_e	$\int_{\Omega_d} L_e \cos(\theta_s) d\Omega_d$	$[\frac{W}{m^2}]$
Flux	Φ_e	$\int_{\Omega_d} \int_{A_s} L_e \cos(\theta_s) dA_s d\Omega_d$	$[W]$
Irradiance	E_e	$\frac{\partial \Phi_e}{\partial A_d}$	$[\frac{W}{m^2}]$

a surface and collected flux by a detector can easily be calculated and converted using radiometric quantities. The most basic quantity is radiance, and carries units of *Watts per steradian per unit area*. Other quantities can be gained from radiance and are expressed in Table 2.1; where θ_s is the angle from the observation angle to the surface normal, dA_s is the differential area of the source, $d\Omega_d$ is the differential solid angle of the detector, and Φ_e is the integrated flux through the detector.

2.3 Bi-Directional Reflectance Distribution Function

The reflectance property, $\rho(\theta)$, represents the proportion of energy that is reflected off the surface for a given incident angle, θ , however, there is no other information available with respect to the reflection angle. The specular or diffuse nature of the surface is unknown. In practice, energy is not perfectly specularly reflected nor scattered equally in all directions. The BRDF provides a method of describing reflectance as a function of incident (source) and reflected (observed) angles and wavelength. The BRDF is defined as the differential ratio of the reflected radiance, L_r , to the incident irradiance, E_i . Nicodemus *et al.* introduced the concept of the BRDF in [20] which contains a more rigorous treatment of the definition, assumptions and applications. Although differential quantities cannot be directly measured, as a finite

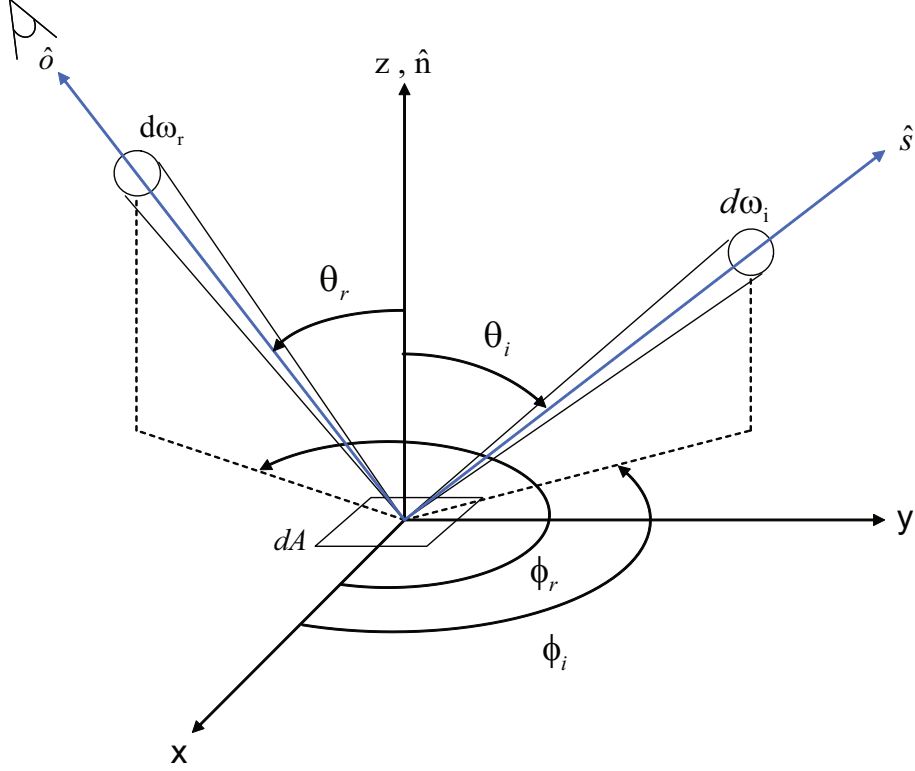


Figure 2.2: Hemispherical geometry of the BRDF, defining the elevation and azimuth angles for both the source and observation vectors.

solid angle of energy must be collected, they can be calculated from the empirical data of each surface. As defined above, the BRDF, with units of inverse steradians, is shown in Equation (2.5) with angles as defined in Figure 2.2;

$$\begin{aligned}
 f_r(\theta_i, \phi_i, \theta_r, \phi_r, \lambda) &= \frac{dL_r(\theta_r, \phi_r)}{dE_i(\theta_i, \phi_i)} \\
 &= \left[\frac{W}{sr - m^2} \right] / \left[\frac{W}{m^2} \right] = \left[\frac{1}{sr} \right]
 \end{aligned} \tag{2.5}$$

where θ_i is the incident elevation angle measured from the surface normal, ϕ_i is the incident azimuthal angle measured from the x-axis or some reference, θ_r is the reflected elevation angle again measured from the surface normal, and ϕ_r is the reflected azimuthal angle measured from the same reference as ϕ_i .

2.3.1 Dimensionality Reduction. The full BRDF is a hi-fidelity representation of a surface’s reflectance properties; however, it is very complex and requires a large amount of processing power and memory, which is not needed for some applications. The domain of the BRDF can be significantly reduced using the theory of reciprocity, an assumption of surface isotropy and wavelength simplifications.

2.3.1.1 Reciprocity. The theory of reciprocity states that the path of light is independent of the direction of propagation. Reversing the direction of propagation does not alter the reflectance properties. The BRDF domain is reduced by using the symmetry of the variables,

$$f_r(\theta_i, \phi_i, \theta_r, \phi_r, \lambda) = f_r(\theta_r, \phi_r, \theta_i, \phi_i, \lambda). \quad (2.6)$$

2.3.1.2 Wavelength. If the BRDF can be assumed to not change significantly over a wavelength band, the BRDF can be set constant across the band. This assumption breaks down as the spectral width of the band increases where the majority of materials become more specular as the wavelength increases. This effect will be clearly seen later, in Figure 2.7, where the diffuse component decreases and specular component increases as the wavelength increases.

2.3.1.3 Surface Isotropy. Surfaces can be considered isotropic if their reflective properties are independent of the azimuthal incidence angle, ϕ_i ; most common surface types fit this definition. Two exceptions to this assumption are polarized materials and materials with surface striae (e.g., gratings). These materials will naturally exhibit different reflectance characteristics as a function of ϕ_i . Under the isotropic assumption, the strict dependence upon ϕ_i and ϕ_r with reference to the x-axis, as shown in Figure 2.2, is removed and only the delta ($\Delta\phi = \phi_i - \phi_r$) is required. Applying these assumptions to Equation (2.5) gives the simplified BRDF

with three dimensions (θ_i , θ_r and $\Delta\phi$),

$$f_r(\theta_i, \theta_r, \Delta\phi) = f_r(\theta_i, \phi_i, \theta_r, \phi_r, \lambda). \quad (2.7)$$

2.3.2 Integral Forms of the BRDF. Equation (2.5) can be converted to many quantities by integrating across one or more domains of the BRDF. The integral forms provide information about the material that may not be intuitive by piecewise evaluation of the BRDF. A few common quantities that will be used later are defined below and a full list of possible integrated quantities can be found in [20, Tables 2 & 3].

2.3.2.1 Directional Hemispherical Reflectance. The Directional Hemispherical Reflectance (DHR) describes the percentage of the energy reflected *into* the entire hemisphere from a given incident angle [20, Table 3, Equation (3.1)]. This function is derived from the integral of the BRDF over all exitant angles as shown in Equation (2.8), where the ϕ_i dependence is dropped under the previous surface isotropy assumption. However, it is important to keep the ϕ_i reference as a baseline for the propagation algorithms described in section 3.5. The DHR must also equal the reflectance, $\rho(\theta)$, as reflectance is the ratio of reflected flux to incident flux. Integrating the BRDF over all reflected angles accounts for all reflected energy (flux), and is thus a ratio total energy.

$$DHR(\theta_i) = \rho(\theta_i) = \int_0^{2\pi} \int_0^{\pi/2} f_r(\theta_i, \phi_i, \theta_r, \phi_r) \cos(\theta_r) \sin(\theta_r) d\theta_r d\phi_r \quad (2.8)$$

2.3.2.2 Hemispherical Directional Reflectance. Conversely, the Hemispherical Directional Reflectance (HDR) describes the energy that is reflected *from* the whole hemisphere into a specific direction [20, Table 3, Equation 3.6]. The HDR is obtained by integrating the BRDF over the incident angle domains as expressed in Equation (2.9) with the azimuthal dependence removed as developed before.

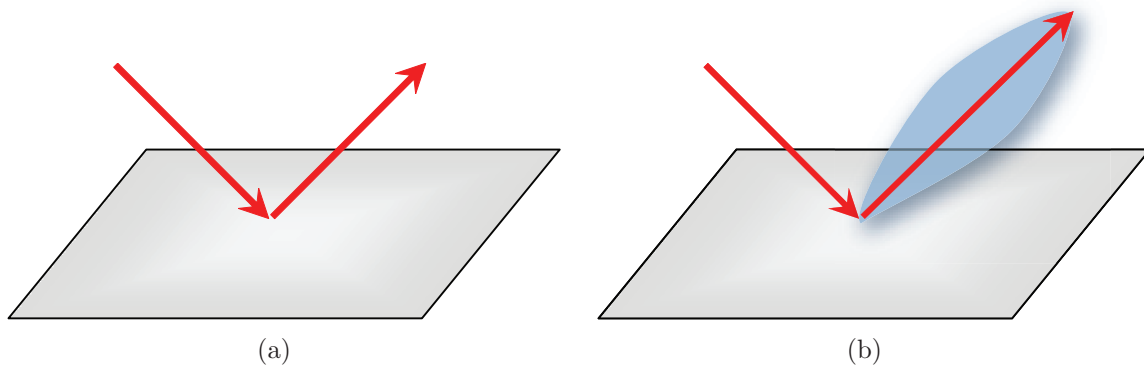


Figure 2.3: (a) A purely specular reflection does change the distribution of energy from incident to reflected directions. (b) Semi-specular reflections are almost specular where the incident distribution spreads slightly and can be described with some lobe width.

$$HDR(\theta_r) = \int_0^{2\pi} \int_0^{\pi/2} f_r(\theta_i, \phi_i, \theta_r, \phi_r) \cos(\theta_i) \sin(\theta_i) d\theta_i d\phi_i \quad (2.9)$$

2.3.3 Surface Reflectance Distributions. Using the BRDF, the reflectance of a surface can now be described in detail as a function of incident and reflected angles to represent the specific reflectance distribution for that material type. Two trivial cases are diffuse and specular surfaces. Other cases are represented by the distribution of the reflectance properties which are discussed below.

2.3.3.1 Specular Reflectance. Specular reflection is perhaps the most common reflectance type. It is the major assumption in ray optics and is the basis of the well known Law of Reflection, $\theta_i = \theta_r$. Surfaces which are optically smooth (a material with surface roughness appreciably smaller than the wavelength of interest) can be considered specular. The Law of Reflection requires that the angle of incidence equals the angle of reflection; this is the two dimensional (2D) definition. In three dimensions (3D), the elevation angles for the incident and reflected rays must equal

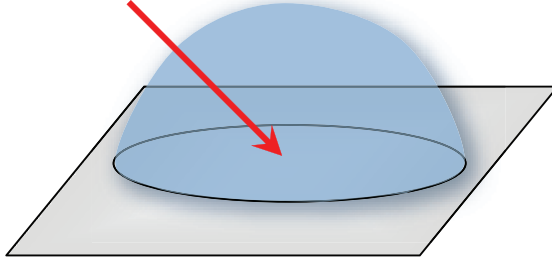


Figure 2.4: The reflected radiance distribution is constant, $f_r = 1/\pi$ steradians, in all directions for the perfectly diffuse reflectance distribution.

and the azimuthal angles must differ by π radians. Applying these conditions to the BRDF, yields Equation (2.10), and is depicted in Figure 2.3 (a). The specular case is special and usually requires a separate algorithm to evaluate the equality.

$$f_r(\theta_i, \theta_r, \Delta\phi) = \begin{cases} \rho(\theta), & (\theta_i = \theta_r, \Delta\phi = \pi) \\ 0, & \textit{else} \end{cases} \quad (2.10)$$

A relaxation to strict equality conditions of the specular case is known as the semi-specular case. Semi-specular is when the surface is almost specular, however, there is some width to the reflected solid angle, producing a specular lobe instead of a perfectly reflected, collimated beam. This effect is chiefly caused by the surface not being completely optically smooth and is depicted in Figure 2.3 (b).

2.3.3.2 Diffuse Reflectance. The opposite of the specular case is where the energy is scattered equally in every direction in the hemisphere, as depicted in Figure 2.4, and is defined as diffuse reflectance. Some common diffuse materials are matte paints, carpet and video projection screens. As the exitant radiance from the surface is constant in every direction, so too is the BRDF. Recall that the DHR is the integral of the BRDF over all exitant angles and is equal to the reflectance at that incident elevation angle. Therefore, the diffuse BRDF, when integrated over the exitant hemisphere, must equal $\rho(\theta_i)$. This leads to the value of $1/\pi$ for the diffuse BRDF and is scaled by $\rho(\theta_i)$,

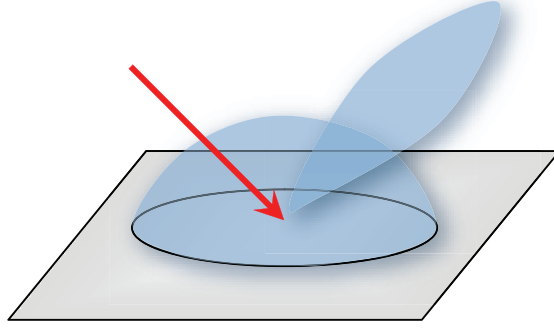


Figure 2.5: The fractional specularity reflectance model is a combination of a diffuse and semi-specular surface.

$$f_r(\theta_i, \theta_r, \Delta\phi) = \frac{\rho(\theta_i)}{\pi} \quad (2.11)$$

$$DHR(\theta_i, \phi_i) = \int_0^{2\pi} \int_0^{\pi/2} f_r(\theta_i, \phi_i, \theta_r, \phi_r) \cos(\theta_r) \sin(\theta_r) d\theta_r d\phi_r \quad (2.12)$$

$$= \int_0^{2\pi} \int_0^{\pi/2} \frac{\rho(\theta_i)}{\pi} \cos(\theta_r) \sin(\theta_r) d\theta_r d\phi_r = \rho(\theta_i). \quad (2.13)$$

2.3.3.3 Fractional Specularity Reflectance Model . In reality, few surfaces fit the definitions of perfectly diffuse or specular, thus, simple analytical descriptions of the BRDF are not sufficient to represent the reflectance distribution throughout the hemisphere. For surfaces that are nearly specular, but exhibit some diffuse reflectance (or vice-versa), a fractional specularity model can be defined. The model can be defined in two ways; either the hemisphere is separated into diffuse and specular regions in a piecewise approach, or a complete hemispherical diffuse component is summed with the specular component to represent the distribution; an example of the second method is shown in Figure 2.5.

2.3.3.4 Parameterized BRDF Models. Sections 2.3.3.1 through 2.3.3.3 discussed theoretical models to represent reflectance distributions of surfaces. However, real surfaces do not exhibit uniform distributions like the diffuse case or the delta function of the specular case; thus, their empirical reflected radiance measurements

will vary with elevation and azimuth angles. Materials (especially specular ones) can exhibit large gradients in the BRDF function, which requires a high sampling rate in the empirical measurements. This ensures the reflectance distribution is recorded properly, however, this process produces large amounts of data.

For practical uses, it may not be feasible to store the entire array of measured data for recall. Additionally, a BRDF value for a point which lies between sample measurements may be required. In these two cases, it is much simpler to develop a model which parameterizes the BRDF surface allowing for fast evaluation of the required value, independent of initial measurement locations. The functions to be fit to the empirical data depend very much upon the empirical BRDF shape; a single model will not give good results for all surface reflectance types. Obviously, the more empirical measurements and the more degrees of freedom in the functions, the more accurate the parametrization will become.

There are many BRDF models available to parameterize empirical BRDF measurements that can be found in literature. Sandford-Robertson [23], Maxwell-Beard [18], and He-Torrance-Sillion [12], are just three. This thesis will concentrate on the Sandford-Robertson model, as it is predominantly used for IR BRDF's on common aircraft surfaces. The Air Force Research Laboratory (AFRL) sponsored the development of the Sandford-Robertson model.

2.3.4 Sandford-Robertson Reflectance Model. One of the common reflectance models used in aircraft IR signature simulations is the Sandford-Robertson Model. Brian Sandford and David Robertson published the model in 1985 [23]. The model is a fractional specular model and is divided into two components, specular and diffuse.

The model is described by four parameters, which represent the physical properties of the material;

- Diffuse spectral reflectance, $\rho_D(\lambda)$,

- Spectral emissivity, $\epsilon(\lambda)$,
- Grazing angle reflectivity, b ; and
- Width of specular lobe, e .

The functions to parameterize the empirical data are separated into diffuse and specular components, where the above parameters are chosen to fit both a diffuse floor and a specular lobe to the measured data. The total BRDF, f_r , is the sum of the diffuse, f_d , and specular, f_s , components,

$$f_r = f_d + f_s. \quad (2.14)$$

2.3.4.1 Diffuse Floor. The diffuse floor is assumed to be symmetric in azimuth as a result from subsurface scattering and surface roughness. It is calculated by;

$$f_d = \frac{1}{\pi} \frac{g(\theta_r) \rho_D(\lambda) g(\theta_i)}{[G(b)]^2} \quad (2.15)$$

where the $g(\theta_r)$, $g(\theta_i)$ and $G(b)$ are defined by,

$$g(\theta_r) = \frac{1}{1 + b^2 \tan^2(\theta_r)} \quad (2.16)$$

$$g(\theta_i) = \frac{1}{1 + b^2 \tan^2(\theta_i)} \quad (2.17)$$

$$G(b) = \frac{1}{1 - b^2} \left[1 - \frac{b^2}{1 - b^2} \log\left(\frac{1}{b^2}\right) \right] \quad (2.18)$$

For a more detailed explanation of the components, see [23].

2.3.4.2 Specular Lobe. The specular reflectance in the Sandford-Robertson model is a modified version of the Trowbridge and Reitz model [25]. The lobe is calculated by Equation (2.19) and is normalized so the hemispherical integral of the BRDF is equal to the DHR measurements. Equations (2.20) through (2.24) define the components that calculate f_s . Again, the reader is referred to [23] for a

detailed derivation and further information relating to the Sandford Robertson BRDF Model.

$$f_s = \frac{1}{4\pi} \rho_s(\lambda, \theta_i) \frac{h(\alpha)}{H(\theta_i)} \frac{1}{\cos(\theta_r)} d(\theta_r) \quad (2.19)$$

$$\rho_s(\lambda, \theta_i) = 1 - \rho_d(\lambda, \theta_i) - \varepsilon(\lambda, \theta_i) \quad (2.20)$$

$$\varepsilon(\lambda, \theta_i) = \varepsilon(\lambda) \frac{g(\theta_i)}{G(b)} \quad (2.21)$$

$$h(\alpha) = \frac{1}{[e^2 \cos^2(\alpha) + \sin^2(\alpha)]^2} \quad (2.22)$$

$$H(\theta_i) = \frac{1}{2e^2} \left[(1 - e^2) \cos(\theta_i) + \frac{[2e^2 + (1 - e^2)^2 \cos^2(\theta_i)]}{\sqrt{(1 - e^2)^2 \cos^2(\theta_i) + 4e^2}} \right] \quad (2.23)$$

$$d(\theta_r) = \frac{1}{1 + b^2 \tan^2(\theta_r)} \quad (2.24)$$

2.3.4.3 Glint Vector. The majority of figures illustrating the model's goodness of fit to empirical data only show the in-plane reflectance ($\phi_r = \phi_i \pm \pi$). Figure 2.9 is an example of the representation style. However, values are required for the out-of-plane angles during the simulation. The glint vector, $\hat{\mathbf{g}}$, represents the distance from the specular reflection vector and is specifically defined as the bisector of the incident vector and the reflected vector. It is shown in Figure 2.6 and is calculated by Equation (2.25). The glint angle, α , is then calculated by Equation (2.26) for use in Equation (2.22).

$$\hat{\mathbf{g}} = \frac{(\hat{\mathbf{o}} + \hat{\mathbf{s}})}{\sqrt{2(1 + \hat{\mathbf{o}} \cdot \hat{\mathbf{s}})}} \quad (2.25)$$

$$\alpha = \cos^{-1}(\hat{\mathbf{g}} \cdot \hat{\mathbf{n}}) \quad (2.26)$$

The Sandford-Robertson model parameterizes with the assumption that the surface is predominantly specular with a diffuse floor; this is why the glint vector and α angle are used to provide a larger attenuation in BRDF value the further away the observation vector is from the specular condition, in both ϕ_r and θ_r .

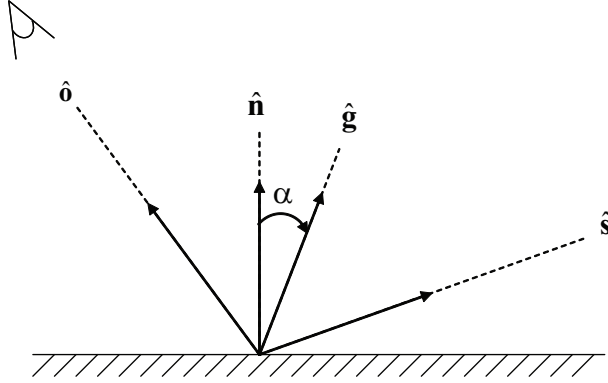


Figure 2.6: Sketch of the glint vector, $\hat{\mathbf{g}}$, and α angle, referenced to the source, observation and normal vectors. The magnitude of the α angle is a measure of the angular separation between the observation and specular reflection vectors. Reproduced from [23].

2.3.5 Bare Aluminum Material. The first surface treatment of interest is bare aluminum. Bortle measured the reflectance data using DHR measurements of bare aluminum. The results are included in Figure 2.7, reproduced from [3] for completeness. These spectral curves were then averaged over two bands. The mid wave infrared (MWIR) band spans $3 - 5\mu m$, and the long wave (LWIR) band covers $8 - 12\mu m$. Figure 2.8 provides average reflectance data as a function of incident elevation. The data points were then parameterized with polynomial functions to provide the $\rho(\theta_i)$ functions in the calculation of emissivity and self emitted radiance of bare aluminum surfaces.

BRDF data was taken with AFRL's scatterometer to provide an empirical BRDF. These empirical results were then parameterized by the Sandford-Robertson model; both sets of data are shown in Figure 2.9 with parameters as listed in Table 2.2. An attribute to note of the aluminum surface is the diffuse component, which is considerable at $3\mu m$, but decreases to almost zero at $12\mu m$. Additionally, as the diffuse component is reducing, the specular component increases to keep the total reflectance relatively constant across the two wave bands.

Table 2.2: Sandford-Robertson BRDF model parameters for the bare aluminum surface, reproduced from [3]. A detailed approach to the selection and parameterizations process can also be found in [3].

Spectral Region	$\epsilon(\lambda)$	$\rho_D(\lambda)$	b	e
MWIR ($3 - 5\mu m$)	0.110	0.020	0.050	0.0042
LWIR ($8 - 12\mu m$)	0.080	0.020	0.050	0.0042

The term *diffuse component* is misleading. The previous definition of diffuse indicated that it was distributed across the whole hemisphere; however, the DHR diffuse measurement strictly means non-specular. When the DHR measurements are made, a small baffle is inserted into the reflectometer to block the specular component to measure the *diffuse* component. This baffle only blocks a very small solid angle, thus, energy that is still in the specular lobe is recorded in the diffuse section of the DHR measurements. Figure 2.9 shows the specularity of the aluminum material, it just happens that the specular lobe is wide enough to extend into the *diffuse* measurement solid angle.

2.3.6 Gloss Black Painted Aluminum Material. Similarly to the bare aluminum case, DHR (Figure 2.10), $\rho(\theta)$ (Figure 2.11) and BRDF (Figure 2.12) measurements were taken with the gloss black painted aluminum surface and the BRDF was parameterized using the Sandford-Robertson model (Table 2.3).

An attribute of the gloss black paint to note is the magnitude of the specular peak of the BRDF; it is approximately two orders of magnitude lower than that of the bare aluminum surface. This can be seen in the DHR data also, where the specular reflectance of the gloss paint is ~ 0.3 compared with the bare aluminum surface's reflectance of ~ 0.8 . The effect of this will be shown later in Chapter IV.

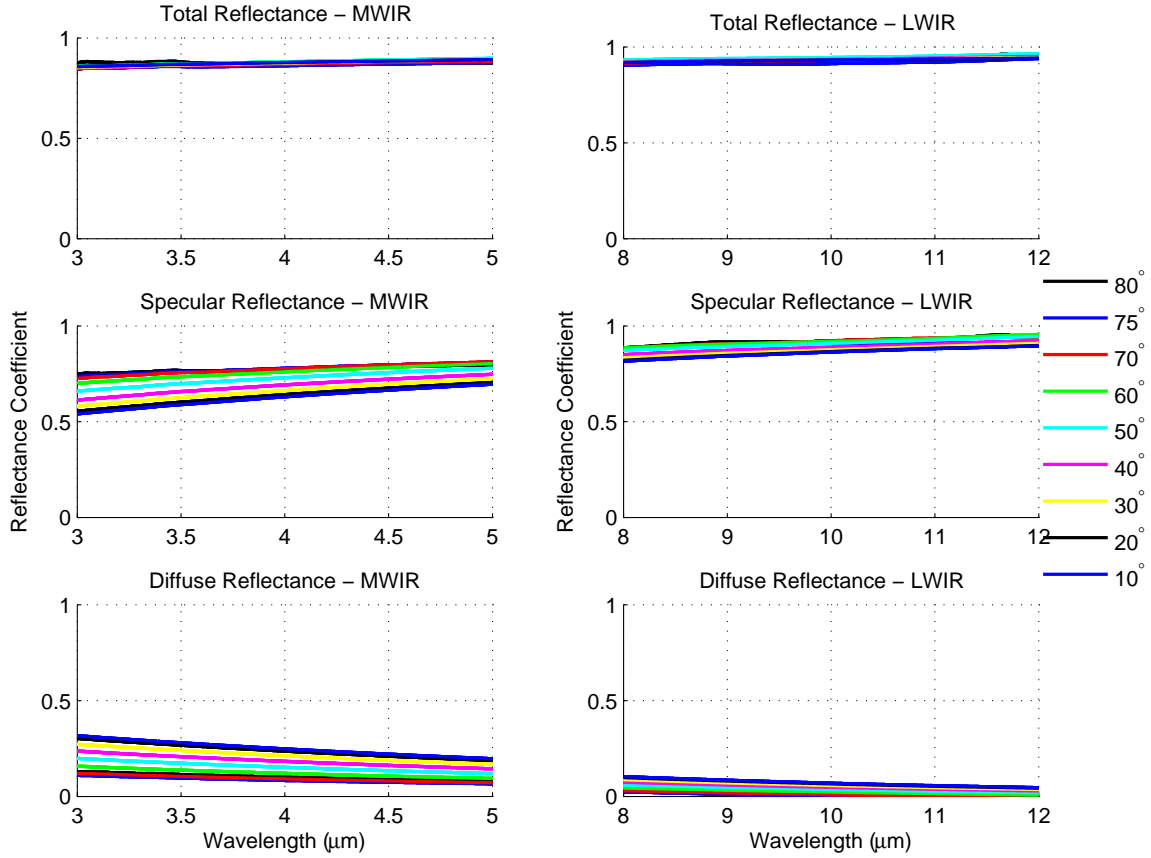


Figure 2.7: Directional Hemispherical Reflectance measurements for the bare aluminum surface, reproduced from [3, Figure 3.8].

Table 2.3: Sandford-Robertson BRDF model parameters for the gloss black paint surface, reproduced from [3]. A detailed approach to the selection and parameterizations process can also be found in [3].

Spectral Region	$\epsilon(\lambda)$	$\rho_D(\lambda)$	b	e
MWIR (3 – 5 μm)	0.890	0.001	0.160	0.005
LWIR (8 – 12 μm)	0.880	0.00075	0.160	0.005

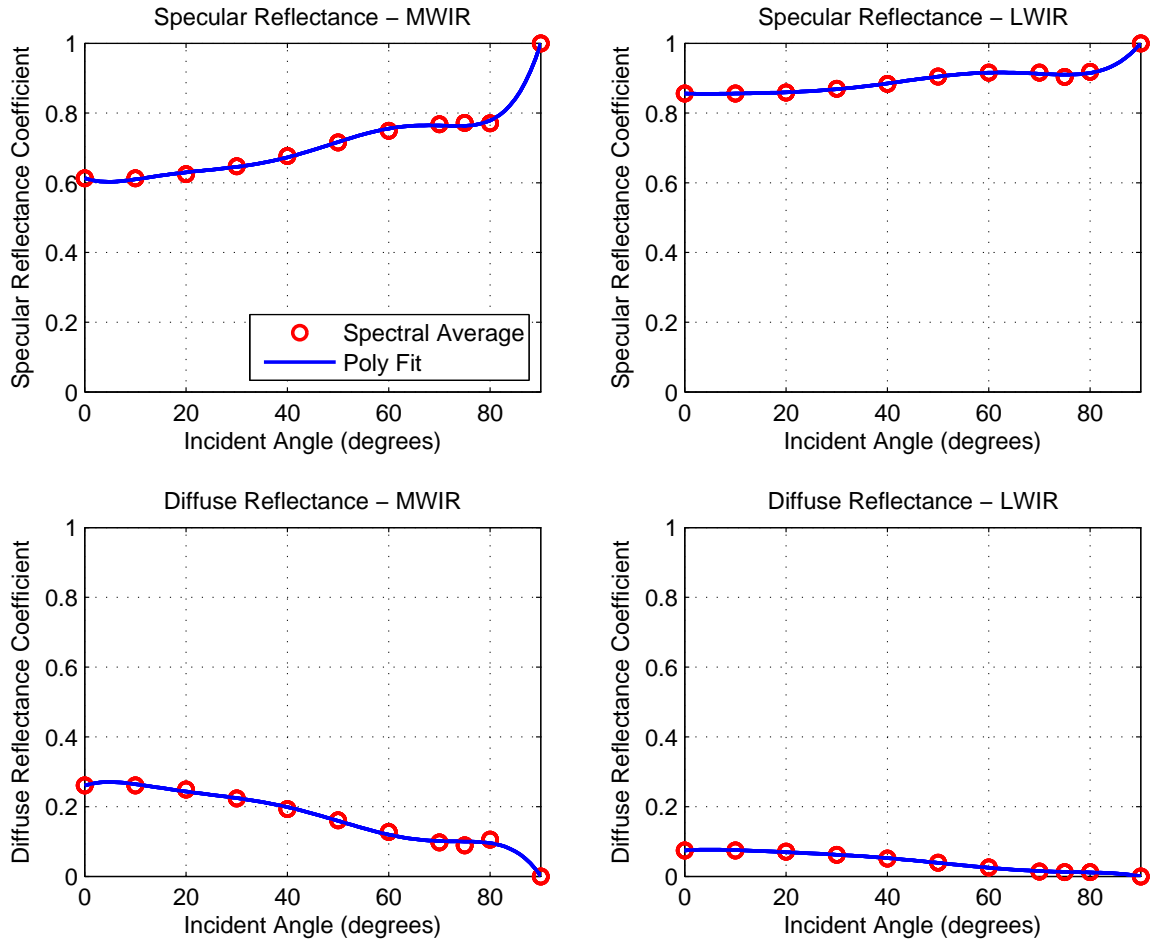


Figure 2.8: $\rho(\theta)$ curves for bare aluminum in both MWIR and LWIR bands. The y-axis limits are set to $[0 \ 1]$ as a reference to show the difference between wave bands and material types. For images showing goodness of fit for the reflectance parametrization, see [3, Figure 3.9 (b)].

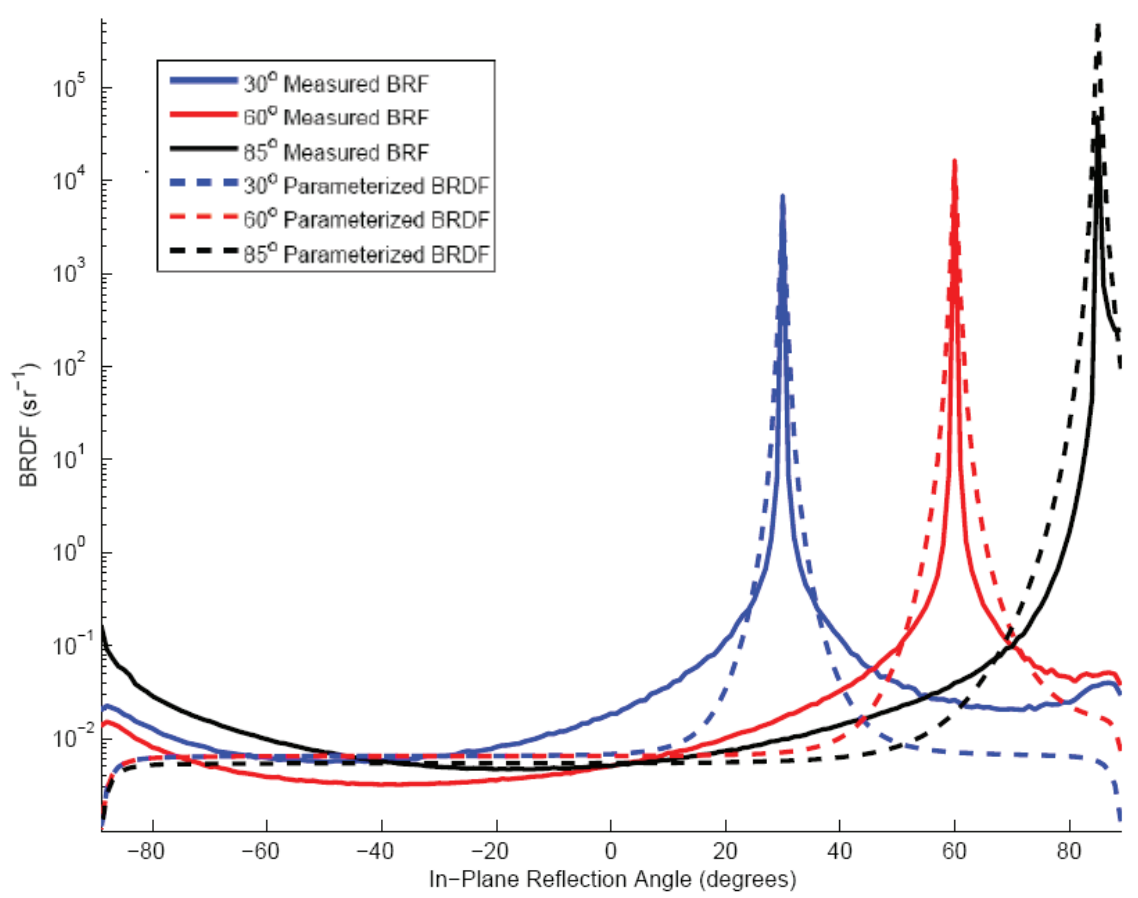


Figure 2.9: Empirical and parameterized BRDF for the bare aluminum surface, reproduced from [3, Figure 3.22 (b)].

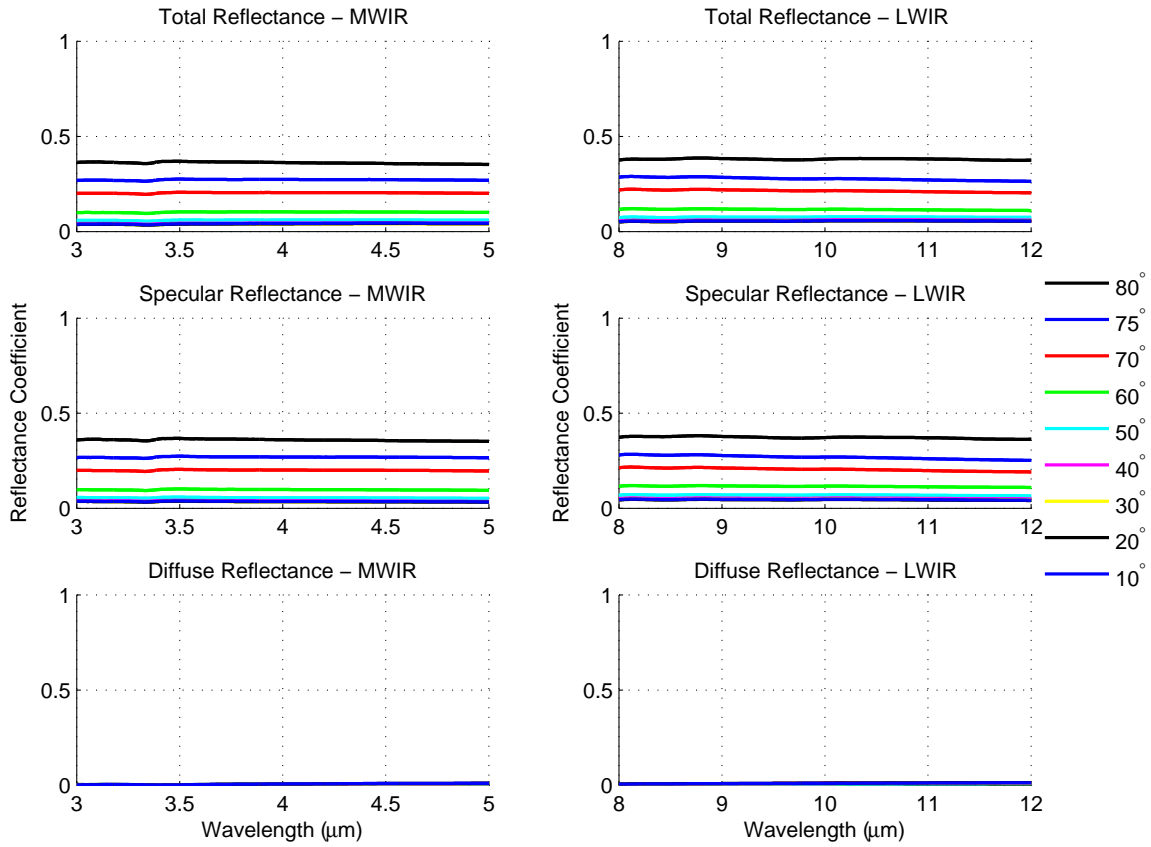


Figure 2.10: Directional Hemispherical Reflectance measurements for the gloss black surface, reproduced from [3, Figure 3.7].

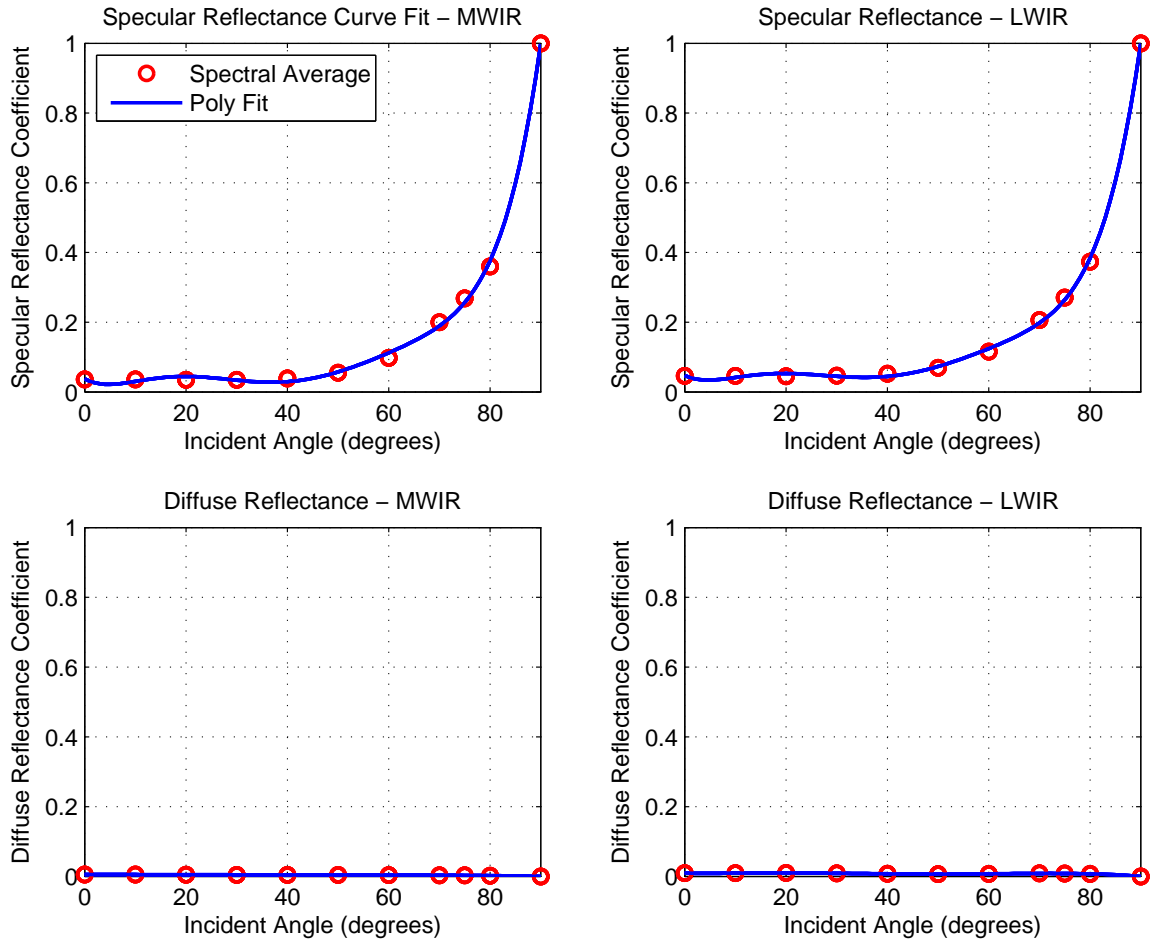


Figure 2.11: $\rho(\theta)$ curves for gloss black paint in both MWIR and LWIR bands. The y-axis limits are set to $[0\ 1]$ as a reference to show the difference between wave bands and material types. For images showing goodness of fit for the reflectance parameterizations, see [3, Figure 3.9 (a)].

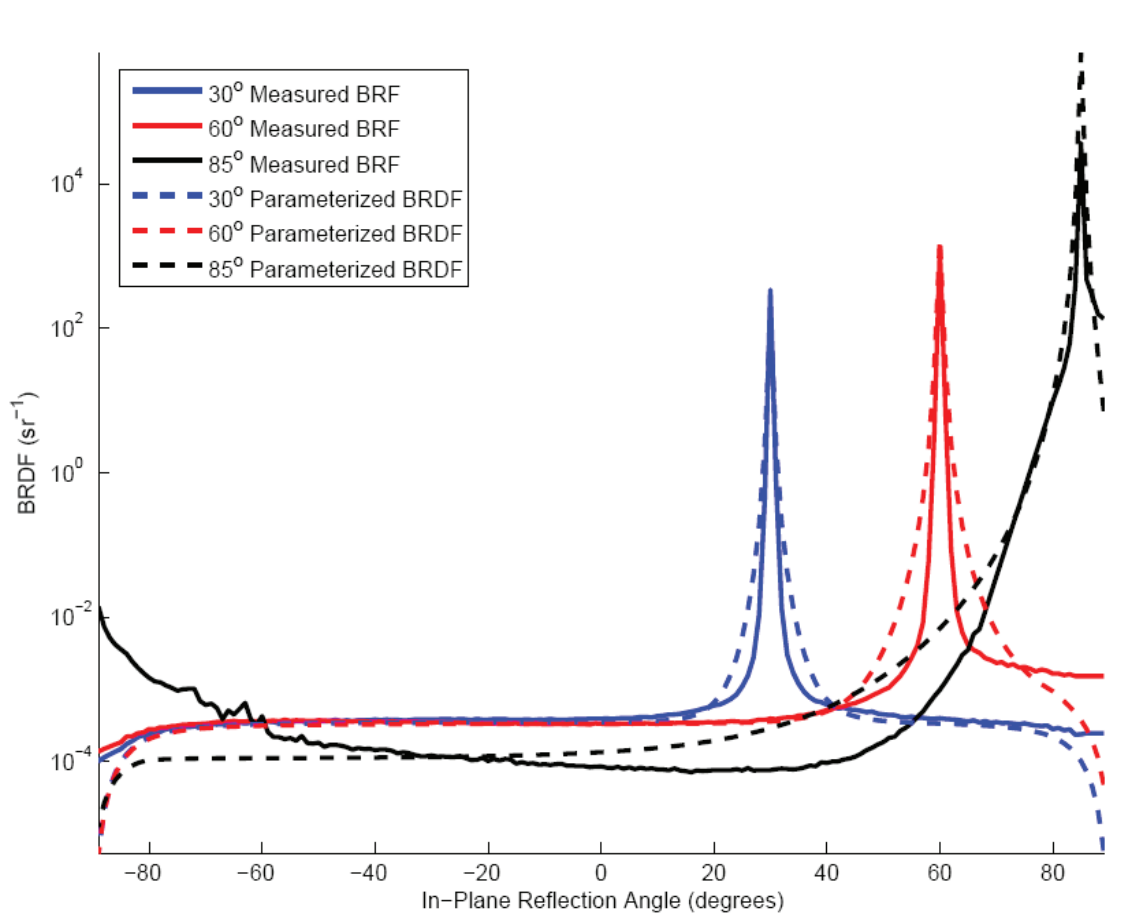


Figure 2.12: Empirical and parameterized BRDF for the gloss black surface, reproduced from [3, Figure 3.22 (a)].

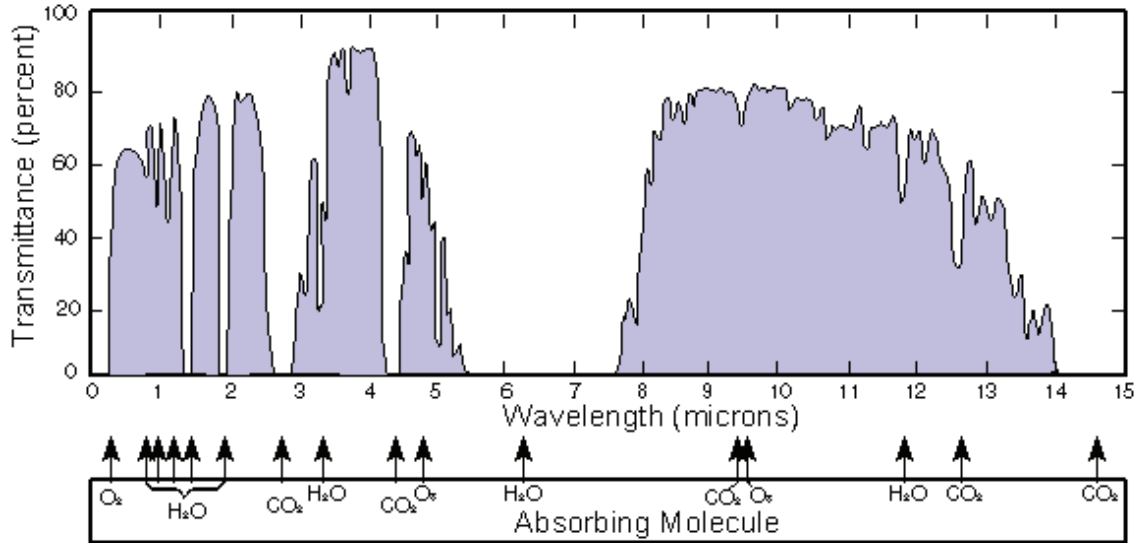


Figure 2.13: The spectral transmission of IR energy varies with wavelength as different molecules absorb the energy at various positions in the spectrum. Reproduced from [19, Figure 7-1.10].

2.4 Atmospheric Transmission

IR energy that propagates through the atmosphere experiences absorption and scattering due to the molecular and aerosol constituents. Water vapor, carbon dioxide, ozone and other minority gases all spectrally absorb radiation, and re-emit the energy as blackbody radiation at the ambient temperature. Absorption occurs spectrally as the IR wavelength matches the various electronic, vibrational or rotational transitions for each molecule. Thus, the absorption spectrum is very dependent upon wavelength, [19, 26], and is shown in Figure 2.13.

When designing a detection system, it is important to understand and exploit these spectral regions of high transmittance, as designing a detection system over a band where there is high absorption will significantly reduce the system's detection range. For this reason, systems are designed to detect in the short wave IR (SWIR) ($1 - 3\mu m$), MWIR ($3 - 5\mu m$) or LWIR ($8 - 12\mu m$) regions.

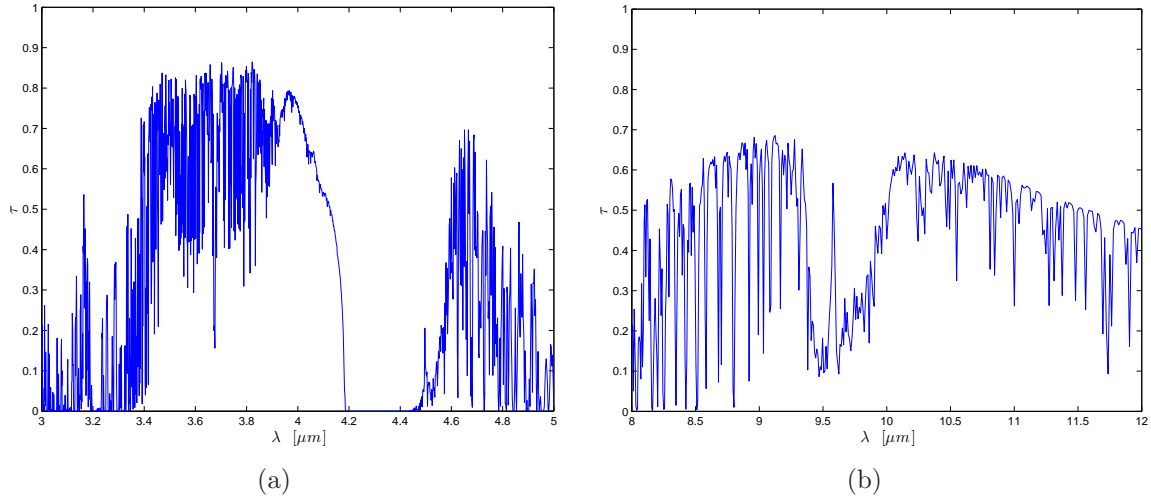


Figure 2.14: An example transmission spectrum for the (a) MWIR and (b) LWIR bands is shown. Note the transmission windows where IR radiation is not absorbed. The path length of this simulation was set to infinity at 45° elevation on a cloudless summer day.

Software programs such as MODTRAN predict the spectral transmission as a function of geographical position, time of day, weather conditions, and path position and length. One such simulation in the MWIR and LWIR bands is included in Figure 2.14 for reference.

2.5 Monte Carlo Integration

Monte Carlo integration is a technique used to numerically evaluate integrals, and is more efficient than standard numerical quadrature techniques for multi-dimensional integrals.

2.5.1 Numerical Quadrature. To evaluate the integral, I , of $f(x)$ over the domain $x \in [a, b]$ analytically, the expression is,

$$I = \int_a^b f(x)dx \tag{2.27}$$

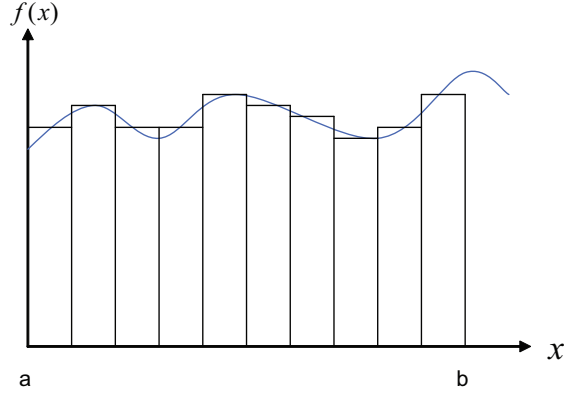


Figure 2.15: Deterministic numerical quadrature where the function is sampled at evenly spaced intervals and approximated by a rectangle across the interval.

and solve by integrating the function $f(x)$ and applying the limits. However, this approach becomes infeasible for multidimensional functions and ones which cannot be integrated analytically. Numerical integration is performed by quadrature, where the continuous function is approximated by rectangles in one dimension, solid rectangles in two dimensions, and so on.

Each domain must be divided into N usually equal sized regions, and the value of $f(x)$ is evaluated at each x_i point. Figure 2.15 illustrates the one dimensional case which can be extrapolated into further dimensions as required. Each value $f(x_i)$ is then scaled by a weighting factor, w_i , and summed to evaluate the integral. For uniform divisions, the weighting factor is $w_i = (b - a)/N$ and is constant $\forall i$. The estimate, \hat{I} , of Equation (2.27) then becomes

$$\hat{I} = \sum_{i=1}^N f(x_i)w_i = \sum_{i=1}^N \frac{f(x_i)(b - a)}{N} \quad (2.28)$$

which calculates the mean value of $f(x)$ over the domain and multiplies by the width of the domain. Intuitively, as N increases, \hat{I} becomes a closer estimate of the analytical result, I . The distance between I and \hat{I} can be measured by the variance in the solution, σ^2 .

To extend numerical quadrature into d dimensions, N^d samples of the function are required.

2.5.2 Monte Carlo Method. Monte Carlo integration is similar to the numerical case, the one difference is that the samples, x_i , are taken from a random variable, not uniform divisions. The advantage of this method is its efficiency in evaluating multi-dimensional integrals where some number of samples ($n < N^d$) can achieve a result where \hat{I} is a suitable estimate of I .

The estimate for Monte Carlo integration is very similar to Equation (2.28), except the weighting factor differs. The $(b - a)$ term is replaced with $1/p(x_i)$ in Equation (2.29), where $p(x_i)$ is the probability density function (PDF) of x_i occurring in the integral domain.

$$\hat{I} = \frac{1}{N} \sum_{i=1}^N \frac{f(x_i)}{p(x_i)} \quad (2.29)$$

This substitution remains consistent with Equation (2.27) as the integral of $p(x_i)$ over the uniformly sampled $(b - a)$ region

$$(b - a) \Rightarrow \frac{1}{p(x_i)} \quad (2.30)$$

$$\int_a^b p(x_i) dx = \int_a^b \frac{1}{(b - a)} dx = 1 \quad (2.31)$$

which is required of $p(x_i)$ (as a valid PDF).

A development of this probability theory is contained in [5, section 3.4], with more detailed mathematical proofs developed in [6]. The definition concludes with a measure of the variance in \hat{I} that reduces as N increases, is detailed in Equation (2.32).

$$\sigma^2 = \frac{1}{N} \int \left(\frac{f(x)}{p(x)} - I \right)^2 p(x) dx \quad (2.32)$$

2.5.3 *2-Dimensional Monte Carlo Integration.* Extending the technique into two dimensions is a trivial extension of Equation (2.29),

$$I = \iint f(x, y) dx dy \quad (2.33)$$

$$\hat{I} = \frac{1}{N} \sum_{i=1}^N \frac{f(x_i, y_i)}{p(x_i, y_i)}. \quad (2.34)$$

2.5.4 *Monte Carlo Integration Example.* As an example, let $f(x) = 5x^4$ and $p(x) = 1$ over the domain $[0, 1]$, which implies the following integral and its estimate from Equation (2.29):

$$I = \int_0^1 5x^4 dx = 1 \quad (2.35)$$

$$\hat{I} = \frac{1}{N} \sum_{i=1}^N 5x_i^4 \quad (2.36)$$

The variance from Equation (2.32) becomes

$$\sigma^2 = \frac{1}{N} \int_0^1 (5x^4 - 1)^2 dx = \frac{16}{9N}. \quad (2.37)$$

Figure 2.16 plots the integral estimate of Equation (2.35) using Equation (2.36) and shows the accuracy of the estimate increasing with the number of samples, N , whilst remaining inside the bounds of the variance estimate calculated with Equation (2.37).

The usefulness of Monte Carlo integration will become evident in Section 3.3.

2.6 *Spherical and Hemispherical Geometry*

Figure 2.2 defined the geometry of the BRDF parameters. Several concepts and data display methods will be used in this thesis, and this section discusses the utility of this method. The BRDF, after ignoring the wavelength domain, is a four

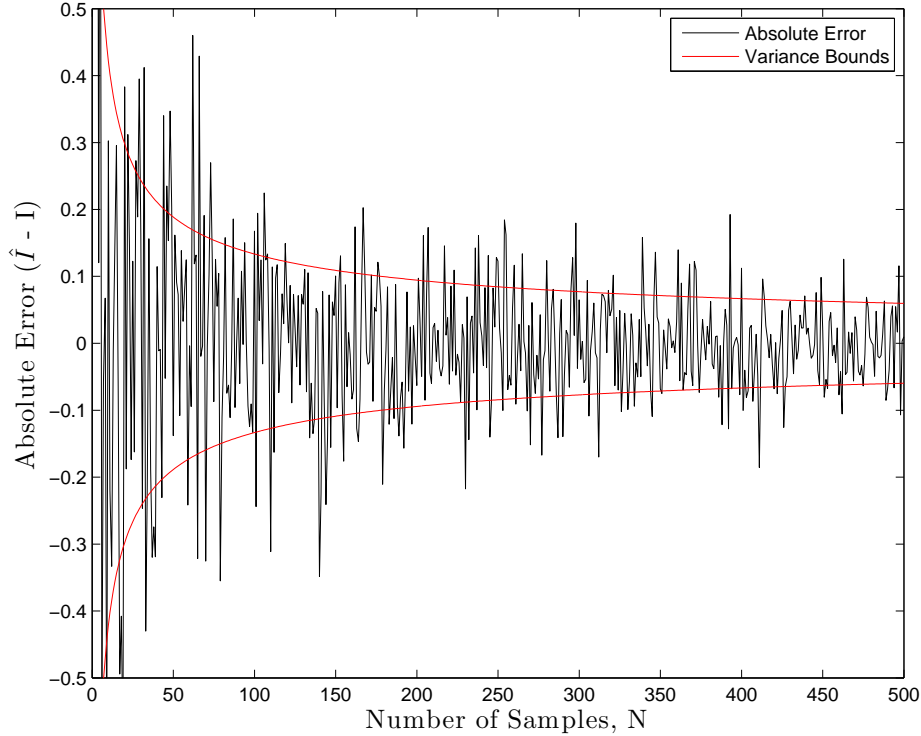


Figure 2.16: Monte-Carlo integration example. The variance of the solution decreases as the number of samples increases, staying within the variance bounds.

dimensional function. It contains two domains (incident and reflected hemispheres) of two dimensions each. Each hemisphere has two dimensions, and is represented by the spherical geometry variables $\phi \in [0 : 2\pi]$ and $\theta \in [0 : \pi/2]$ which map out the hemisphere.

A solid angle, Ω , is defined by the area subtended on the hemisphere by the angular region of interest, and has units of steradian (sr). Assuming the hemisphere's radius is one, the surface area of a hemisphere is then $2\pi r^2 = 2\pi$, implying there are 4π steradians in a whole sphere. The area creating the solid angle can be of any shape, only the magnitude of the area is important.

2.6.1 Hemispherical Integration. In most cases, there is a requirement to integrate the incident irradiance, at a point on the model's surface, over the hemisphere to calculate the reflected radiance in the direction of the observer. When numerically

calculating a hemispherical integral, both domains are treated as if they are in cartesian form. Thus, the differential solid angle, $d\omega$, uses the Jacobian transform from spherical to cartesian coordinates. When integrating the BRDF over the hemisphere, the differential solid angle (centered on the direction Θ),

$$d\omega_{\Theta} = \sin(\theta)d\theta d\phi \quad (2.38)$$

transforms the spherical integral into a form, which the computer can calculate,

$$\int_{\Omega} f(\Theta)d\omega_{\Theta} = \int_0^{2\pi} \int_0^{\pi/2} f(\theta, \phi) \sin(\theta)d\theta d\phi. \quad (2.39)$$

2.7 Chapter Summary

The background theory and concepts discussed above will be expanded and applied to the IR simulation application in Chapter III. Chapter III also includes the methods and algorithms used to compute the IR signature simulation.

III. Development of the Infrared Signature Simulation

This chapter describes the method, procedures and ideas that will be simulated in Chapter IV. The background theory presented in Chapter II is expanded in detail and is focussed towards the IR signature modelling application.

3.1 *Infrared Signature Components*

An IR signature is the signal that is emitted or reflected from a target (aircraft) across the whole IR spectrum. It contains thermal self emission from the target and reflections from the background. The background consists of earth and sky shine, solar reflections and atmospheric path radiance; all of these are reflected in some part from the target towards the detector. The target's composite signal is then attenuated by the atmosphere due to scattering and absorption.

Additionally, the background itself provides a direct component. The background that is in the field of view (FOV) of the detector contributes through the path radiance to infinity and the path radiance between the detector and target.

For single-pixel detectors, the whole FOV is integrated into a single output, and for the target to be detected, it must have a greater magnitude than the background (or possibly less in a negative-contrast system). However, for imaging detectors, there is spatial information which can be used to detect targets. Adjacent pixels are compared to determine contrast, finding the edges of the target. If the resolution is sufficient, then algorithms can classify the type of target. However, this process requires a larger signal-to-noise ratio (SNR) than pure detection.

3.2 *Aircraft Model*

The aircraft or target being modelled must be represented quantitatively in some manner to allow algorithms and mathematical expressions to be applied and calculated, respectively. LCAIR uses a facetised approach, where the aircraft surfaces are broken (facetised or tessellated) into small flat polygons of at least three coplanar

vertices. The number of facets is arbitrary, however, the more facets, the better the approximation of the real aircraft. This facet-based approach is more commonly known as a wireframe model.

3.2.1 Wireframe Model. Each component of the real aircraft or target must be facetised. The resulting model should accurately represent the geometry for the simulation result to be representative of the real world phenomenon. To achieve this, each facet must be continuous to the next so there are no gaps where sample rays could miss an intersection between two facets. The wireframe facets are defined by three or four vertices (for a triangle or a quadrilateral, respectively) in a single 2D (coplanar) plane. The units are not important, however, to aid in the calculation of radiance later (with units of *watts per square meter per steradian*), meters are chosen as the base unit. In addition to the vertices, each facet must have several other parameters defined. The wireframe file contains all the information describing the aircraft (target) that is required by the propagation algorithm.

3.2.1.1 Normal. The facet normal defines the direction that the facet emits and reflects radiation. A condition of this is that all facets are only one-sided. The model must be continuous and enclose the volume of the aircraft completely, and all aircraft parts (especially thin parts) must be facetised into a volume with the normals facing out.

3.2.1.2 Center. The center of the facet is calculated by the arithmetic mean of the vertices in all three dimensions. The center is used to calculate the spherical angles (ϕ and θ) to and from the other facets. The irradiance and exitance distribution is assumed constant across an individual facet, with the center being used for the geometric point of calculation.

3.2.1.3 Reference Vector. The azimuthal domain is expressed from -180° to $+180^\circ$; the reference vector divides the positive and negative angles. The

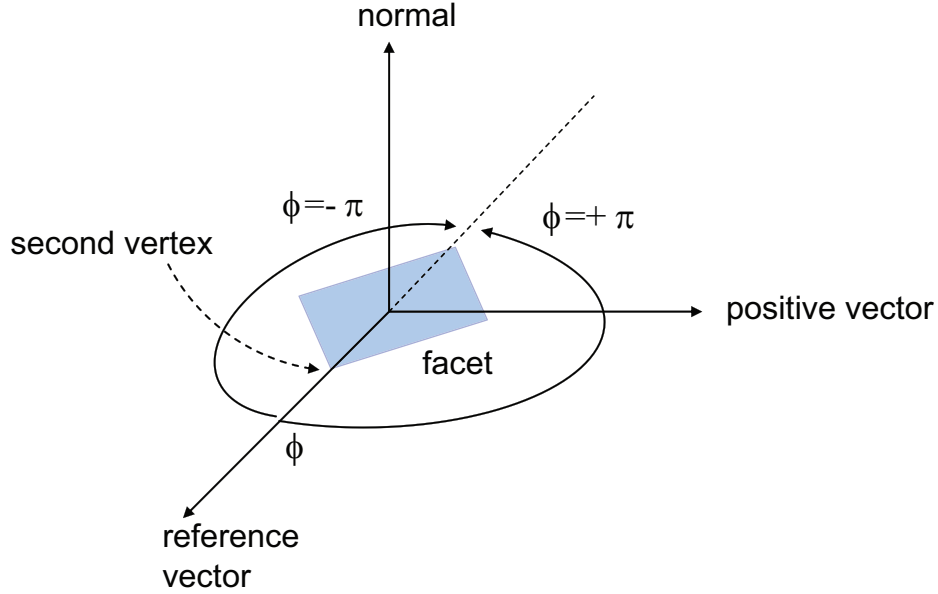


Figure 3.1: Sketch of the definition of the positive and negative azimuth domain values. The positive half always has the positive vector, as this defines a right handed coordinate system.

reference vector is calculated from the facet center to the second vertex, and is normalized to give a unit vector.

3.2.1.4 Positive Vector. The positive vector defines the positive 180° of azimuth and lies along the $[\phi = 90^\circ, \theta = 90^\circ]$ vector. It is calculated by a cross product to create a right handed coordinate system with the reference vector and facet normal. Figure 3.1 defines the positive and negative azimuthal values in relation to the reference and positive vectors.

3.2.1.5 Facet Type. Each facet is coded to indicate what it represents, whether a model (f), sky (s) or terrain (t) facet.

3.2.1.6 Material type. Surface treatment of the facet is very important as it affects the reflectance distribution of the facet. The material type is coded as the propagation algorithm must know what the surface treatment is. Material types available for simulation are gloss black painted aluminum, bare aluminum, and a per-

fectly diffuse surface. Other surfaces which are available, although not simulated are FS3411 Flat Blue Camouflage and FS3464 Gloss White as the Sandford-Robertson model parameterizations are listed in [23]. The Federal Standard Paint scheme (abbreviated as FSxxxx) is an attempt to standardize colors in the United States Federal Government to provide a way for engineers and manufacturers to reference, design and manufacture to one common paint scheme. FED-STD-595, [1], is the controlling document for the standard.

3.2.1.7 Temperature. As discussed in Chapter II, the temperature of a surface affects the blackbody radiation of a surface. Each facet must have a temperature assigned in Kelvin.

3.2.2 Blender 3D Program. The user needs a tool to create, edit and manipulate the wireframe model with ease. The software program Blender3D was used to create the wireframe and assign the facet type, material type and temperature to each facet.

An off-the-shelf product was primarily chosen for ease of use, but also because it comes with an import/export utility that can import many types of 3D wireframes that are available for aircraft. Autodesk 3D Studio Max® files are easily imported. Additionally, once the wireframe model is loaded inside Blender3D, the export utility is used to produce a data file for the `Matlab`® algorithm to read, containing the vertex and label format information for each facet. The data file in Blender3D is exported as a Wavefront (.obj) file. The settings required for this are shown in Figure 3.2.

Each facet is coded with the parameters that were defined in Section 3.2.1. The field options are listed in Table 3.1, and the label must conform to the format in Figure 3.3. An example is included for a bare aluminum model facet with a temperature of 300K. Figure 3.4 contains a screenshot of Blender3D, which shows the facet label format entry position in the top left of the textbox.

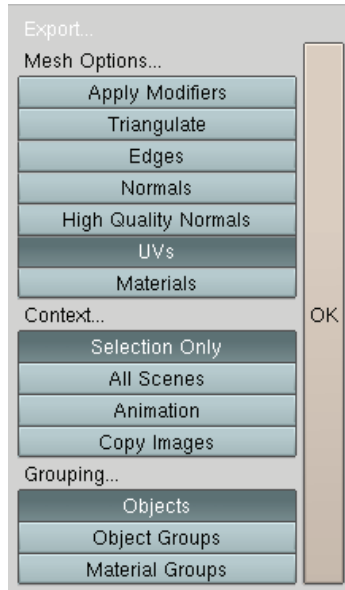


Figure 3.2: Screenshot of the Wavefront (.obj) export settings in Blender3D.

```
{facet type}*{material type}*{temperature}*{Blender3D misc}
f*bareAl*300*
```

Figure 3.3: The facet naming format must be typed exactly so the Matlab[®] import function can read the applicable fields. This example is for a bare aluminum model facet at a temperature of 300K.

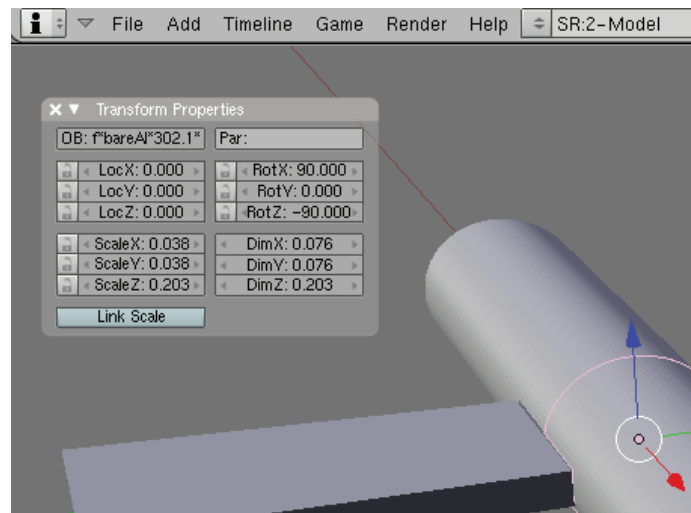


Figure 3.4: Screenshot of the cylinder model in Blender3D. The program makes editing and manipulating the wireframe model very easy.

Table 3.1: Facet label attributes for facet type, material type and temperature. These must be entered exactly into the textbox in Blender3D, or the `Matlab®import` function will crash.

Label Field	Format Options	Detail
Facet Type	f s t	model facet sky facet terrain facet
Material Type	glossBk bareAl diffuse1.0 diffuse0.5 diffuse0.0 modt#	Gloss black painted aluminum Bare aluminum Perfectly diffuse (Lambertian) blackbody, $\epsilon = 1.0$ Perfectly diffuse greybody, $\epsilon = 0.5$ Perfectly diffuse reflector, $\epsilon = 0.0$ MODTRAN generated path radiance
Temperature	T [K]	Temperature of facet in Kelvin
Blender3D misc	{blank}	Blender3D adds information to the label. All information to the right of the third asterisk (*) is ignored by the <code>Matlab[®]import</code> function.

3.2.3 Simulation Models. Three models are simulated in Chapter IV; the first is a cavity blackbody source. The second is a cylinder with wings, representing a notional aircraft shape. It is simulated in an IR range environment to demonstrate the applicability and accuracy of the various algorithms. The final model is based on an Airbus A340-300, and is simulated at a generic airport to calculate the apparent irradiance at a detector located outside the airport boundary. Other models are included in Appendix A, where analytical test cases are performed to quantitatively validate the algorithms.

3.2.3.1 Artificial Cavity Blackbody Source. Figure 3.5 shows a cavity model displayed in `Matlab®`. The cavity model is facetised into 400 facets and has a radius of $0.5m$. During the simulation, seven other cavities were simulated with varying aperture sizes. The eight different aperture sizes are created by removing more and more facets from the wireframe model. The number of facets removed are;

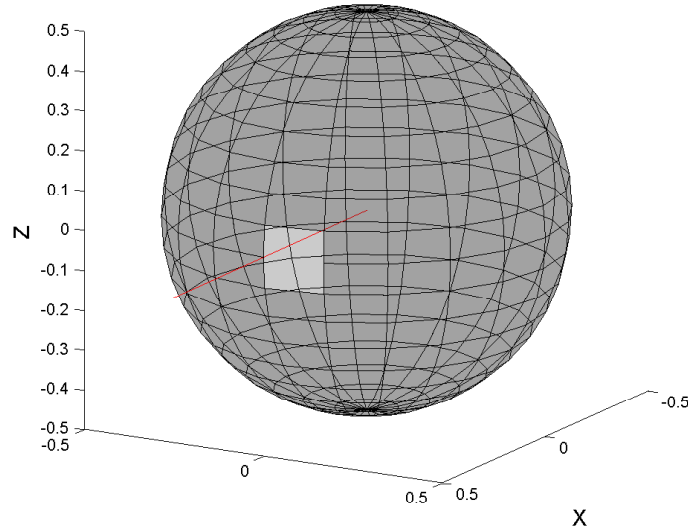


Figure 3.5: The artificial cavity blackbody source is modelled as a faceted sphere with 400 facets. In this case, two facets are removed to create the aperture.

2, 4, 8, 16, 24, 36, 60, and 80. Figure B.1 shows the different cavity aperture sizes. The cavity is set to 800 Kelvin and has an internal emissivity of 0.5.

3.2.3.2 Cylinder Model. The cylinder model was built in 2005 by Capt Bortle as a physical model to validate the original LCAIR code written by Capt Martinez in 2005. The model is constructed of aluminium and has dimensions as detailed in Figure 3.6. Detailed construction drawings can be found in [3] and photographs of the model are included in Figures 3.7 and 3.8. Figure 3.9 shows the cylinder model in the Blender3D program. The cylinder model is simulated in two configurations, bare aluminum and painted with gloss black paint. Table 3.2 lists the temperatures that were measured in the IR range simulations by Bortle.

3.2.3.3 Airbus A340-300. The third model to be simulated is the Airbus A340-300. This aircraft was chosen as a typical large commercial airliner. A sample wireframe model was imported into Blender3D. From there, the A340-300

Table 3.2: Cylinder Model Surface Temperatures.
Reproduced from [3].

Position	Gloss Black Temperature [K]	Bare Aluminum Temperature [K]
Nose	292.1	301.7
Front Fuselage	293.1	302.1
Rear Fuselage	294.2	303.2
Left Wing Front	301.6	303.6
Left Wing Rear	298.2	303.6
Right Wing Front	304.2	303.7
Right Wing Rear	299.1	303.7

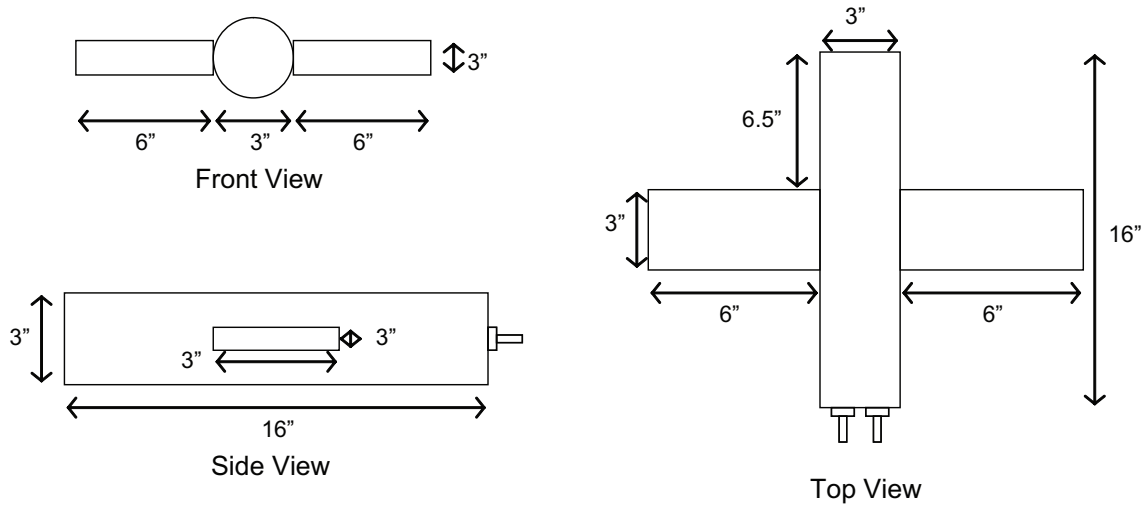


Figure 3.6: 3-View drawing of the cylinder model, showing the dimensions from the front, side and top views. Adapted from [3, Figure 3.1].



(a)



(b)

Figure 3.7: A photo of the cylinder model showing (a) the internal construction of the cooling coils and the thermal electric heater input wires, and (b) another photo showing the cylinder model with the cover attached. In this figure the model is not painted, which is the surface treatment for the bare aluminum simulations in the IR Range. Reproduced from [3, Figure 3.2].

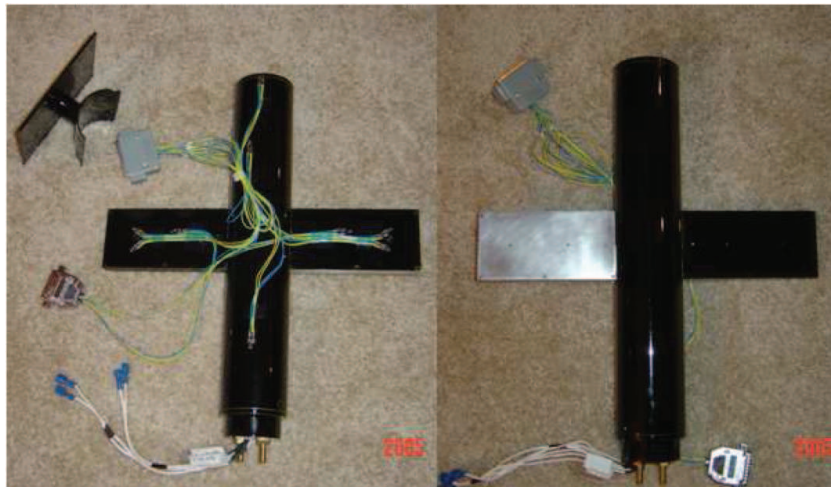


Figure 3.8: Photo of the cylinder model with the gloss black paint surface treatment applied. Note the underside of one wing is left bare to provide some contrast in the IR range simulations. Reproduced from [3, Figure 3.12].

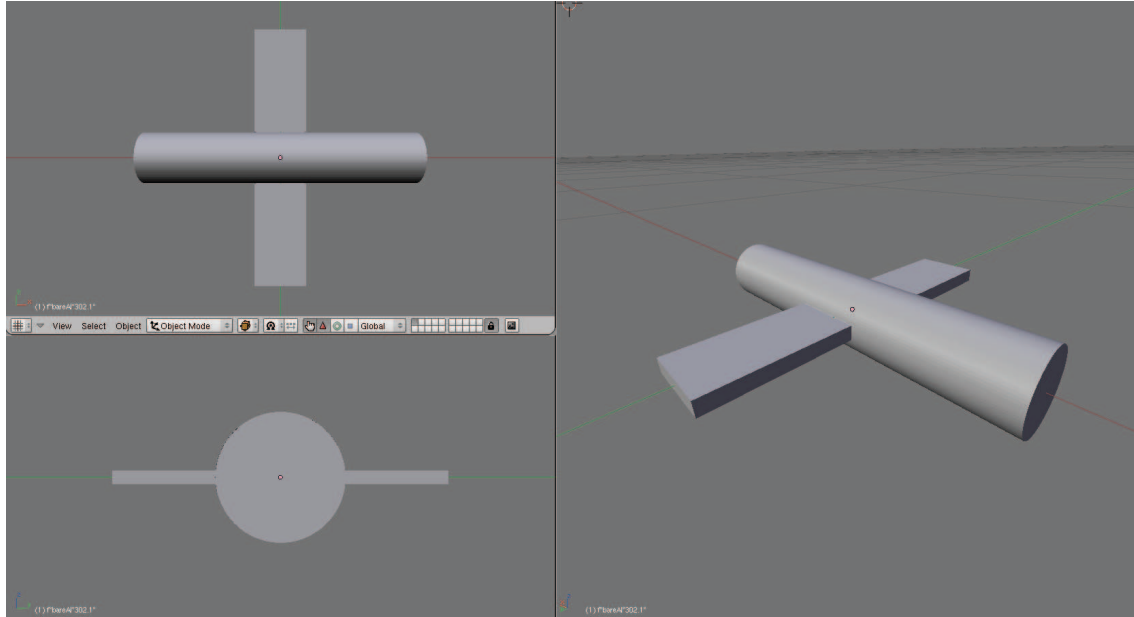
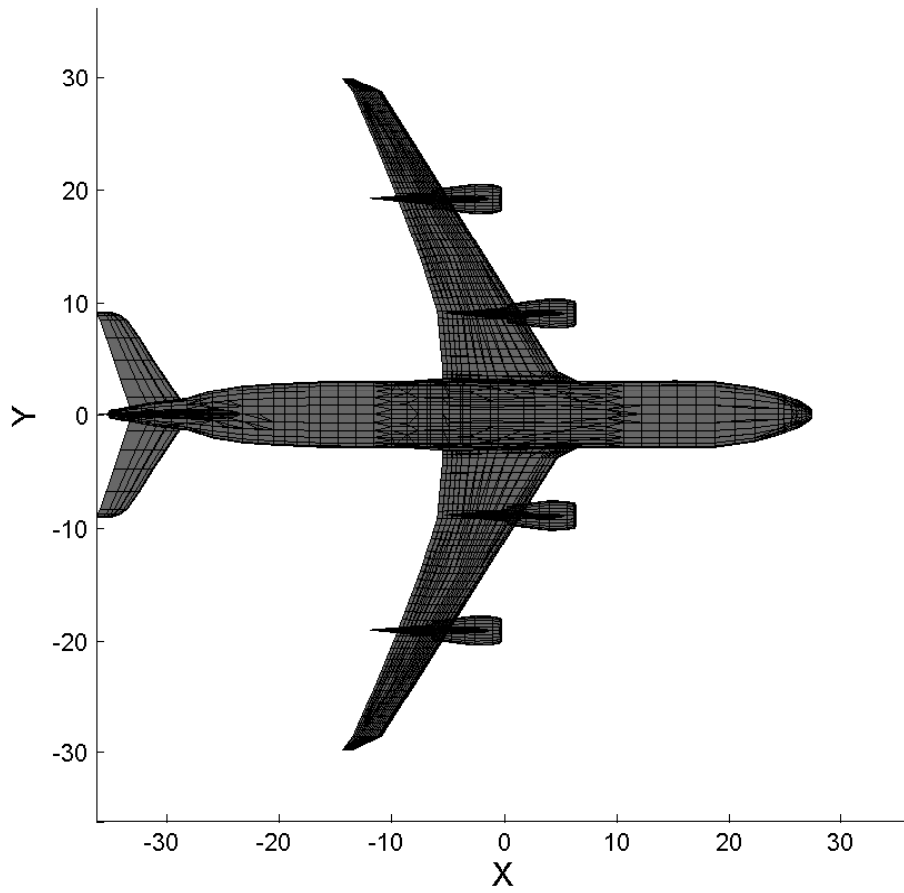


Figure 3.9: A screenshot of the cylinder model in the Blender3D program, viewed from different orientations.

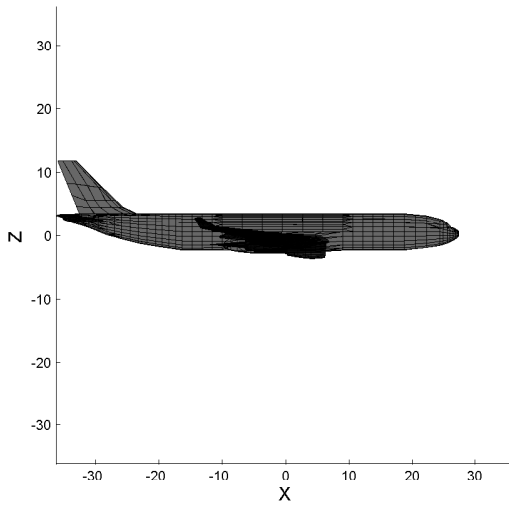
model is treated exactly the same as the cylinder model with respect to the algorithms and simulation procedures. Figure 3.10 shows the aircraft model in **Matlab**[®].

During the simulations, the aircraft's surface treatment will be bare aluminum, to approximate the specularity of commercial aircraft surface finishes. The aircraft fuselage, wings, stabilizers, engine pylons and cowls are set to 300K, the ambient temperature. The majority of the thermal signature is simulated to be emitted from the engine exhaust plume and the visible hot parts in the turbine cavity. The exhaust plume is modelled as a simple cone at a temperature of 500K. Figure 3.11 shows the exhaust temperature profile for a turbofan engine, and is assumed to be similar to the A340-300 engine. From the figure, the 500K profile would extend to about 20 feet from the tailpipe exit plane; hence, the exhaust cone in the model is set to 20 feet in length.

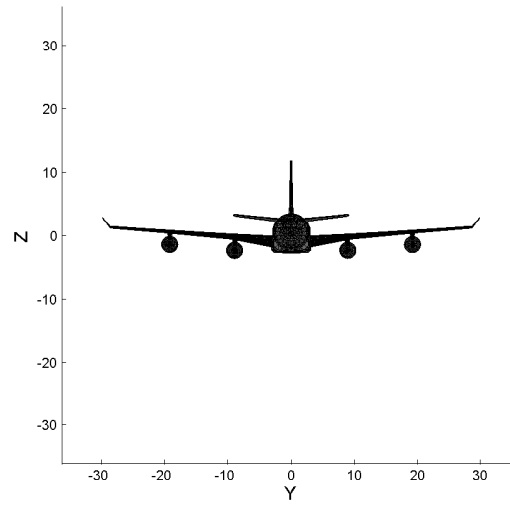
Additionally, the engine hot parts are modelled by an annulus that connects the exhaust cone to the engine cowl. This simulates the view of the engine from behind where the observer can see into the engine cavity; the temperature is set to 800K.



(a) Top View



(b) Side View



(c) Front View

Figure 3.10: The Airbus A340-300 model is imported into `Matlab`[®] and displayed from three angles. Note the varying magnitude of the visual cross-section from the three different angles.

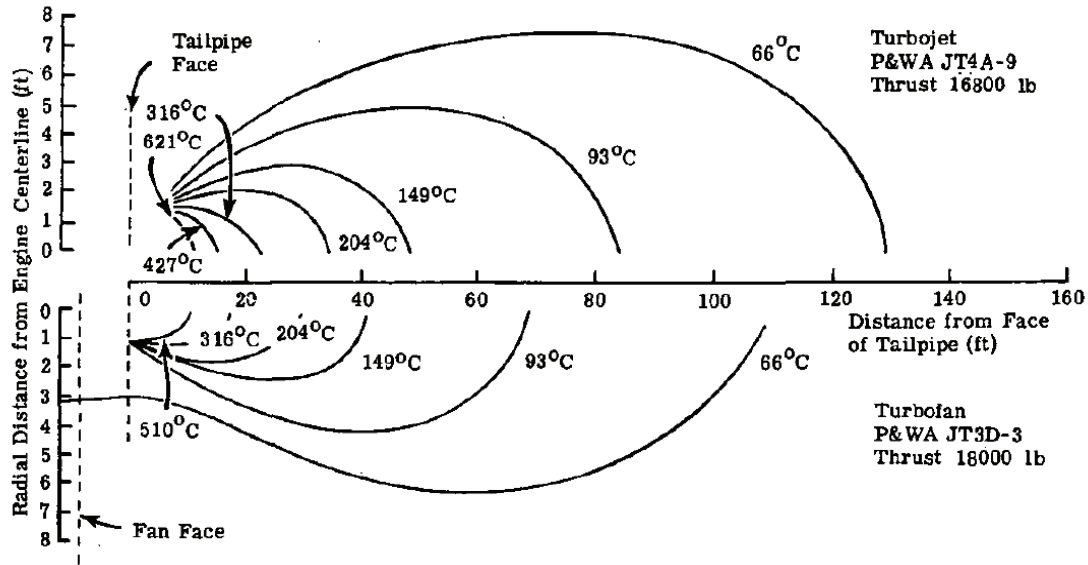


Figure 3.11: Engine exhaust temperature contours for the Boeing 707 turbofan and turbojet engines. Reproduced from [26, Figure 2-72].

This annulus is not visible forward of the tailpipe exit plane; which again, simulates the view into the engine cavity.

3.2.4 Hemispherical View. The hemispherical view of any point on the model's surface refers to the geometry in the hemisphere that is visible from that point. Viewable objects include other model surfaces or background, whether terrain or sky. The hemispherical view has information of where (as a function of ϕ and θ) and how large (size of solid angle) each object is. The *view* is displayed in a 2D figure with the `colormap` referenced to the 3D model facet index. Figure 3.12 shows the *hemispherical view* of facet A from the example geometry of Figure 2.2, and Figure 3.13 shows the view of the more complex geometrical setup of the cylinder model from an arbitrary facet on the wing leading edge.

Displaying BRDF values over the hemisphere requires a similar 2D figure. In this case, one of the two domains must be fixed, to allow the function to be evaluated across the other. The most common display is when the reflected domain is fixed at some observation position and the BRDF is calculated across the whole incident

domain; an example with $\theta_i = 30^\circ, \phi_i = 100^\circ$ is shown in Figure 3.14. Recall that under the theory of reciprocity from Section 2.3.1.1, it does not matter which domain is fixed; the result will be the same as described in Equation (2.6).

3.3 Integrating the BRDF

Section 2.3.2 discussed the different integral forms of the BRDF; the most useful one is the DHR, where the BRDF is integrated over all exitant angles. This hemispherical integration will be required by the propagation algorithms of Section 3.5. Hemispherical integration is required when integrating the incident irradiance of any facet. The BRDF must also be hemispherically integrated to scale that incident irradiance. Computer simulations require all calculations (including integrals) to be computed numerically (discretely). The caveat to this approach is that the function must be suitably sampled during the integral to avoid aliasing problems that give an incorrect answer. This sampling issue is the same as discussed in Section 2.5, where Figure 2.16 shows the aliasing error decreasing as the number of samples increases.

The BRDF function must be suitably sampled during integration to ensure that the function's characteristics are observed throughout the domains. The Sandford-Robertson BRDF model, being a fractional specular model, assumes that the surface exhibits some specular behavior. It is this specular nature that requires careful sampling when integrating the function. Figure 2.9 demonstrated the specular behavior of the surface where the diffuse floor's magnitude is 10^{-2} and the specular peak is 10^{+4} . This is a very large range across the function's domain. The region where the large values (10^{+1} and above) exist is also over a small angular region of approximately 5° in θ_r , which demonstrates the specular nature of the aluminum surface. Note the gloss black surface, although with a considerably lower total reflectance than aluminum, is also highly specular; the angular region of large values (10^0 and above) is also 5° in θ_r .

Having to numerically integrate this function creates a computational problem. A design goal of any simulation is low computation time, hence, the number of samples

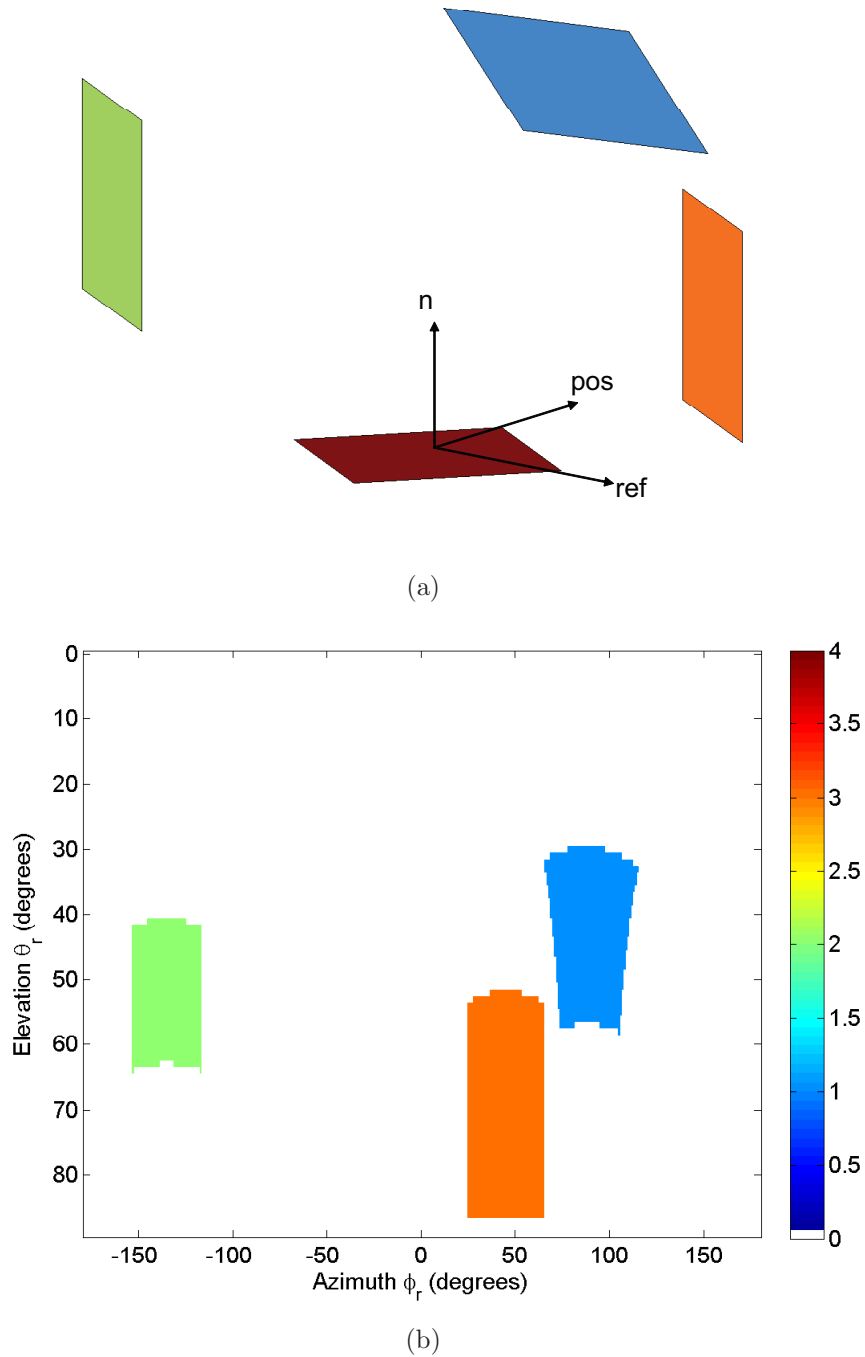
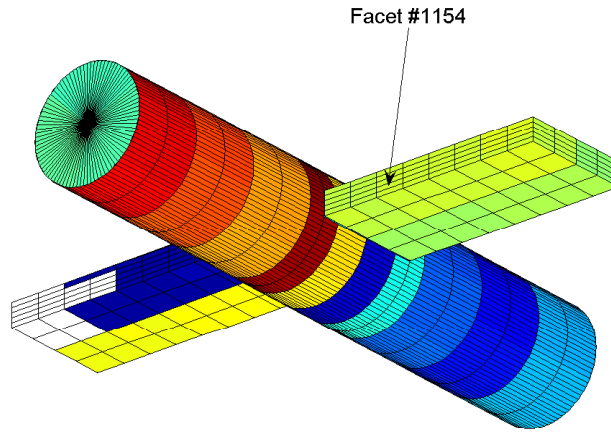
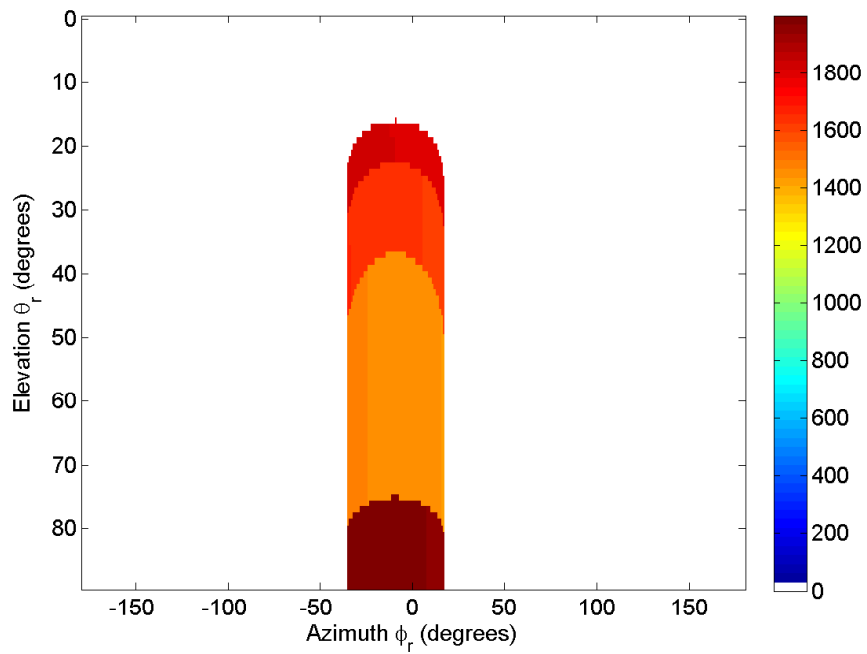


Figure 3.12: The geometry of a simple setup is shown in (a). The colormap references to the facet index number. Note the region in ϕ and θ that each of the other facets occupy in (b). Also, observe the spherical-to-cartesian conversion effect, which makes square facets have curved edges in the hemispherical view representation.

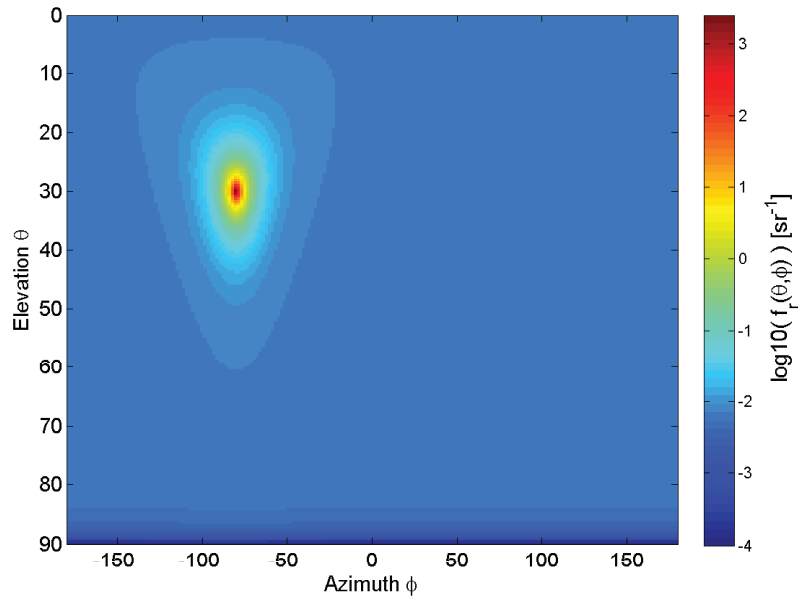


(a)

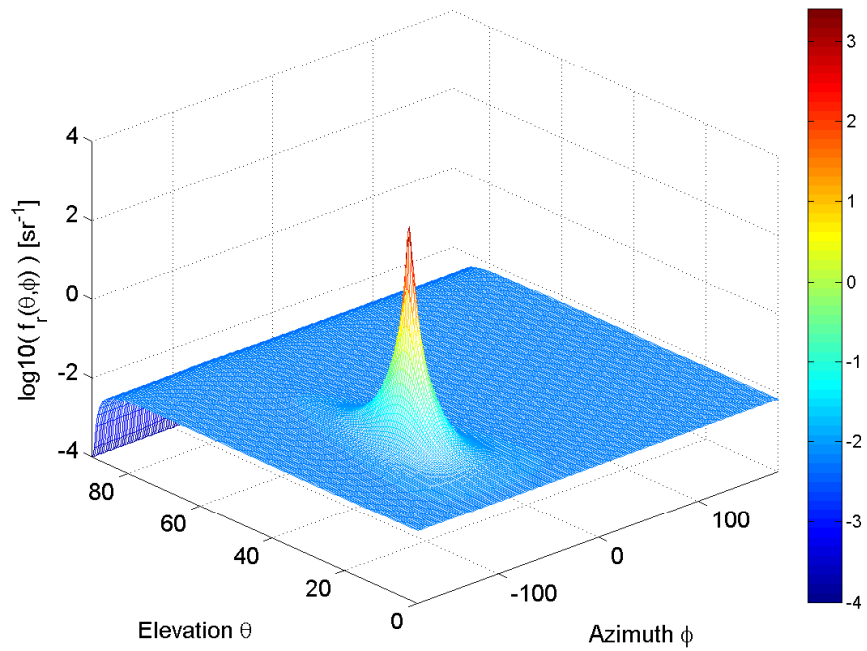


(b)

Figure 3.13: (a) Geometry of the cylinder model. The colormap is referenced to the facet index number. (b) The hemispherical view of a wing leading edge facet (#1154) from the cylinder model. Note the region where the model facets exist, everywhere else is background.



(a)



(b)

Figure 3.14: (a) The BRDF is represented in 2D format. This data structure is a 2D matrix that contains values as a combination of azimuth and elevation dimensions. (b) The BRDF is shown in 3D here for clarity. Note the log scale in the y-axis and colormap.

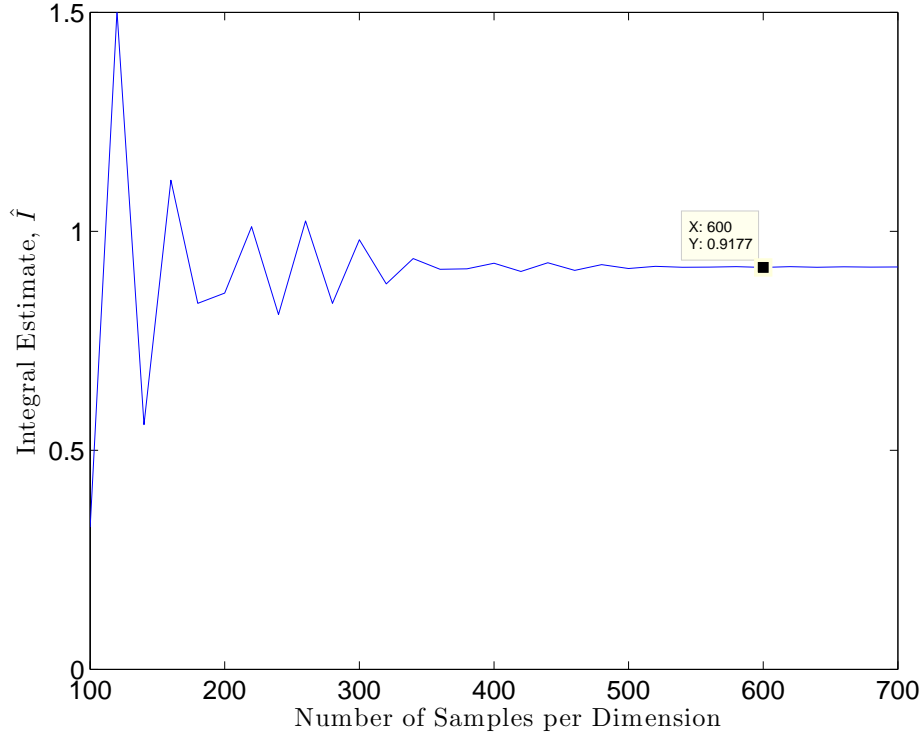


Figure 3.15: Integrated BRDF of bare aluminum ($\theta_i = 30^\circ, \phi_i = 100^\circ$) in the long wave IR ($8 - 12\mu m$) with varying sample resolution in the azimuth and elevation domains. The DHR (reflectance) for LWIR bare aluminum with $\theta_i = 30^\circ$ is 0.93.

per integration domain must be kept as low as possible to reduce computation time. However, this need is balanced against the requirement to adequately sample the function. Recall from Equation (2.8), the integral of the BRDF over all reflected angles must equal the reflectance at that reflected elevation angle. Simulations were performed by calculating the DHR from the BRDF with varying resolution across the azimuth and elevation domains to determine the sampling resolution required to achieve an accurate result, whilst keeping the computation time minimized.

Figure 3.15 shows the DHR result for sampling resolutions of 100 to 700 samples per dimension. Note that the number of samples is per dimension, thus, to integrate the BRDF across ϕ_r and θ_r (two dimensions) requires N^2 samples. From Figure 3.15, 500 samples per dimension are required for an accurate result, thus, $500^2 = 250,000$

samples are actually computed. This number of samples is prohibitive for a timely simulation, even with a single bounce simulation, as each facet's observed radiance takes minutes to calculate. The relatively simple cylinder model has around 2,000 facets; with several minutes per facet, a single bounce simulation will take days! Thus, an optimized result must be found.

As an aside, notice in the result of the BRDF integrated DHR measurement in Figure 3.15; the solution converges on 0.917, which is lower than the empirically measured DHR of 0.93 from Figure 2.7. This difference results from the fitment of the BRDF model parameters to the empirical BRDF curves. It can be seen that the parameterized BRDF curves in Figure 2.9 fall under the empirical measurement everywhere except the specular peak. When the parameterized curve is integrated, the result is less (owing to the lesser *area under the curve*). The opposite can be demonstrated for the gloss black case (Figure 2.12), where a significant proportion of the specular peak remains above the empirical curve, whilst the diffuse floors are relatively equal.

Importance-sampled Monte Carlo integration and numerical quadrature will now be investigated to search for the optimum numerical integration technique for this IR signature simulation application.

3.3.1 Importance Sampled Integration. The blind numerical integration technique simulated above has no *a priori* information about the BRDF distribution. In this case, the majority of samples are wasted, especially when the BRDF resembles a delta function where the values of any appreciable magnitude are so closely located.

A more efficient calculation method is to sample the function with a density that is proportional to the value of the function, where the peaks are sampled many more times than the lower values. This method places *importance* on the larger values of the function as they have a greater bearing on the result. Recall that when numerically integrating, a weighting factor $1/p(x_i)$ must be applied to the function's sampled value. The value of $p(x_i)$ is the probability that the function will be sampled

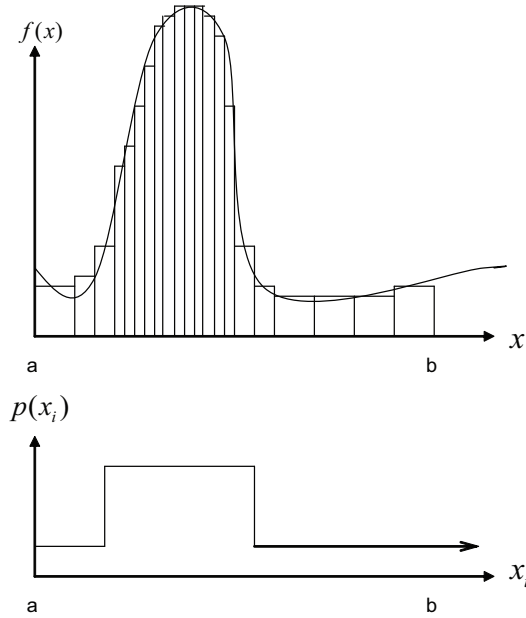


Figure 3.16: Integration with importance sampled domain. The $p(x_i)$ function is representative only, and it is not meant to specifically depict a piecewise function. The choice of the distribution for $p(x_i)$ is an important component of achieving the fastest convergence.

at that point, and the higher-probability sample values must be weighted by a larger factor to account for them being closely spaced. The region of the function with a higher probability of being sampled will then have more samples compared to the other regions, as shown in Figure 3.16, where the error introduced by the rectangular approximation is much less.

The choice of distribution for $p(x_i)$ should, optimally, be related to the function itself. The perfect $p(x_i)$ is then,

$$p(x_i) = \frac{|f(x)|}{\int_D f(x)dx} \quad (3.1)$$

where the function itself (when converted to a probability distribution function) integrates to one. Whilst this is the perfect $p(x_i)$, which will result in the variance of

Equation (2.32) equaling zero, it also requires knowledge of the integral of the BRDF,

$$\int_D f(x) dx = I \quad (3.2)$$

which is usually the object of the numerical integration estimate, \hat{I} .

3.3.2 Monte Carlo Integration. Monte Carlo integration, introduced in Section 2.5, is the term for the technique where the samples along one or more dimensions are generated with a certain distribution, $p(x_i)$.

From the previous section, the exact integral, I , is achieved with the perfect distribution from Equation (3.1). However, the key is being able to generate samples from the $p(x_i)$ distribution. The most efficient way is to use the inverse Cumulative Distribution Function (CDF) method, where a uniform random variable is transformed into the distribution of choice. This method, however, requires an expression for the CDF of the random variable, which is based on the BRDF of the specific surface treatment. Section 2.3.4 detailed the method of calculating the BRDF value using the four parameters and the equations defined in [23], however, the complexity of the BRDF model prevented an analytical expression of the CDF (matching the reflectance distribution of the BRDF) from being developed. In theory, the analytical CDF is

$$CDF(\theta_i, \phi_i, \theta_r, \phi_r) = \int_0^{\theta_r, \phi_r} \left(\frac{|f_r(\theta_i, \phi_i, \theta_r, \phi_r)|}{\int_D f_r(\theta_i, \phi_i, \theta_r, \phi_r) d\theta_r d\phi_r} \right) d\theta_r d\phi_r. \quad (3.3)$$

Other simpler BRDF models are able to be integrated analytically; however, the Sandford-Robertson model is being used in this case.

An analytical expression for the CDF is required to generate samples quickly and efficiently. A method of developing samples to a distribution without an analytical CDF is called *rejection sampling*. Rejection sampling is where uniform samples are generated in $N+1$ domains, where N is the number of domains in $p(x)$. The samples

are then tested against the required distribution, where if they fall under the desired $p(x)$ curve, they are accepted. A more detailed description of this technique and other generation techniques can be found in [6]. Despite this technique being available to generate samples, the delta function-like distribution of values in the BRDF makes this method *extremely* inefficient, and it is not chosen. The location of the BRDF peak is different for each evaluation of the reflected radiance integral, which would make even a precalculated look-up table method inaccurate.

3.3.2.1 Importance Sampled Normal Distribution. Although a BRDF-based CDF was not found, an attempt to integrate using a normally distributed approximation was performed. The normal distribution was chosen as its CDF is well known; thus, samples can be calculated easily. Figure 3.17 shows the convergence of \hat{I} using the normal distribution approximation. The integral approximation begins to converge; however, at 250,000 samples, the technique has still not achieved a suitable accuracy. This number of samples is clearly time prohibitive, and this technique is rejected.

3.3.2.2 Stratified Uniform Distribution. Another adaptation to the Monte Carlo case is stratified sampling, where the function's domain is divided into several regions where different sampling resolutions can be used in each. The regions can be sampled with uniform distributions as depicted in Figure 3.16.

The first region is defined as the function's peak centered on the specularly reflected point with a width of 20° in elevation and 40° in azimuth. However, the statistical nature of a uniform random variable causes the technique to break down as the uniformly generated variable is not purely uniform. The effect of this approximation and lack of uniformity is demonstrated in Figure 3.18, where a suitable accuracy is not reached after 500,000 samples. Special algorithms exist for generating better distributed uniform random variables, however, they were not investigated as the numerical quadrature section below proves to be far superior. Examples of

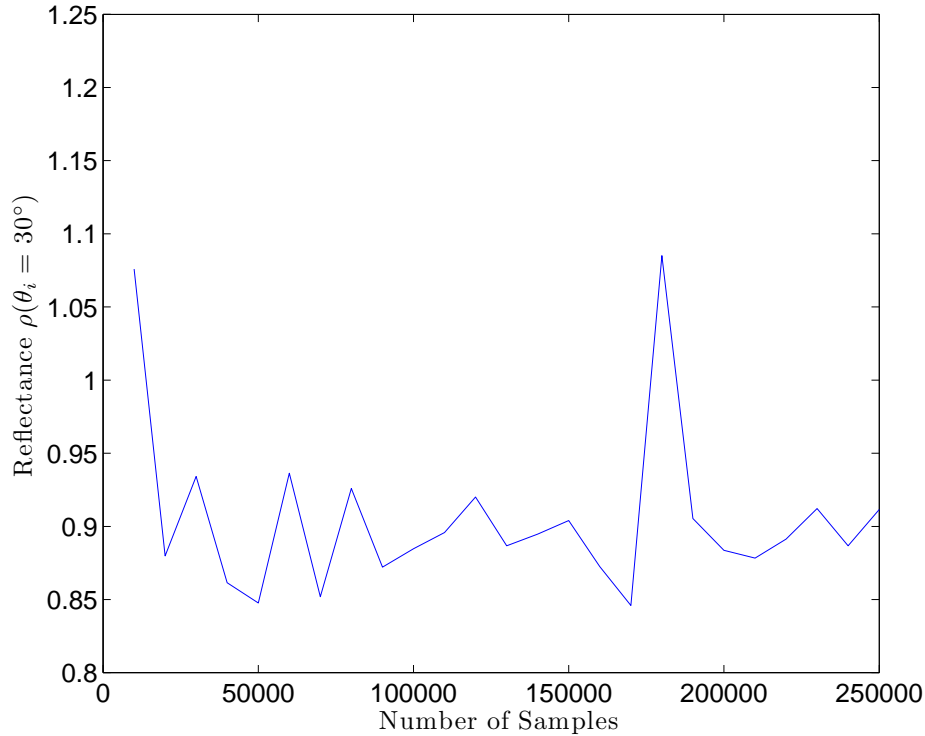


Figure 3.17: BRDF integration with a normal distribution approximation. Note how after 250,000 samples, the approximation has not suitably converged to the correct result.

these optimized distributions can be found in [6], where one technique is based on the Halton sequence of pseudo random numbers.

3.3.3 Stratified Numerical Quadrature. The advantage of statistical techniques comes from the law of large numbers, and is only realized when the number of samples becomes *large*. It has been demonstrated that even 500,000 samples is not suitably *large* enough when using this technique for this application.

A variation of the stratified uniform distribution is simply, stratified numerical quadrature. In this case, the same regions as Section 3.3.2.2 were chosen and integrated with numerical quadrature. Figure 3.19 shows the convergence of the peak region integral approximation, whilst Figure 3.20 shows the convergence of the outer region integral.

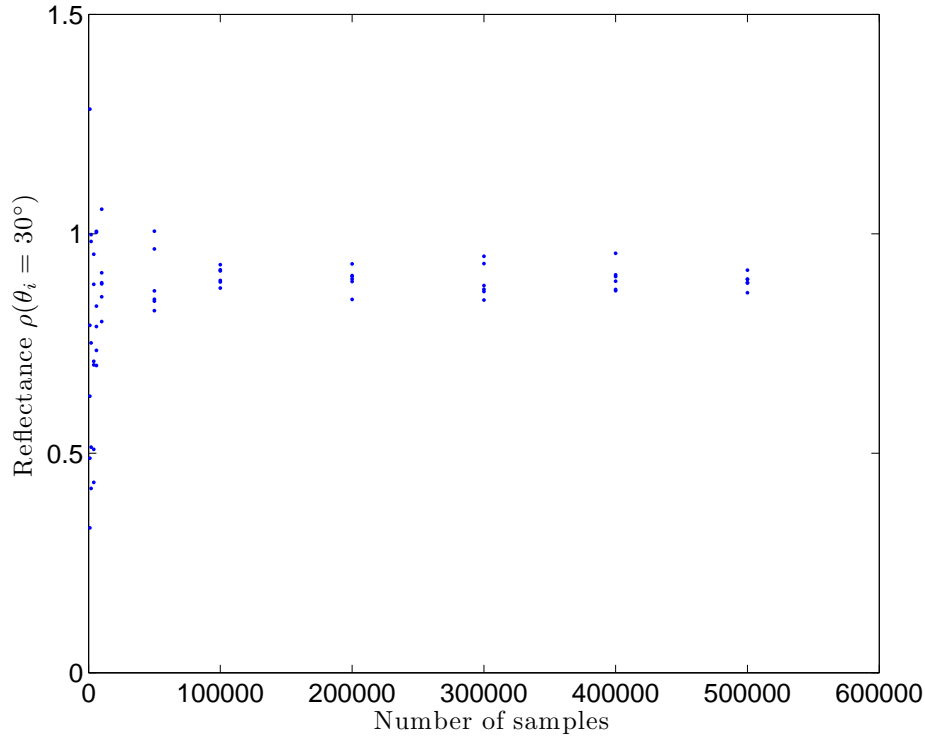


Figure 3.18: BRDF integration with a stratified uniformly distributed approximation. Note how after 500,000 samples, the approximation has not suitably converged to the correct result. A single dot represents one simulation at that number of samples. If the dots are widely spaced, then subsequent simulations provide different results, and hence, a large variance in the solution.

This method is far superior to those previously simulated. The advantage of stratified numerical quadrature is that the peak is sampled at a higher resolution than the rest of the domain. To sample at this resolution across the whole domain would require many samples, which was shown in Section 3.3.

3.3.4 Geometry Sampling. In addition to integrating the BRDF correctly, the hemisphere must also be sampled at a high enough rate to locate the edges of each facet. Figure 3.21 shows the number of samples required to sample the facet’s radiance when integrating across the BRDF. The figure shows that around 200 samples per dimension are required for a correct result. This sampling rate is required as each

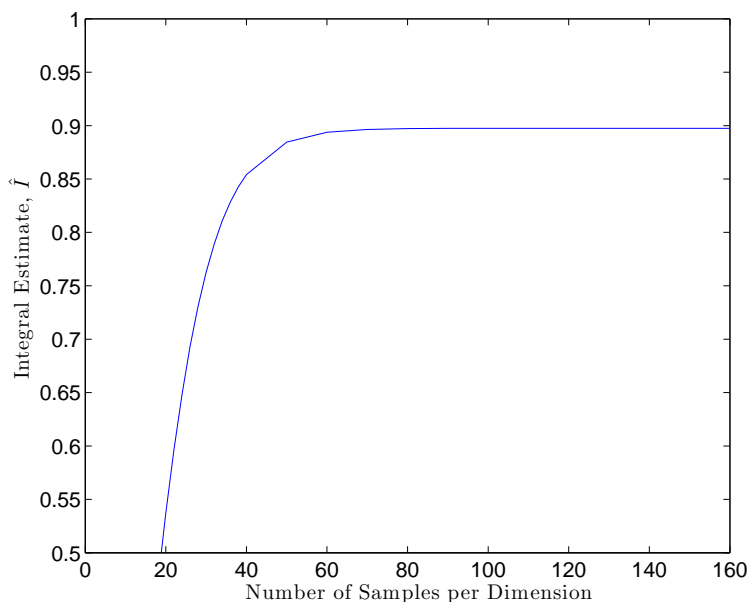


Figure 3.19: Convergence of the peak region ($40^\circ \times 20^\circ$) is achieved much faster with numerical quadrature. After only approximately 80 samples per dimension, the correct result is achieved.

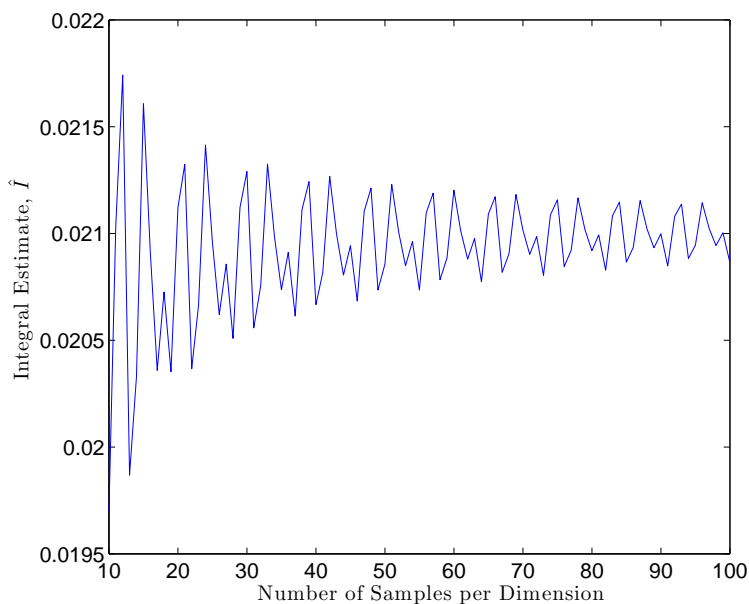


Figure 3.20: Convergence of the outer region is achieved much faster with numerical quadrature. After approximately 50 samples per dimension, the correct result is achieved; note the resolution in the y-axis scale.

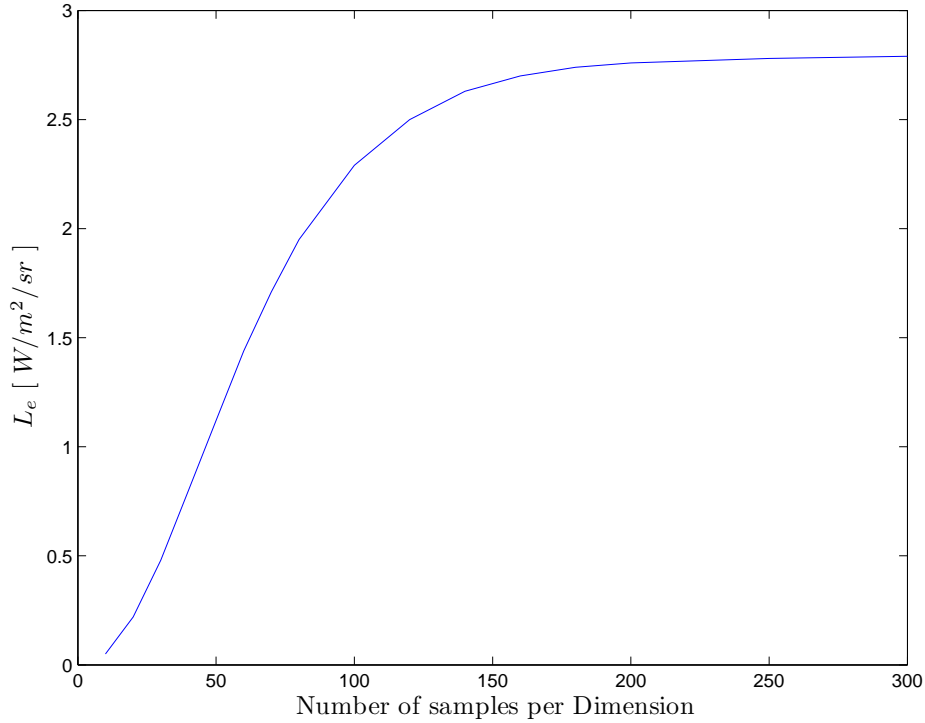


Figure 3.21: Additional to the BRDF, the hemispherical geometry must be sampled to accurately calculate the solid angles that each facet occupies.

sample approximates the radiance in that solid angle. The more samples, the smaller the solid angles become, increasing the accuracy of the estimated radiance.

3.4 Background Construction

In addition to the target's self emission, there is also a significant contribution to the signature from the background, especially when a highly reflective surface treatment is applied. The sources of this background component include terrain reflection and self emission, sun reflection and atmospheric path radiance. For this reason, a detailed background model is required for the simulation to be accurate, even for laboratory simulations.

3.4.1 IR Range. The IR Range at the Sensors Directorate, AFRL, is a temperature and atmosphere controlled enclosure designed to simulate conditions up to

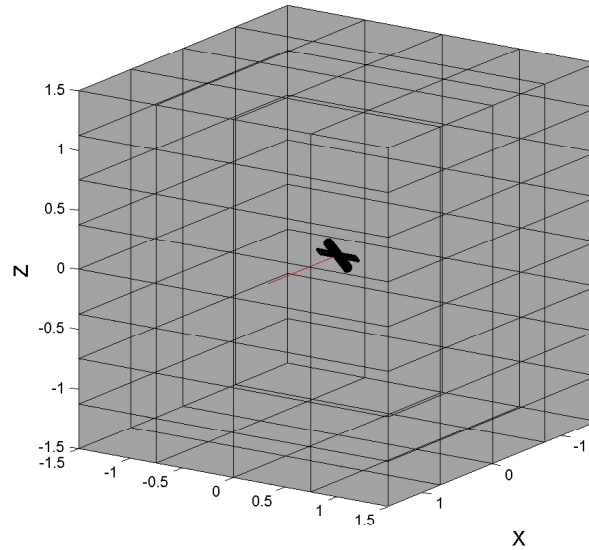


Figure 3.22: AFRL’s IR Range is developed in Blender3D and imported into Matlab[®]. The cylinder model is included in the figure for a size comparison.

35,000 feet in altitude. Each wall is cooled with liquid nitrogen and the upper half can be controlled separately to the lower half; this allows a *sky* and *earth* to be simulated. Cooling with liquid nitrogen provides a temperature controlled environment and also minimizes the thermal emission of the background.

To represent the IR Range background in LCAIR, a cube with sides of length, 3m, is facetised (tesselated) into 160 facets, as shown in Figure 3.22, where the cylinder model is also included for scale comparison. Each facet’s material property is set to diffuse emission and emissivity is set to 96%. From data included in [3], the upper walls of the range are set to 263K and 253K to simulate sky and terrain, respectively.

3.4.2 World Sphere. For a simulation to be accurate, it must be representative of the physical environment. The IR Range background discussed above is a suitable background for laboratory experiments, however, it is not as suitable for a *real world* simulation. The real world contains, earth, sky, sun and atmosphere that

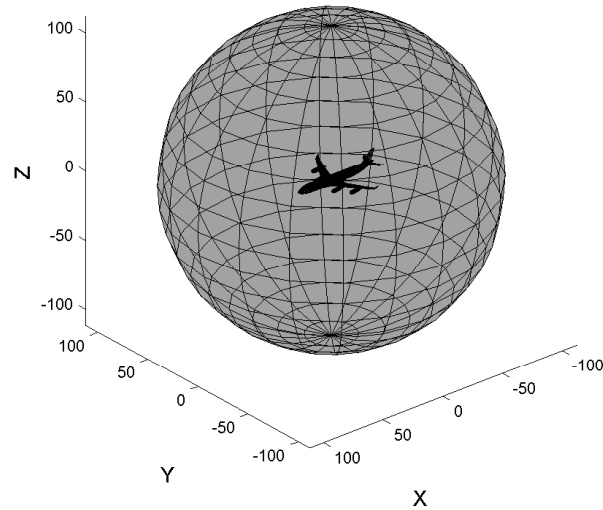


Figure 3.23: The world sphere background model is developed in Blender3D and imported into Matlab[®]. The A340 aircraft is included in the figure to demonstrate the simulation setup.

is contributing to the background irradiance onto the model. The world sphere is designed to simulate sky and terrain when the algorithm does not encounter an aircraft facet. Figure 3.23 shows the world sphere with A340-300 aircraft inside.

For the A340-300 simulations, the ambient weather conditions are set to be standard overcast day, at the Dallas Airport in Texas, with an air temperature of 27°C (300K). An inland airfield was chosen to remove the effects of water, and provide solid ground as the terrain model.

3.4.2.1 Terrain. The terrain is modelled as a blackbody. This decision is based upon spectral radiance figures listed in the The Infrared Handbook [26]. The terrain composition around the airport is assumed to be an even mix of grass and concrete/asphalt covered areas. This assumption is based upon a heavily populated or industrialized area surrounding the airport, which is common of many major international airports.

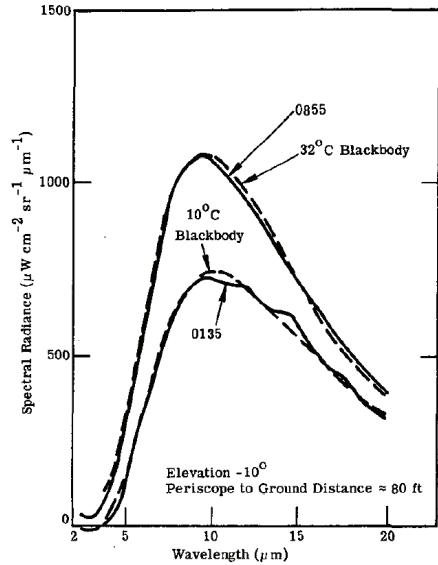
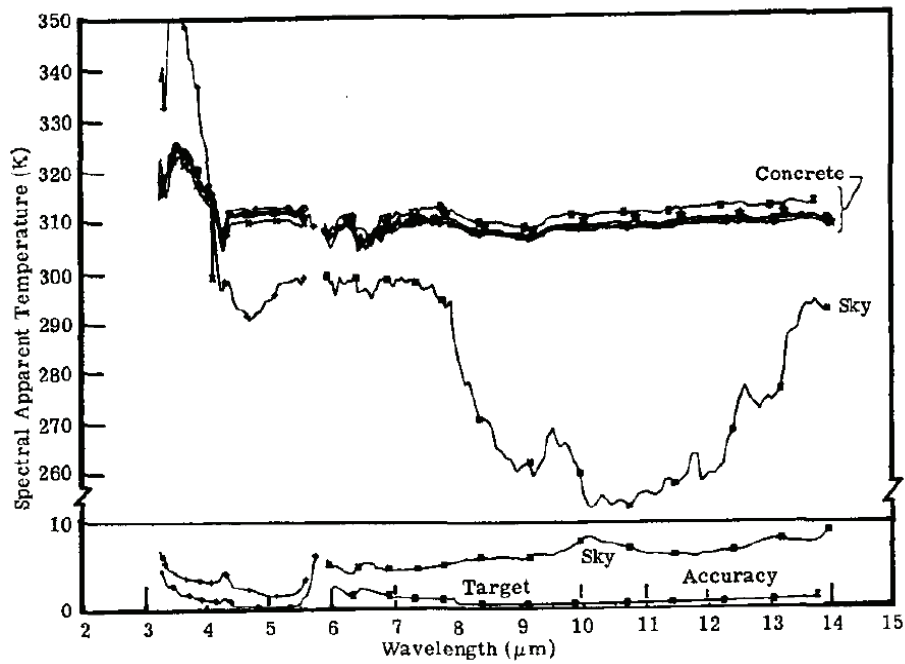


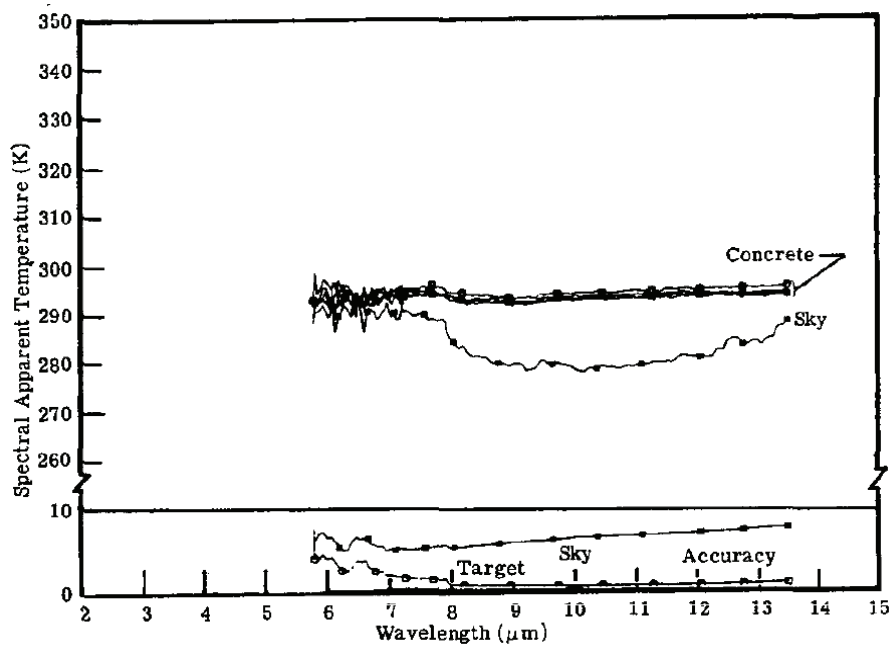
Figure 3.24: Day and night radiances of grass-covered field, reproduced from [26, Figure 3.27]. Note that the measured radiance matches the radiance of a perfect blackbody reasonably well, inferring a spectral emissivity very close to one.

Figure 3.24 is reproduced from [26] and shows the spectral radiance of a grass covered field. The blackbody curves for the ambient temperatures are provided and match reasonably well to the measured radiance; hence, grass will be defined as a perfect blackbody at the ambient temperature.

Concrete and asphalt can also be approximated by a perfect blackbody, however, the apparent temperature is higher than ambient. Figures 3.25 and 3.26 show the spectral apparent temperature with and without cloud cover for concrete and asphalt, respectively. Spectrally, the emission is flat, which usually implies a greybody; however, no emissivity information is given. The spectral peaks between $3 - 4\mu\text{m}$ on both figures, with no cloud cover, are due to scattered solar radiation; however, it is ignored in the greybody assumption, and an averaged brightness (apparent) temperature is calculated. Note the ratio between ambient temperature and apparent temperature changes with and without cloud cover. Concrete is 10 Kelvin higher than ambient temperature with no cloud cover where asphalt is approximately 20 Kelvin higher.

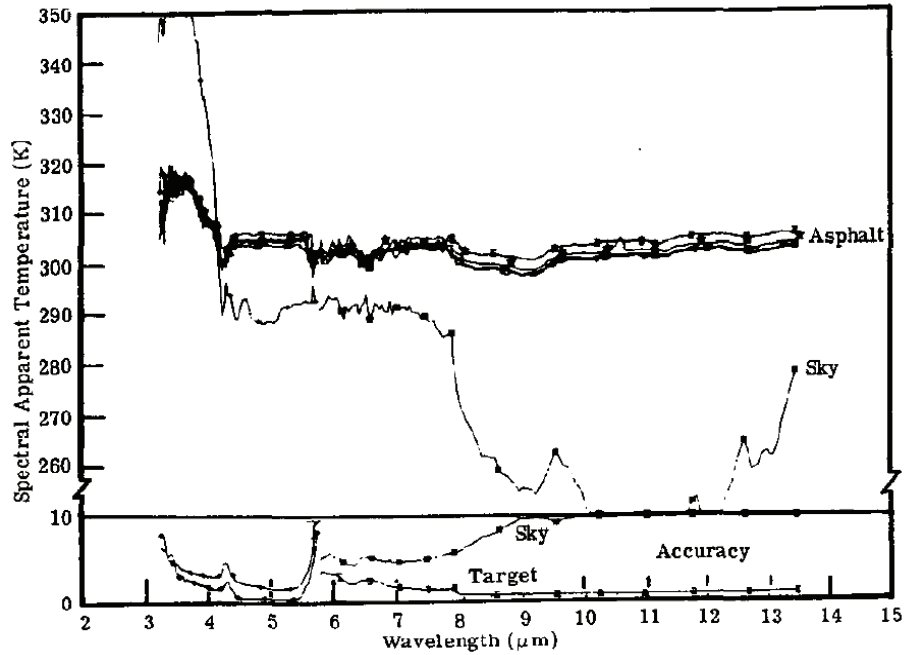


(a)

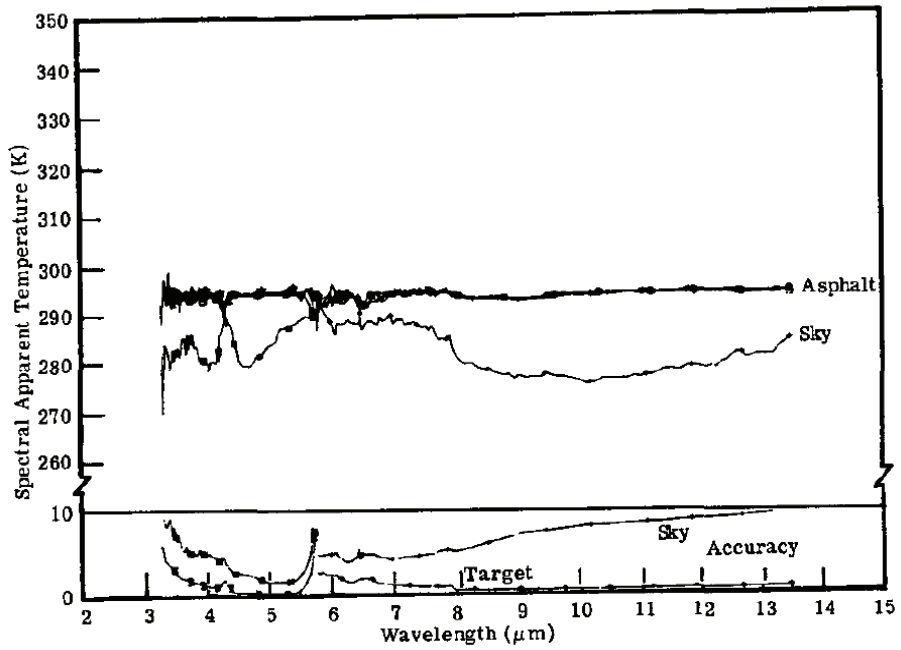


(b)

Figure 3.25: (a) Spectral apparent temperature for concrete with no cloud cover. Ambient temperature is 300K. Reproduced from [26, Figure 3-103(a)]. (b) Spectral apparent temperature for concrete with full cloud cover. Ambient temperature is 295K. Reproduced from [26, Figure 3-103(b)].



(a)



(b)

Figure 3.26: (a) Spectral apparent temperature for asphalt with 3/10 cloud cover. Ambient temperature is 283K. Reproduced from [26, Figure 3-105(a)]. (b) Spectral apparent temperature for asphalt with full cloud cover. Ambient temperature is 285K. Reproduced from [26, Figure 3-105(b)].

Under full cloud, concrete matches the ambient temperature and asphalt is still 10 Kelvin higher.

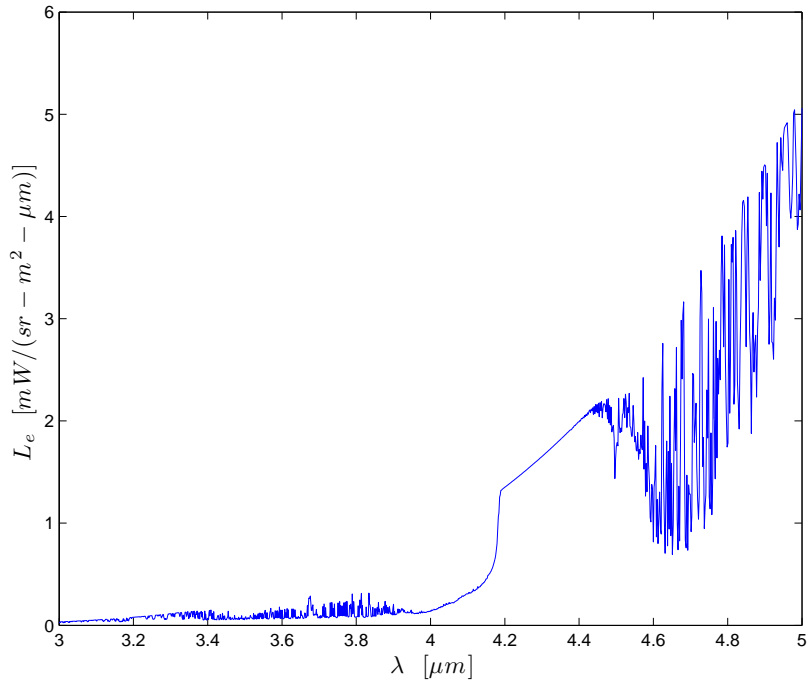
Under the assumption of an even mix between grass, and concrete and asphalt combined, with full sun, the apparent terrain temperature will be 7.5 Kelvin hotter than ambient. Under full cloud, the apparent terrain temperature will be 2.5 Kelvins hotter. The lower hemisphere of the world sphere represents terrain and all facets will be set to 2.5 Kelvin above ambient, 302.5 Kelvin.

3.4.2.2 Sky. The sky is very rarely modelled as a grey- or black-body. Atmospheric transmission and radiance simulations are required to produce the spectral radiance curves.

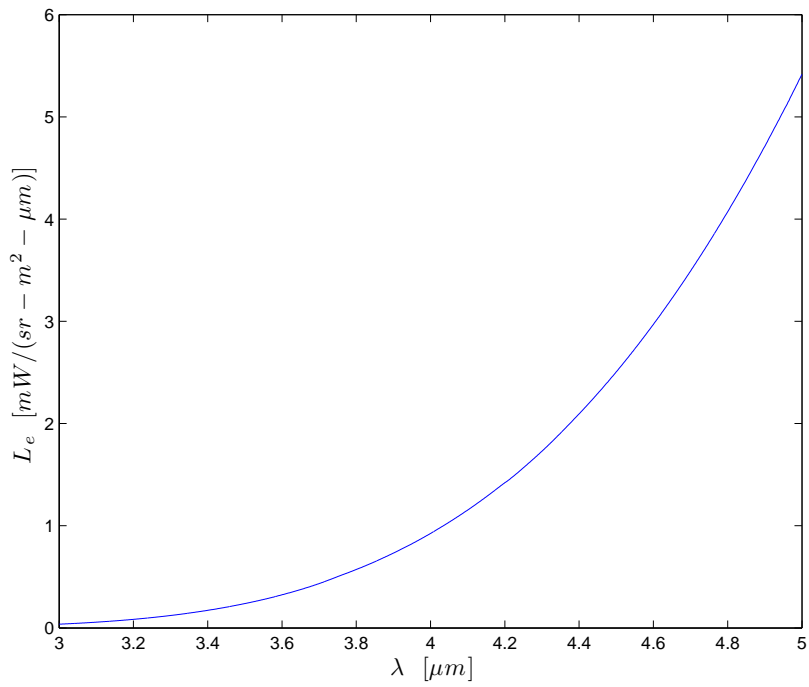
The upper hemisphere of the world sphere represents the sky. The hemisphere is divided in to 10 horizontal rings for elevation dependence, which are divided into 20 facets themselves, to provide azimuth dependence (see Figure 3.23).

The weather conditions that will be used for the simulation are a overcast day with an ambient temperature of 300K. The overcast day is chosen to remove the effect of the sun. Including the sun in the background will influence the intensity of the simulation by making the output a function of sun position. As multiple simulations for different sun and aircraft positions will not be performed, the decision to not include the sun is chosen.

The overcast day provides a cloud cover which absorbs and re-emits radiation. A cloudless sky should be a selective emitter where emission bands correspond to the atmospheric constituents, for example water, H_2O , and carbon dioxide, CO_2 . The denser atmosphere (cloud cover) fills in the background spectral radiance curve, which better approximates a blackbody, as it has more particles to absorb and re-emit radiation. Figure 3.27 shows two spectral background radiance curves produced by MODTRAN, of a typical sunny day and the overcast summer day, that will be used in the simulation for the MWIR band. Figure 3.28 displays the LWIR case.

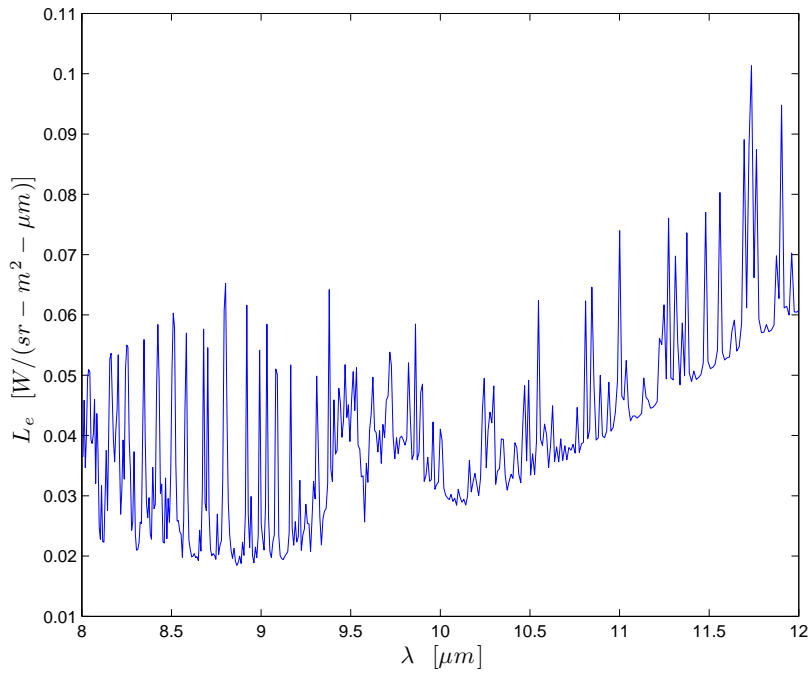


(a)

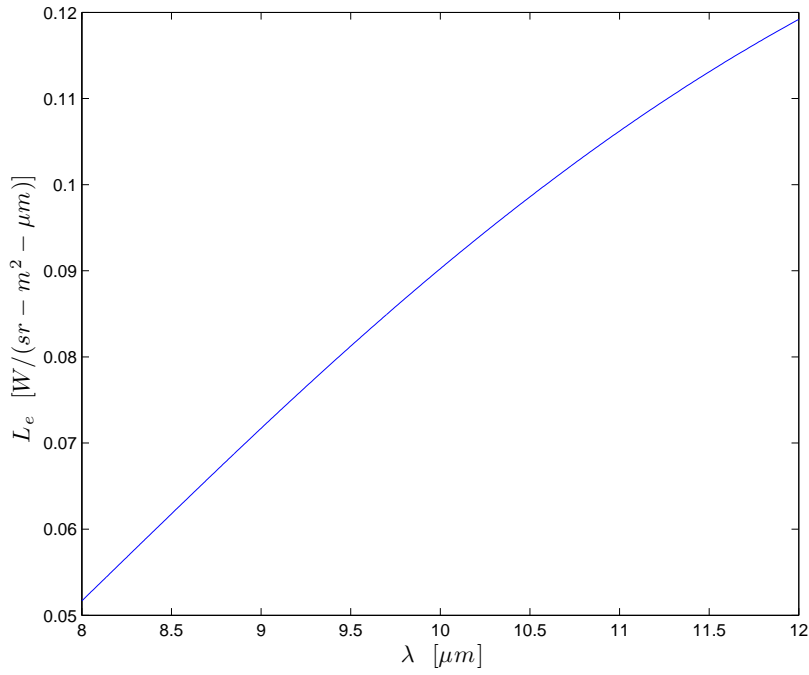


(b)

Figure 3.27: MWIR spectral path radiance to infinity produced by MODTRAN for (a) a sunny day, and (b) a cloudy day. Note how the presence of cloud fills in the curve to approximate a greybody.



(a)



(b)

Figure 3.28: LWIR spectral path radiance to infinity produced by MODTRAN for (a) a sunny day, and (b) a cloudy day. Note how the presence of cloud fills in the curve to approximate a greybody.

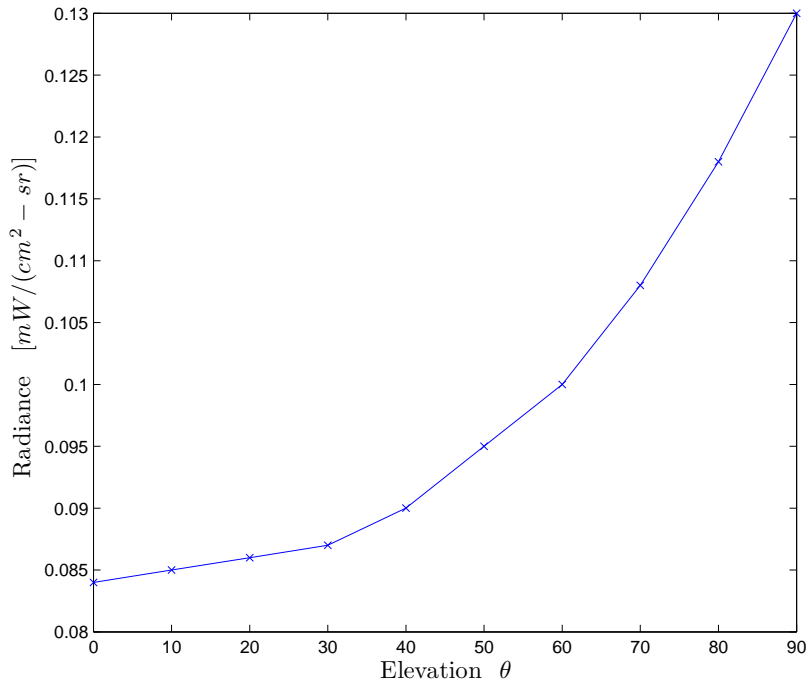
The hemisphere is broken into ten regions in elevation. This allows different background radiance profiles to be simulated as a function of elevation. Figure 3.29 shows the integrated background radiance as a function of elevation from the earth surface normal where 90° is the horizon. Note how the integrated path radiance is a function of elevation angle and increases as the path moves closer to the horizon. This is because the path becomes more optically dense as more atmosphere at low altitudes is included in the simulation. When observing at zero elevation (zenith), the optical density of the path is the least, thus, the path radiance curve is not filled in as much and the integrated band radiance is lower.

3.5 Emission and Propagation Algorithms

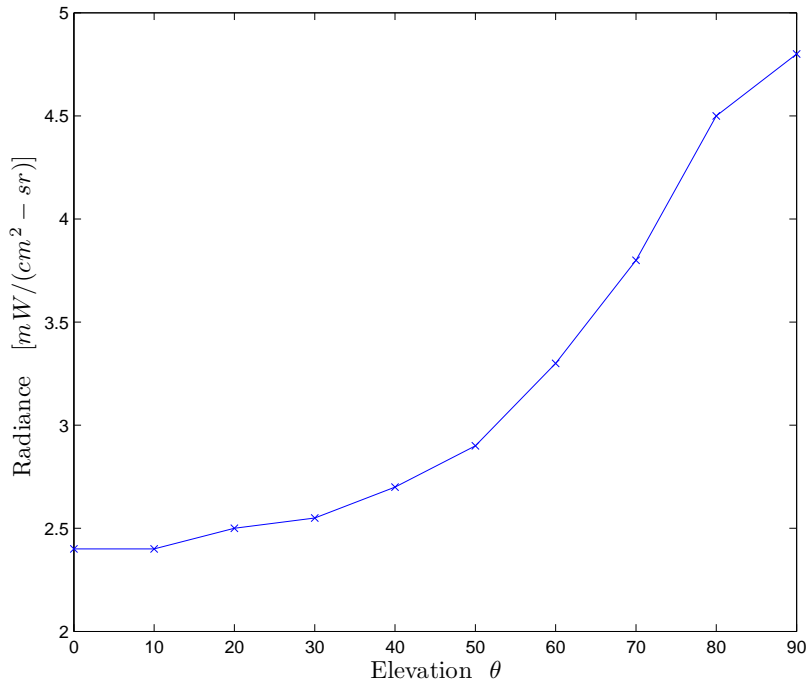
During a simulation, the incident and reflected radiance of a facet must be calculated. A tessellated aircraft model allows the algorithm to be facet-based rather than pixel-based as computer graphics algorithms are. Additionally, a pixel-based algorithm (which could be used to simulate an imaging optical system) has the limitation of not sampling with prior knowledge of the aircraft's geometry. It is this lack of *a priori* information that increases the computation time of *blind* deterministic algorithms and drives the need for modified algorithms for a more resource friendly solution.

A detector (whether a camera or missile seeker-head) that is orientated in the direction of the aircraft will integrate the visible facets from any point of view (POV) into a single electrical output for each element in the detector.

As discussed in Chapter II, the emitted radiation from a surface is either self-emitted or reflected. The algorithm must calculate the emitted and reflected energy (in radiance or intensity, whichever is the more convenient unit for further use) from each facet. To express this mathematically in radiance units, Equation (3.4) lists the observed radiance $L_{e(\text{Observed})}$ as a sum of the self-emitted radiance and reflected



(a)



(b)

Figure 3.29: Integrated path radiance to infinity produced by MODTRAN for (a) MWIR and (b) LWIR bands. The absolute magnitude of the values is not important, simply note the power of the background path radiance dependence upon elevation.

radiance.

$$Le_{(\text{Observed})} = Le_{(\text{Self-Emitted})} + Le_{(\text{Reflected})} \left[\frac{W}{sr - m^2} \right] \quad (3.4)$$

Calculation of the self emitted radiance is trivial. The radiant thermal emission of Chapter II (at some surface temperature, T [K]) is scaled by the specific material emissivity from Equation (2.4), where the reflection coefficient, $\rho(\theta)$, is taken from the material DHR measurements.

$$Le_{(\text{Self - Emitted})} = \varepsilon(\theta) \cdot \int_{\lambda_1}^{\lambda_2} Le_{(\text{BB})}(T_{\text{surface}})d\lambda \left[\frac{W}{sr - m^2} \right] \quad (3.5)$$

Conversely, calculating the reflected radiance is considerably more complex and the following subsections deal with various methods of achieving an approximation of the analytical solution. The accuracy of the approximation is driven chiefly by the sampling resolution of the model and functions in the simulation.

Analytically, the reflected radiance from a point, x , in the direction of the observer, is the hemispherical integration of the irradiance at a point, x , and the hemispherical BRDF. This method is expressed mathematically in Equation (3.6), and Figure 3.30 also shows this graphically.

$$Le_{\text{Reflected}} = \int_{\Omega} Le_{B_i(\text{Emitted})} f_r(\theta_i, \theta_r, \Delta\phi) d\omega_i \left[\frac{W}{sr - m^2} \right] \quad (3.6)$$

By combining Equations (3.5) and (3.6), an accurate definition of emitted radiance results,

$$Le_{A(\text{Observed})} = \varepsilon(\theta) \cdot \int_{\lambda_1}^{\lambda_2} Le_{A(\text{Blackbody})}(T_{\text{surface}})d\lambda + \dots \int_{\Omega} Le_{B_i(\text{Emitted})} f_r(\theta_i, \theta_r, \Delta\phi) d\omega_i \left[\frac{W}{sr - m^2} \right]. \quad (3.7)$$

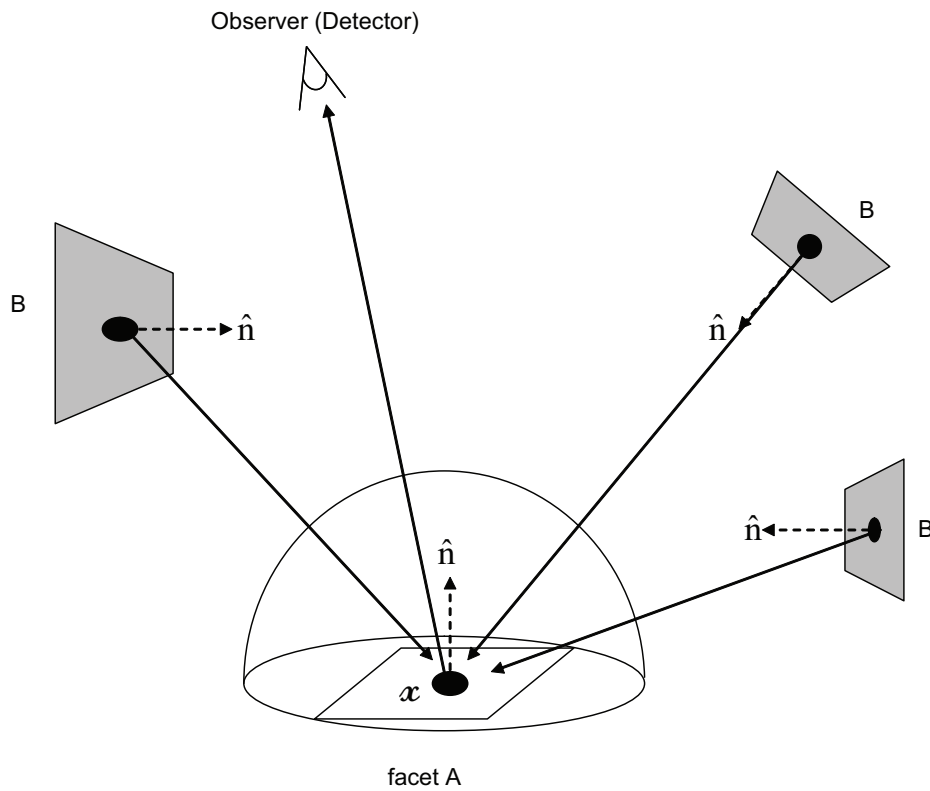


Figure 3.30: An illustration of the process of hemispherically integrating the irradiance on facet A, to calculate the reflected radiance in the direction of the observer, from a point, x .

3.5.1 Specular Reflection Assumption. The simplest way of evaluating the reflected radiance integral, Equation (3.6), is that of a purely the specular surface, which was the major assumption in Bortle’s and Martinez’s work, [3] and [17]. This assumption is valid when a highly specular surface is used; however, when a more diffuse surface is used, the assumption breaks down and gives inaccurate results. Under the specular assumption, the integral is not required to be evaluated as the BRDF is only non-zero when the incident and reflected elevation angles are equal and the azimuthal angles differ by 180 degrees. The reflected radiance then becomes the incident radiance multiplied by the reflectivity, $\rho(\theta)$.

$$Le_{\text{Reflected}} = Le_{\text{Incident}} \cdot \rho(\theta) \left[\frac{W}{sr - m^2} \right] \quad (3.8)$$

This method is very fast to compute as only a single incident radiance value is required.

3.5.2 Radiosity. The first algorithm implemented to attempt to hemispherically integrate the irradiance contribution was classical radiosity as described in [10]. Radiosity is an algorithm that calculates in the direction of flux propagation with the intent of calculating the exitant radiance distribution of each facet. When the process has finished, a value of observed radiance from any direction can simply be read from the data file. This method would make trend analysis very easy, simply by rotating around the model in azimuth and reading off radiance values from each facet.

The algorithm starts with the first facet’s self emission, where the isotropic radiance distribution is calculated from Equation (3.5), as a function of $\rho(\theta)$. The facet’s hemisphere must then be sampled to reveal the surrounding geometry (whether it is another aircraft facet or background). This method divides the hemisphere up into a 2D (ϕ and θ) grid where the exitant radiance is assumed to be constant through the sampled solid angle. The number of divisions is up to the user, however, larger numbers will take longer to calculate, yet, will yield a more accurate solution. This sampling method, more commonly known as ray tracing, is described in detail in Appendix C.

For solid angles where background is visible (a possible location of the observer), the emitted radiation is stored in that facet’s observed radiance map for later recall when rendering the scene. For the other solid angles where model facets are visible, the flux to each facet is summed and the algorithm moves to the next step for each visible facet. Incident flux on a facet can be easily converted to irradiance by dividing by the facets area. From there, the BRDF is scaled by this irradiance which becomes the exitant radiance from that facet. The process of sampling the hemispherical geometry continues as before and the algorithm quickly becomes nested.

The algorithm stops when the self-emitted radiance from the first facet exits the model and reaches the background where it is stored in the observed radiance map. For complex models, this process may take considerable time; thus, stopping conditions should be developed to truncate the random walk of the algorithm through the facet’s geometry. Once the algorithm has finished propagating the first facet’s self emission, it moves to the second facet and restarts. Stopping conditions for the algorithm can include truncating the random walk after a certain number of bounces, or ignoring small incident flux values that when reflected into the facet’s hemisphere will not meaningfully contribute to the observed radiance. Figure 3.31 is a flow chart that outlines the process in graphical form, and Equation (3.9) describes the process mathematically. For greater detail on the algorithm, including techniques to increase accuracy, see [10] and [5, Chapter 6].

$$M_{e_i} = \frac{1}{A_i} \int_{S_i} \int_{\Omega_x} L_{e \text{ Incident}} \cos(\theta_x) d\omega dA_x \quad \left[\frac{W}{m^2} \right] \quad (3.9)$$

Radiosity algorithms are historically slow, as path lengths carrying significant flux can become long. Also, they are suited well to diffuse reflections where the sampling rate can be kept low. However, when more specular BRDFs are used, the sampling issue described in Section 3.3.2 becomes important. When the incident irradiance is multiplied by the BRDF, the BRDF must be adequately described (sampled). This method was used early on during the simulations included in Appendix A and provided

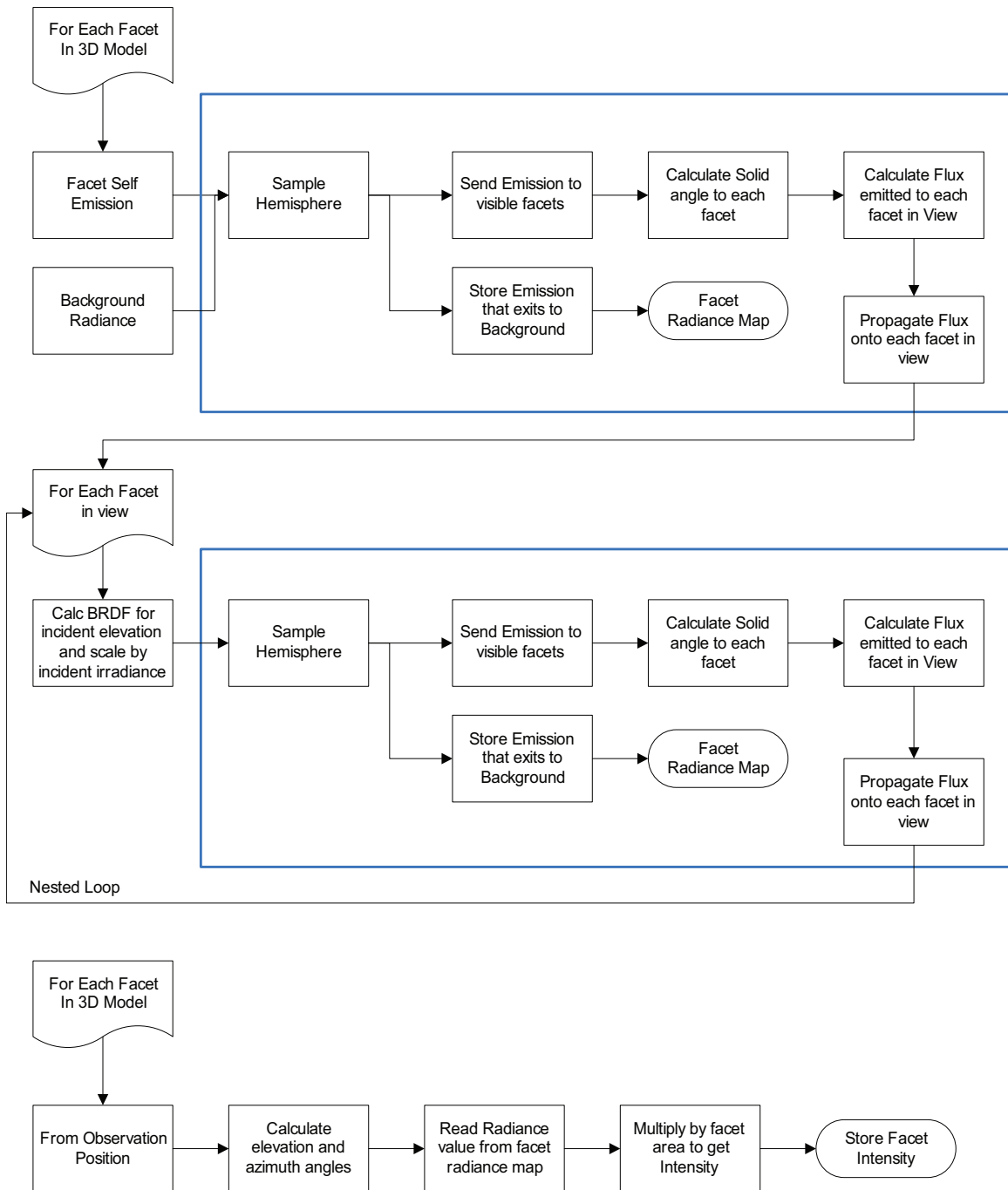


Figure 3.31: The steps involved in the Radiosity algorithm are listed above. The number of bounces becomes important, as they are calculated independent of the observation direction. Even if only one observation is required, the algorithm must be completed in full.

accurate solutions. However, when a realistic, specular BRDF was introduced, the sampling rate had to be increased dramatically. This increase made computation times very long, even for the cylinder model. For this reason, radiosity was not chosen as an algorithm capable of simulating IR signatures with highly specular BRDFs.

3.5.3 Point-Of-View Hemispherical Integration. The classical radiosity algorithm of [10] has an easy-to-calculate-and-program algorithm. Because of this property, an attempt was made to reverse this algorithm starting from the observer, in the hope of reducing the number of paths and computation time.

This algorithm starts with the first visible facet from the observer's POV. From there, Equation (3.6) is approximated by evenly sampling the hemisphere, identically to the radiosity case, and calculating incident radiance on the facet. To include multiple bounces, by calculating the reflected radiance of Equation (3.6) again, the algorithm steps into the visible facets. This method attempts to integrate the BRDF and incident radiance using the method described in Section 3.3 where there is no *a priori* knowledge of the reflectance distribution. The same issues of computation time are experienced, and this blind integration method is rejected as a suitable propagation algorithm.

3.5.4 Point-Of-View Monte Carlo Hemispherical Integration. Similarly to the narrative in Section 3.3, Monte Carlo hemispherical integration was evaluated as an algorithm. However, as the BRDF could not be integrated efficiently with a normal or uniform distribution, this method is not followed. If the geometry of the simulation created many paths, for example, a complex cavity like an engine exhaust system, then this method may prove more efficient than numerical quadrature as the number of dimensions and bounces becomes large.

3.5.5 Point-Of-View Stratified Hemispherical Integration. Section 3.3.3 showed that the most efficient method of integrating the BRDF, one of the terms in Equation (3.6), is to use stratified numerical quadrature in two regions; the spec-

ular peak and outer diffuse floor. As this method is the most efficient in integrating the BRDF, it follows that it will be the most efficient in calculating Equation (3.6). Hence, the best propagation algorithm will be POV stratified hemispherical integration. Figure 3.32 is a flow chart outlining the propagation algorithm.

This algorithm is again facet-based, and starts at the first facet in the model. The self-emitted radiance is easily calculated using Equation (3.5) and the reflected radiance is calculated using the algorithm in Figure 3.32 to approximate the integral in Equation (3.6). Although this method is POV-based and has to be recalculated for each observing location, an answer is achieved much faster than in the classical radiosity case.

The length of possible paths that the algorithm can calculate when integrating the BRDF over the whole hemisphere is infinite. The infinite length paths are created by recurring bounces between two mutually visible facets. The diffuse reflection calculations, for a highly specular surface, quickly become negligible, even after the first bounce.

Two approximations can be made to reduce the number of paths. The first is to reduce the angular search space of each bounce. From Equation (3.6), the irradiance from the whole hemisphere must be integrated to produce the reflected radiance. However, if the surface is highly specular, then the angular region of integration, Ω , can be reduced and still calculate an accurate result. This was hinted at in Section 3.3.3, however, the outer region integral was maintained. Figures 3.19 and 3.20 show the integral values over the peak (0.917) and outer (0.02) regions, respectively. The large value for the peak integral compared to the outer result proves that the surface (bare aluminum in this case) is highly specular. Under the assumption that the model has a highly specular surface treatment, then the solid angle can be reduced to only the peak region of the BRDF, with a negligible effect on accuracy.

The second approximation is to stop the path when a surface of very high emissivity is encountered. In this case, the self-emitted term of Equation (3.4) dominates,

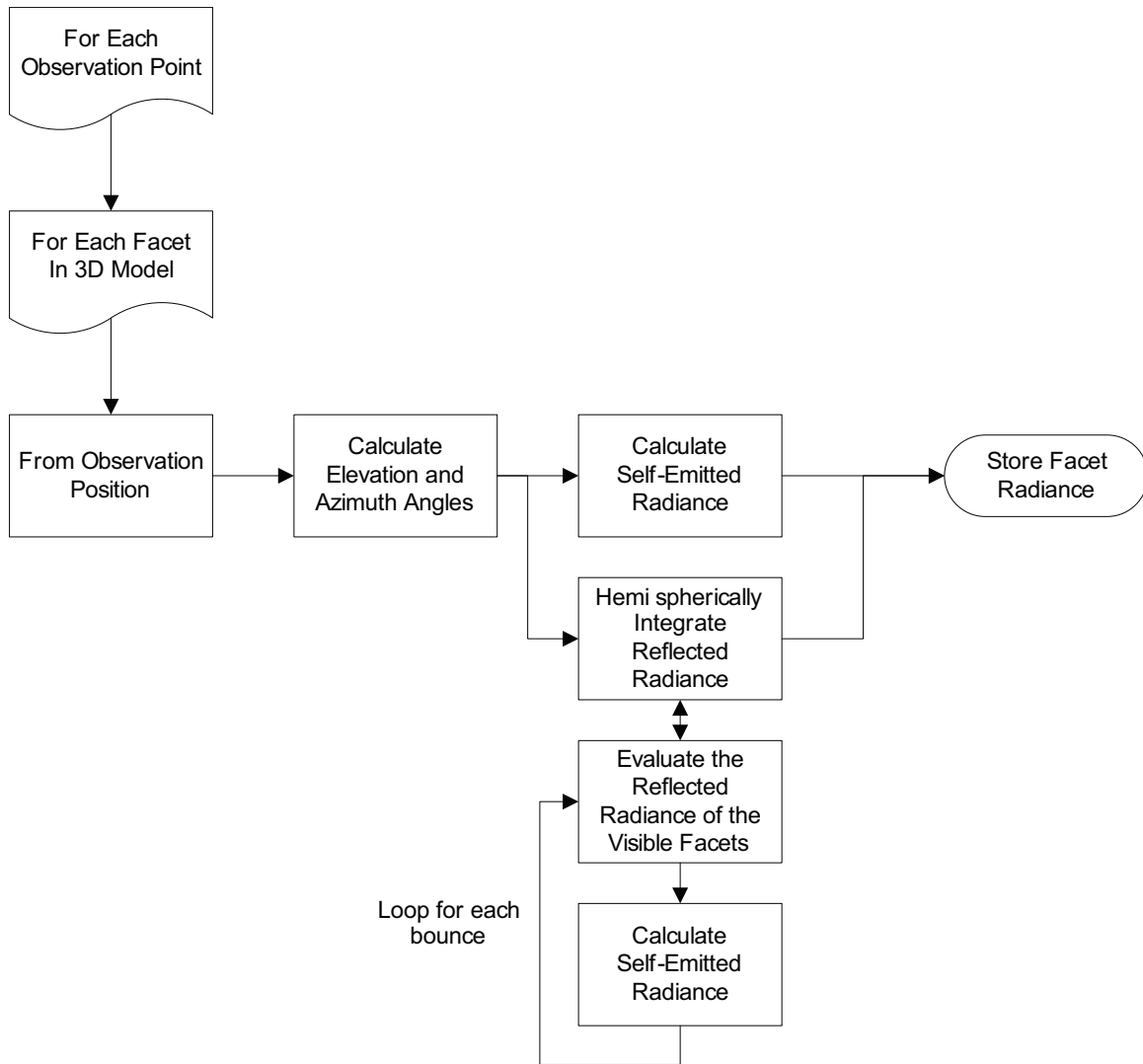


Figure 3.32: The process flow for the hemispherical numerical quadrature integration algorithm is less complex than the radiosity one. This algorithm also allows a solution to be quickly obtained where only the radiance in one direction is calculated for each simulation.

rather than the reflected term; when this is the case, there is not much gained from calculating further paths as the result will be scaled by the very small reflectance. This method is not employed in the algorithms, however, in the IR range, the walls are highly emissive (96%) and as the algorithm does not calculate a bounce off the background facets, by proxy, this method was implemented, although, it was not for the highly emissive model facets.

3.5.6 Memory Considerations. With all of these algorithms, memory allocation cannot be ignored. The radiosity algorithm is the most memory intensive as it stores the emitted radiance maps for each facet. A single map contains a value for each combination of θ and ϕ . The cylinder model has around 2000 facets, and typical hemispherical resolutions were 200 in each dimension. This requires $2000 \times 200 \times 200 \times 8$ bytes (625Mb) of data. To have this much memory reserved for one variable, the computer must have enough memory for `Matlab`[®] and the operating system to still function, without using swap space on the hard drive. If swap space is used, then all the techniques listed here to save processing time will be wasted.

3.6 Artificial Cavity Blackbody Source Simulation

When calibrating laboratory systems, a perfect blackbody source is usually required. However, no material by itself exhibits the properties of a perfect blackbody as there is always a reflected component as the emissivity is never exactly one. Flat black paint is very close, yet it is still not accurate enough to be used as a calibration source.

A useful thermodynamics property is that radiation inside an isothermal, enclosed cavity matches that of a perfect blackbody. The radiation emitted inside the cavity will bounce around, being absorbed and re-emitted, until the radiation inside the cavity is spectrally that of a perfect blackbody source at that same temperature, even when very low emissivity internal surfaces are used. To use this radiation as a source, a small hole must be made to allow the radiation to escape. This hole is then

Table 3.3: Variable Definitions for the Method of Gouffé.

Variable	Definition
ε_0	Total emissivity of cavity source
ε'_0	Emissivity of cavity
ε	Emissivity of internal cavity walls
s	Area of aperture
S	Surface area of cavity including aperture
S_0	Surface area of a sphere of the same depth as the cavity
l	Depth of cavity
r	Radius of aperture

emitting perfect blackbody radiation. The radiation becomes less representative of a perfect blackbody as the hole becomes larger. There are many theories that predict this behavior, however, the Method of Gouffé is provided in [11].

Gouffé predicts the total emissivity, ε_0 , from a cavity source as a function of internal emissivity, ε , cavity depth, l , hole radius, r , area of cavity aperture, s , internal surface area of the cavity, S , and the surface area of a perfect sphere with the same diameter as the cavity, S_0 . The method is detailed in Equations (3.10) through (3.12), and the variables are described in Table 3.3.

$$\varepsilon_0 = \varepsilon'_0 (1 + k) \quad (3.10)$$

$$k = (1 - \varepsilon) \left[\frac{s}{S} - \frac{s}{S_0} \right] \quad (3.11)$$

$$\varepsilon'_0 = \frac{\varepsilon}{\varepsilon \left[1 - \frac{s}{S} \right] + \left(\frac{s}{S} \right)} \quad (3.12)$$

Equation (3.12) is plotted as a function of s/S for varying internal emissivities, ε , in Figure 3.33, which is reproduced from [26, Figure 2-1]. The ratio of l/r is

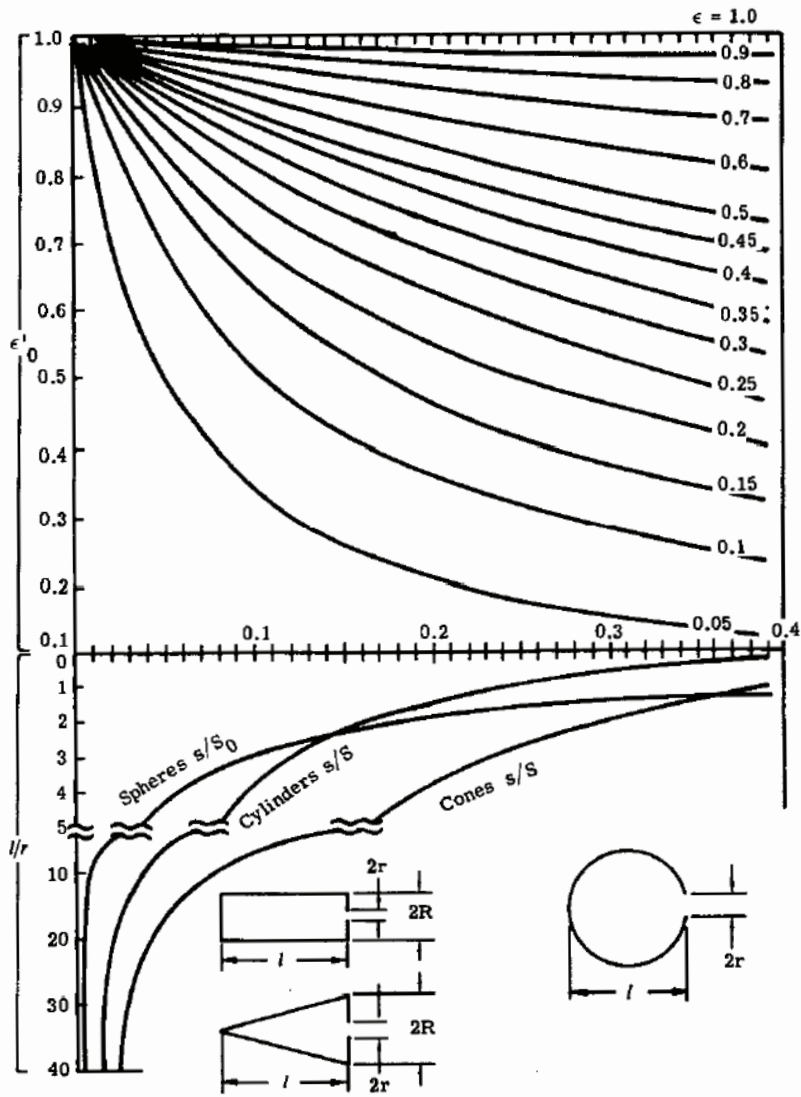


Figure 3.33: The emissivity of the blackbody cavity is calculated, using Equation (3.12), as a function of the s/S ratio of the cavity for many different internal greybody emissivities, ϵ . The lower half of the figure calculates the s/S ratio as a function of l/r for spherical, conical and cylindrical cavity shapes. Reproduced from [26, Figure 2-1].

converted to the s/S ratio, transferred up to the greybody emissivity of the cavity and across to the cavity emissivity. This value is then modified to account for cavity shape by k in Equation (3.10). The different aperture sizes create different s/S ratios, and thus, eight data points on each curve.

The curves of Figure 3.33 will be reproduced by the model in Figure 4.1.

3.7 *A340-300 Simulation Output*

The output of the simulation is a spectral intensity curve in the direction of the observer, for the spectral band of interest. The simulation calculates the intensity at the target. Thus, to calculate the apparent intensity at the detector, a spectral transmission curve must be applied. To gain a total in-band scalar intensity value, the spectral intensity can simply be integrated across the waveband.

To calculate the intensity in the direction of the observer, the simulation must convert the emitted and reflected radiance from each facet to intensity by summing the radiances and multiplying by the projected facet area. This process is expressed in Equation (3.13) where N is the number of facets in the model, $A_i \cos(\theta_i)$ is the projected area of the facet, and V_i is the visibility function. The visibility function is a binary function: 1 if the facet is visible from the view point, and 0 if not. The simulation must calculate which facets are visible from the POV and apply a mask, $V(i)$, to the intensity values calculated previously.

$$I_{e \text{ Target}} = \sum_{i=1}^N (Le_{\text{Self-Emitted}} + Le_{\text{Reflected}}) \cdot A_i \cdot \cos(\theta_i) \cdot V_i \left[\frac{W}{sr} \right] \quad (3.13)$$

3.8 *Exercising the Model*

A scenario typical of an aircraft landing at an international airport will be simulated to calculate the apparent irradiance at the detector. Then, a maximum value for noise equivalent irradiance (NEI) will be chosen to allow a system to track and *lock-on* to the aircraft. A lock-on event is defined as when the apparent irradiance

from the target achieves an SNR of 10, or ten times the NEI of the detector system. An expression for the maximum allowable NEI, and yet still lock onto the aircraft, is developed in Equation (3.14). An SNR of 10 was chosen to give the detector a signature large enough to ensure the system can detect and track the aircraft.

$$NEI_{\text{Max}} = \frac{E_{\text{Signal}}}{SNR_{\text{Lock-on}}} \left[\frac{W}{m^2} \right] \quad (3.14)$$

The NEI is a parameter that describes the noise power of the entire electro-optical system of the detector. This allows comparison between platforms independent of detector type, tracking methods and noise sources. The NEI is a noise power parameter which translates the internal noise sources (e.g., Johnson, shot and generation-recombination noise) as an equivalent irradiance at the optic.

3.8.1 Contrast Detection. The signal detected by the detector is the sum of the target and background irradiance at the optic plane of the detector. The background exists constantly and the target must provide contrast against the background for detection. The simulation assumes a single-pixel detector where the whole FOV is integrated into one signal.

Figure 3.34 shows the irradiance with and without the target present. The first irradiance signal level, $E_{e \text{ NoTarget}}$, is the background without a target present.

$$E_{e \text{ NoTarget}} = L_{e\text{Background}} \Omega_{FOV}. \quad (3.15)$$

This background irradiance is calculated with MODTRAN as was shown in Figures 3.27 and 3.28. The integrated background radiance across the band then becomes the magnitude of the signal. The ripples on the signal depict the electronic noise that is present in all systems, such as Johnson or shot noise. The NEI represents the power contained in this electronic noise. Thus, for the target to be detectable, it must have a signal that is greater than the random noise. The signals in Figure 3.34 are expressed as irradiance. Irradiance is calculated by Equation (3.16) where the

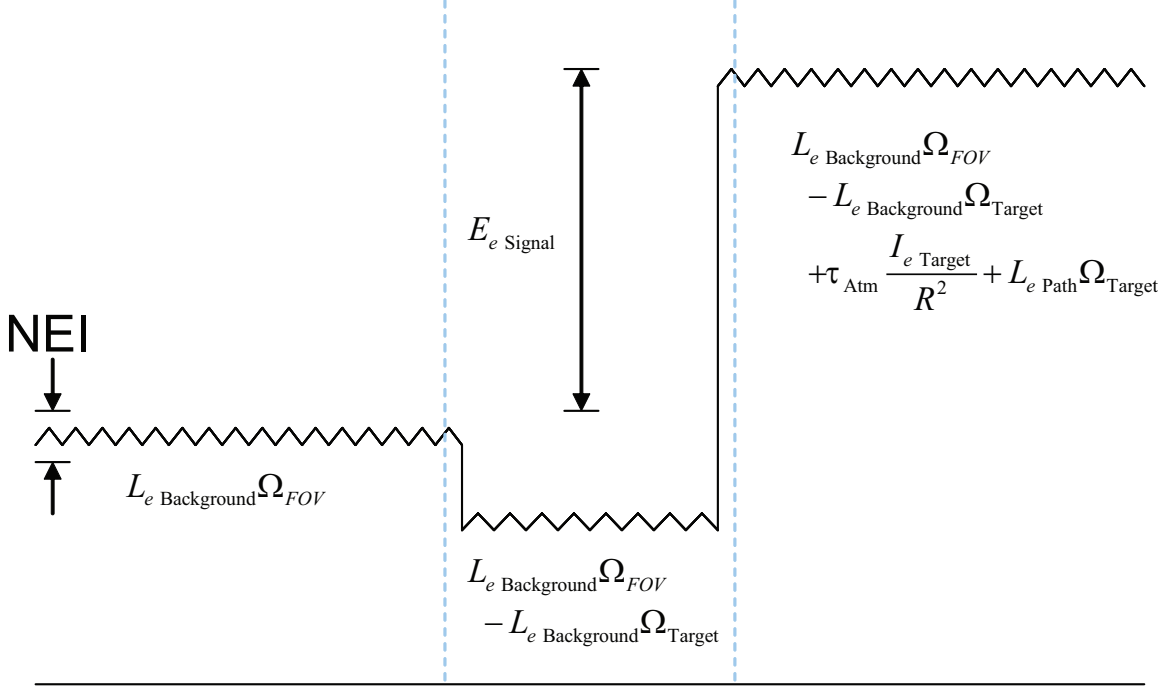


Figure 3.34: The irradiance signal at the detector's optic is a combination of background and target emissions.

radiance of the source is multiplied by the projected area of the source and divided by the range squared, which is also equal to the radiance multiplied by the solid angle that the source occupies.

$$E_e = \frac{L_e A_s \cos(\theta_s)}{R^2} = L_e \Omega_{FOV} = \frac{I_e}{R^2} \quad (3.16)$$

When the target is present in the FOV, the background irradiance is still present, however, the target is now blocking some solid angle of background and must be subtracted before the addition of the signal from the target. To calculate the propagated spectrum, the signal from the target must be multiplied by the spectral transmission discussed in Section 2.4. Additionally, the path radiance from the target to the detector must be added to the signal. This path radiance replaces the subtracted background radiance over the solid angle of the target. The solid angle of the target is calculated by,

$$\Omega_{Target} = \frac{A_{Target}}{R^2}. \quad (3.17)$$

Combining these terms gives the irradiance with the target present,

$$E_e \text{ Observed-Target} = L_{e\text{Background}}\Omega_{FOV} - L_{e\text{Background}}\Omega_{\text{Target}} + L_{e\text{Path}}\Omega_{\text{Target}} + \tau_{\text{Atm}} \frac{I_{e\text{Target}}}{R^2} . \quad (3.18)$$

As introduced above, the detection process operates on contrast. A threshold is set above the background irradiance level and when a target is present in the FOV, the signal from the target must lift the observed signal over the threshold. A threshold of ten times the noise level is chosen to guarantee not only detection but enough signal power for tracking algorithms to function correctly. This SNR of 10 is arbitrary, where the actual required value depends upon the sophistication of detection and tracking.

Because the detection process is only concerned with the difference, the background signal can be normalized out and the detection signal as shown in Figure 3.34 is the difference of the irradiance with and without the target,

$$E_e \text{ Signal} = \tau_{\text{Atm}} \frac{I_{e\text{Target}}}{R^2} + L_{e\text{Path}}\Omega_{\text{Target}} - L_{e\text{Background}}\Omega_{\text{Target}} . \quad (3.19)$$

3.8.2 Flight Path. A standard Instrument Landing System (ILS) approach path is simulated. ILS approaches are directed by a radio frequency (RF) system where the aircraft navigates down a virtual 3° glideslope, starting about four nautical miles (7km) out from the runway. The aircraft will also be given an angle of attack of +10°, which is approximately representative of the attitude of an aircraft on final approach.

3.8.3 Aircraft Engagement Positions. Three positions are chosen to simulate the engagement of a MANPADS system against the aircraft. The first position is 1km from the threshold at an altitude of 50m, the second is at 2km out at 100m altitude, and the third is 3km out and 150m in altitude. The detector/observer is located 2km

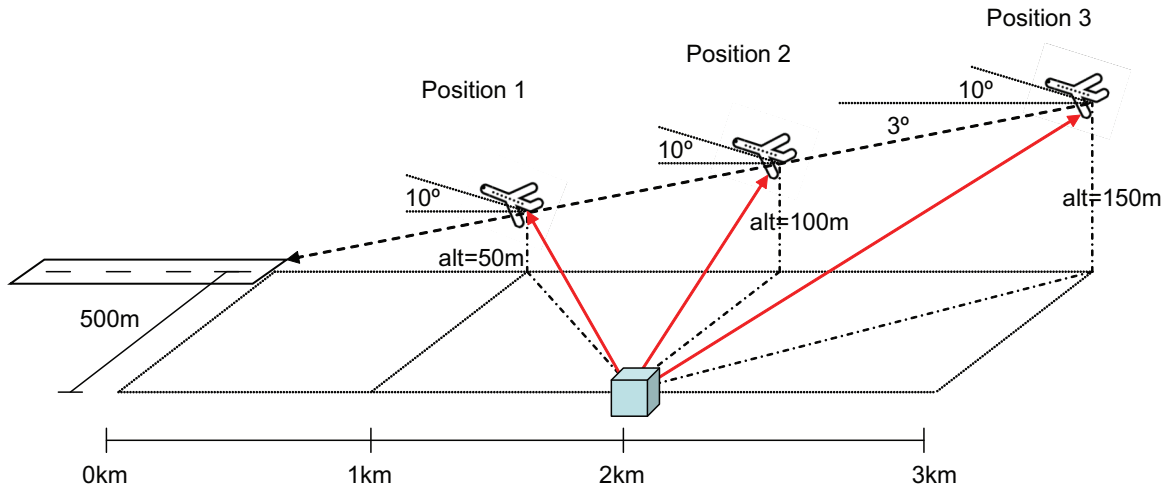


Figure 3.35: Three engagement positions are chosen to calculate the infrared signature irradiance at the detector.

from the threshold and 500m off the centerline of the runway. These positions are illustrated in Figure 3.35.

The positions were chosen as examples only and are not meant to represent a complete parametric study of each of the variables. They are merely a demonstration of the application of an IR signature simulation code.

3.9 Chapter Summary

This Chapter has applied the theory introduced in Chapter II to the methods, models and algorithms that will be used in the IR signature simulations. The results of these simulations are detailed and discussed in Chapter IV.

IV. Results and Analysis

This chapter details the results of the different simulations performed using the algorithms developed in Chapter III. The aim of this thesis is to demonstrate the effect of the BRDF and multiple bounce calculations in IR signature simulations. Several different simulations are performed to aid in the demonstration of the objectives. Initially, simple geometric cases (where analytical results can be obtained) were simulated to ensure the software was coded correctly, and that the propagation algorithm is a valid approximation to the reflected radiance integral of Equation (3.6). The results of these simple simulations can be found in Appendix A, where the radios-ity algorithm performed quite well on diffuse surfaces. However, it failed to calculate the correct results for specular surfaces in a timely manner.

4.1 *Artificial Cavity Blackbody Source Simulations*

A more complex simulation than the simple analytical proofs was performed to check the multiple bounce algorithm, and also as a quantitative check of the radio-metric calculations in the algorithm.

This property is simulated to test the accuracy of the algorithm, using several facetised spherical cavities with varying aperture sizes. Calculations of s/S ratios for the other aperture sizes, and a sample simulated emissivity calculation are included in Appendix B. Figure 4.1 attempts to simulate Figure 3.33 for the $\varepsilon = 0.5$ case. Note the effect of the number of bounces in the simulation. After only one bounce, the cavity emissivity is approximately 75% of the theoretical result. The simulated emissivity of the cavity increases after each further bounce. After four bounces, the simulation is 96% accurate; the ability of the propagation algorithm to accurately predict the analytical emissivity is shown. Further bounces were not calculated due to processing time, and also because the algorithm was predicting the cavity emissivity correctly. As the reflectance distribution of the cavity is diffuse, the whole hemisphere contributes equally with respect to the BRDF, thus, the whole hemisphere of each

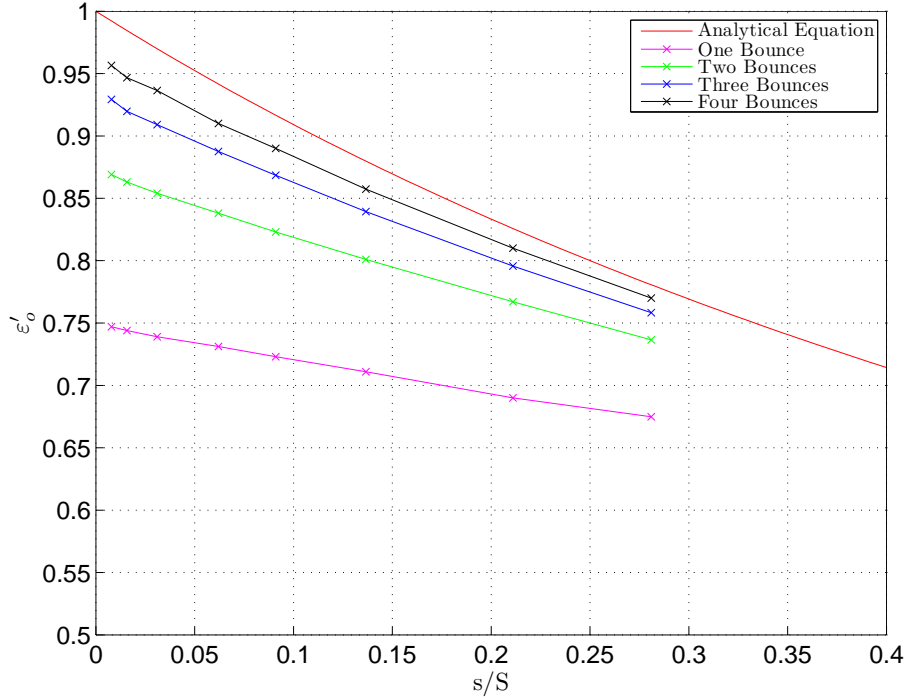


Figure 4.1: The emissivity of the $\varepsilon = 0.5$ greybody cavity is simulated using the propagation algorithm of Equation (3.7). The upper curve is the analytical limit (Equation 3.12) of the cavities' ability to approximate a perfect blackbody as a function of s/S . Several different aperture sizes were simulated to produce a curve in stead of a single point. After each bounce the apparent cavity emissivity increases as the approximation of the reflected radiance integral is more precise.

facet must be sampled. This creates a large number of paths of appreciable radiance that must be calculated to obtain the correct result.

In reality, the greybody radiation in the cavity has experienced an almost limitless number of bounces as radiation is reflected, absorbed and emitted. Referring the simulation back to Equation (3.4), the self-emitted radiance of the visible facets inside the cavity is attenuated by the greybody emissivity, $\varepsilon = 0.5$. The reflected component, then becomes considerable as the number of bounces increases, the paths become longer and the irradiance on the visible facets increases to provide the other half of the blackbody spectrum.

4.2 IR Range Simulations

Bortle [3] performed experiments in AFRL’s IR range to validate the LCAIR code developed by Martinez [17]. Detailed work was performed to produce calibrated and normalized radiance images of the cylinder model in the range. Images were taken in the MWIR and LWIR spectral regions and compared to the output of LCAIR. In each of the figures presented for the IR range simulations, the physical range image will be presented beside the simulated image for comparison.

The following sections will detail limitations and advantages of the single specular bounce LCAIR algorithm, the multi bounce POV stratified hemispherical integration algorithm, and combinations of both.

4.2.1 Single Bounce and Specular Reflectance. To begin, Bortle found that the single bounce, specular reflectance LCAIR algorithm performs well when the model’s surface is highly specular and the specular bounce hits a highly emissive facet, whether model or background.

The gloss black painted model is simulated the best by LCAIR. Although it is highly specular, as can be seen in the peak of the BRDF (Figure 2.12), it is also reasonably emissive over all wavelengths which was seen in the DHR data in Figure 2.10. Figure 4.2 shows the simulation of the gloss black painted cylinder model in the IR range. Visibly, the single bounce specular reflectance simulation is a good match to the physical image. This is achieved because the surface is specular, and where the specular bounce hits other model facets, the emissivity of the gloss black paint is high (see Figure 2.10). The considerable emissivity of the gloss black paint makes the single bounce algorithm approximate the $L_{e_{B_i(\text{Emitted})}}$ term of Equation (3.6) much more accurately. Remember that the observed radiance is a sum of the emitted and reflected radiance, and the emissivity and reflectance coefficients sum to one, $\epsilon(\theta) + \rho(\theta) = 1$. Thus, when one of these dominates, the other term can be considered negligible. Conversely, when the reflectance term dominates, the self-emitted com-

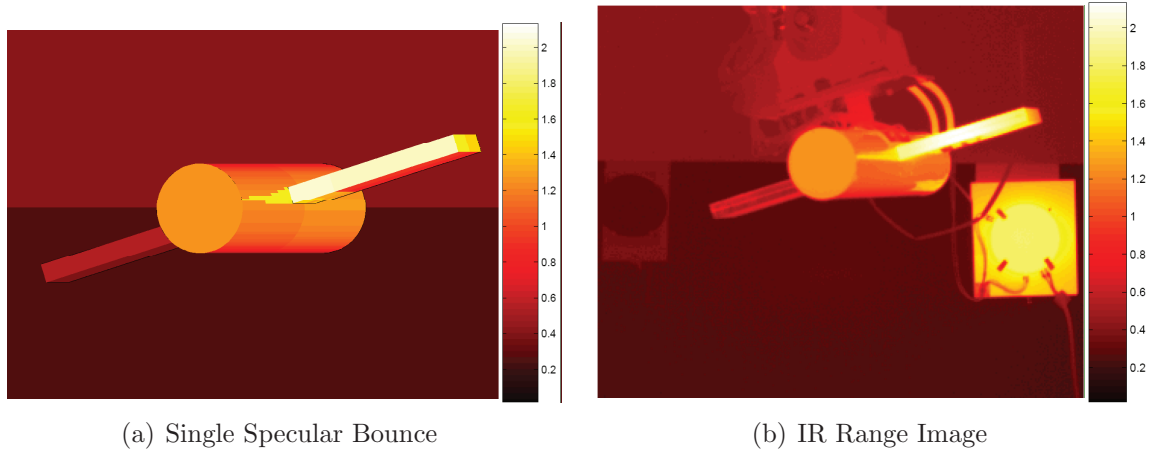


Figure 4.2: The single specular bounce assumption works well for the gloss black case where the model is reasonably emissive, where all specularly reflected rays hit an emissive facet, and the reflected radiance term is approximated well. Colormap units are $[W/(m^2 - sr)]$. Subfigure (b) is reproduced from [3].

ponent becomes negligible and the reflected radiance term dominates the signature, similar to a mirror.

Although the emissivity of the gloss black is only 60-80%, it numerically contributes around 92% of the final result. This is because of the temperature difference between the model and the IR range walls. The model, on average, is 300K, and the walls 260K. Figure 4.3 plots the blackbody spectral radiance curves for those two temperatures. The vertical lines define the MWIR ($3 - 5\mu m$) and LWIR ($8 - 12\mu m$) spectral regions. Note that the 300K curve is much higher than the 260K curve, and when integrated over the MWIR band, the exitant radiance for the 300K blackbody is $1.92 [W/(m^2 - sr)]$, and $0.37 [W/(m^2 - sr)]$ for the 260K blackbody. If the emissivity and reflectance were equal, then the model self emission ($T = 300K$) is still significantly larger than the reflected radiance from the background. However, in the gloss black case, the emissivity is 60-80% and this effect is magnified, where the self emitted radiance is $1.3 [W/(m^2 - sr)]$ and the reflected radiance is $0.11 [W/(m^2 - sr)]$. This is the reason that the algorithm can use a single bounce algorithm and still pro-

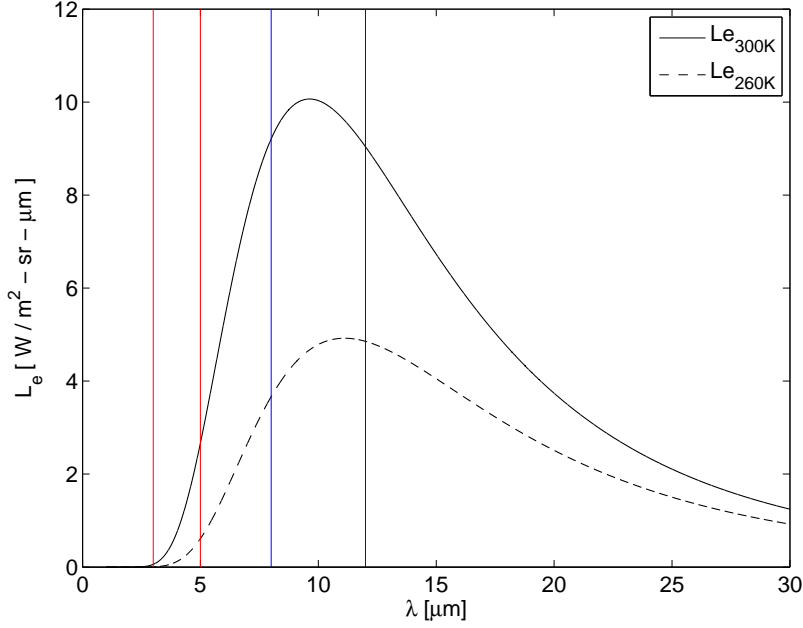
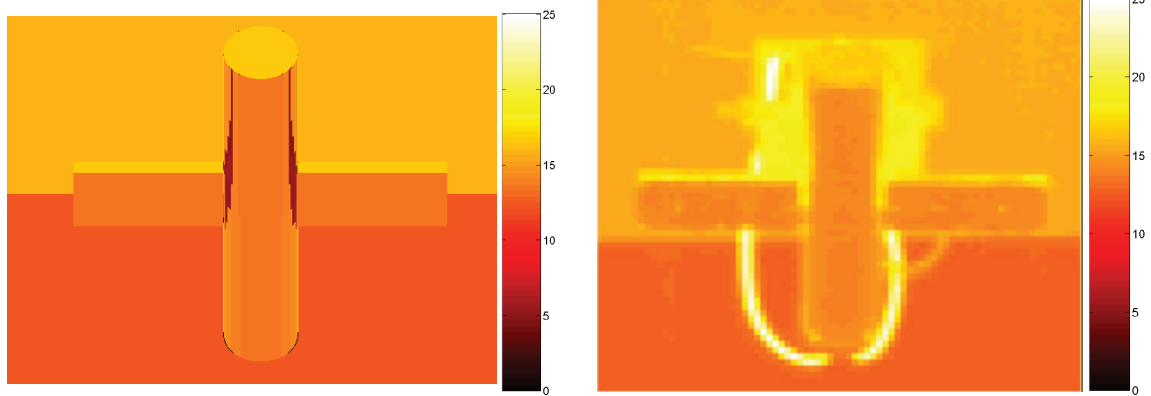


Figure 4.3: The spectral radiance of a 260K and 300K blackbody source are shown. The vertical lines show the extents of the two spectral bands, MWIR ($3-5\mu\text{m}$) and LWIR ($8-12\mu\text{m}$). Colormap units are $[W/(m^2 - sr)]$.

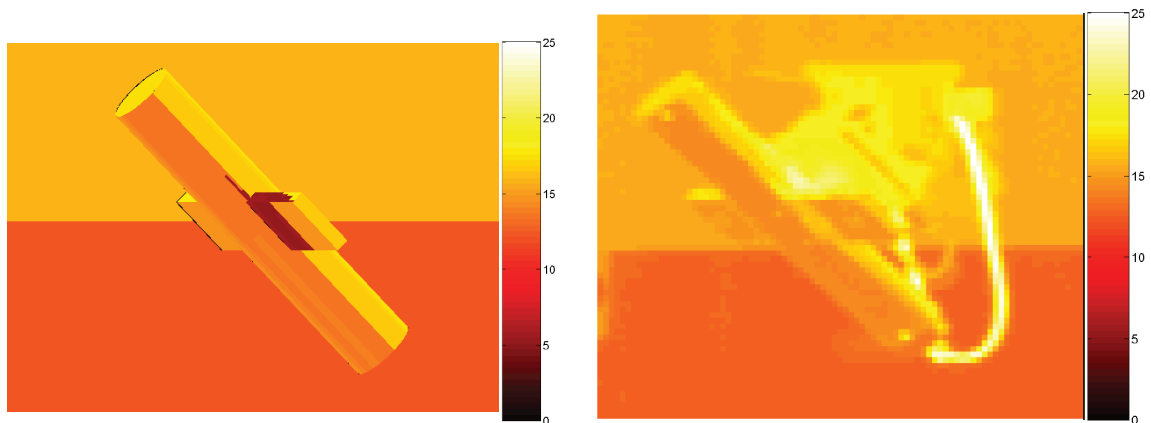
duce suitable results (over 90% correct). The reflected ray will always hit an emissive surface, whether background or another model facet.

However, the single bounce assumption fails in the bare aluminum case, where the model is highly (approximately 90%) reflective. In this case, the reflected term dominates the observed radiance. Even with the MWIR integrated radiance from Figure 4.3, the reflected radiance is now $0.33 [W/(m^2 - sr)]$, and the self-emitted radiance is reduced to $0.19 [W/(m^2 - sr)]$. Thus, with the single bounce, where this reflected radiance is dropped, the result underpredicts by 60%. Figure 4.4 shows this effect; the black regions are where the vector from the observer to the facet is specularly reflected onto one of the wing facets. This has caused the observed radiance from these facets to be severely under predicted, through the process described above. The model is rotated to a pitch of $+45^\circ$ and this is why the top of the cylinder is visible. It is also why the black region is not only in line with the wings in the vertical dimension.



(a) Single Specular Bounce (0° azimuth)

(b) IR Range Image (0° azimuth)



(c) Single Specular Bounce (70° azimuth)

(d) IR Range Image (70° azimuth)

Figure 4.4: The single bounce specular assumption fails when the specularly reflected ray hits a highly reflective (cylinder model wing) facet. In this case, the reflected radiance term is under predicted by 60%. Colormap units are $[W/(m^2 - sr)]$. Subfigures (b) and (d) are reproduced from [3].

The error is caused by the approximation of Equation (3.6). The Le_{B_i} *Emitted* term is the incident radiance on facet A from facet B (refer to Figure 3.30 for facet definitions). A single bounce calculation only calculates the self-emitted portion of Equation (3.4) and ignores the reflected term. The error occurs when the reflectance of facet B is high. Thus, a large portion of emitted radiance is lost and the blackbody radiance is reduced by the low emissivity value.

A second bounce is required to evaluate the irradiance on facet B to calculate the reflected radiance integral of Equation (3.6) to complete the Le_{B_i} *Emitted* term of facet B. This process is nested, and many bounces may have to be calculated (through multiple bounces) to properly evaluate the Le_{B_i} *Emitted* term for reflective surfaces. In theory, an infinite number of bounces are required, however, several assumptions can be made to truncate the iteration and provide a timely solution.

4.2.2 Multiple Bounces and Specular Reflectance. To improve on the simplistic LCAIR algorithm (a single specular bounce), multiple bounces were included in the simulation, whilst still keeping the specular assumption. Multiple bounce calculations do not drop the reflected radiance term from the observed radiance equation, as Equation (3.6) is nested inside itself for each specular bounce. Figure 4.5 shows the results when two specular bounces are calculated from the same simulation as before (LWIR bare aluminum).

The second bounce has added to the emitted radiance of the second facet. In these simple cases, the second bounce hits the background of the IR range, and the algorithm stops. The highly reflective aluminum creates the need to keep tracking bounces throughout the model. In this case, only two bounces are required for all paths to exit to the background, however, with more complicated geometry, the number of bounces required would be more, and will be explored with the A340-300 model simulations.

Another demonstration of how the second bounce contributes to the accuracy of the bare aluminum in the MWIR band simulation is shown in Figure 4.6. In

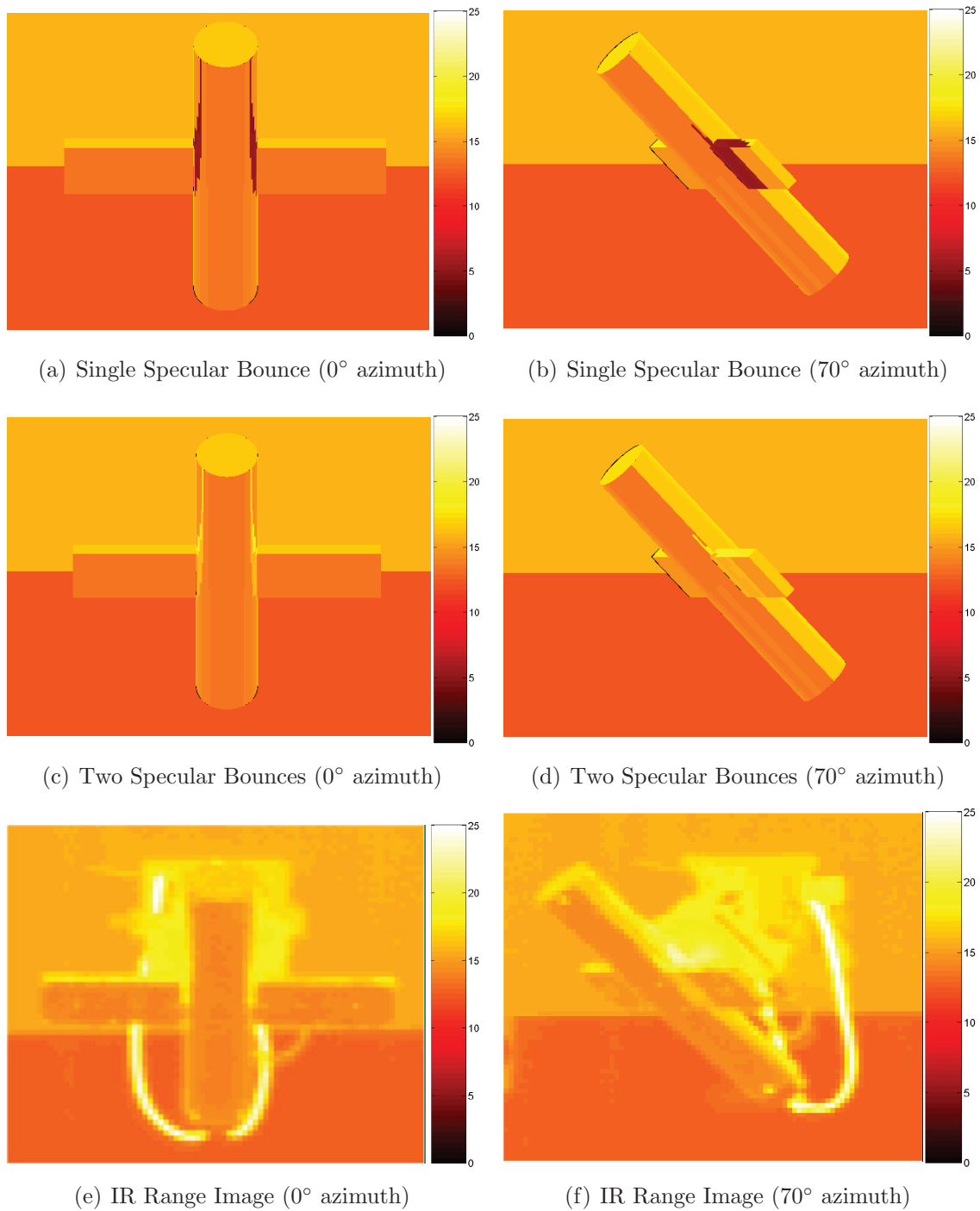
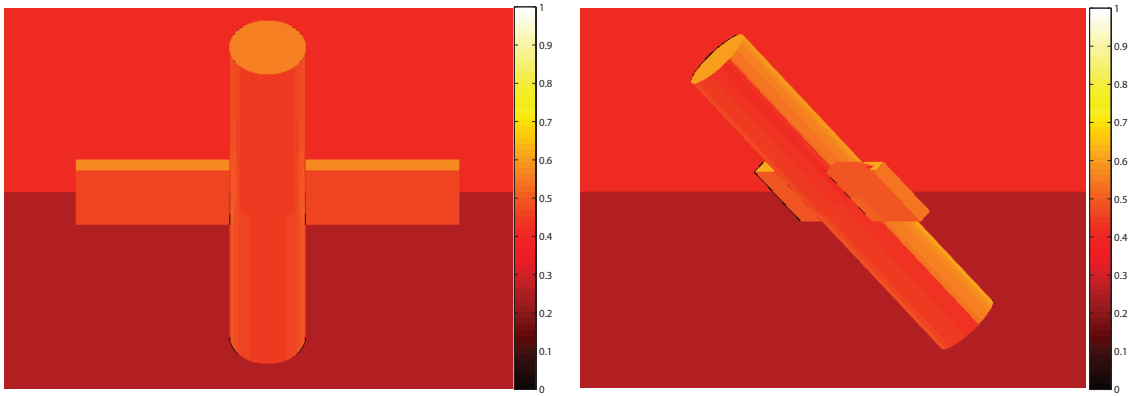
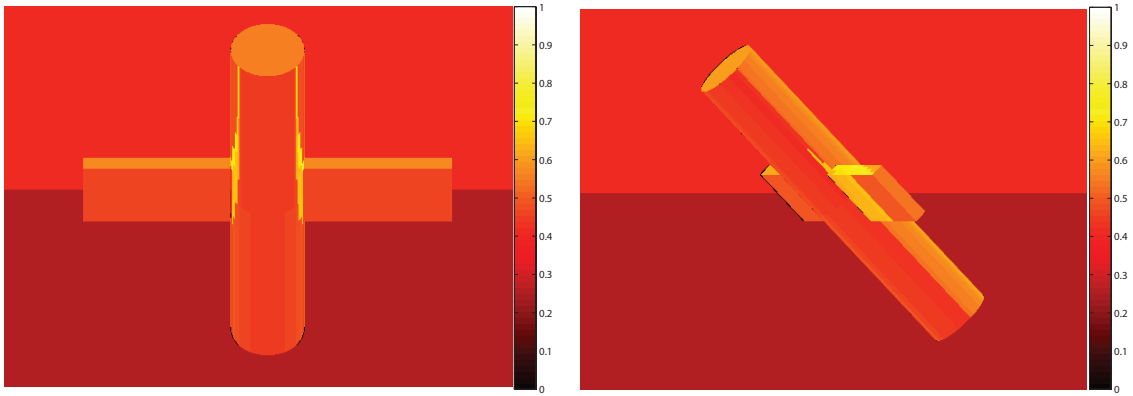


Figure 4.5: By including a second specular bounce, all reflected rays now exit to a highly emissive background facet. Thus, the reflected radiance term of Equation (3.6) is approximated well. Colormap units are $[W/(m^2 - sr)]$. Subfigures (e) and (f) are reproduced from [3].



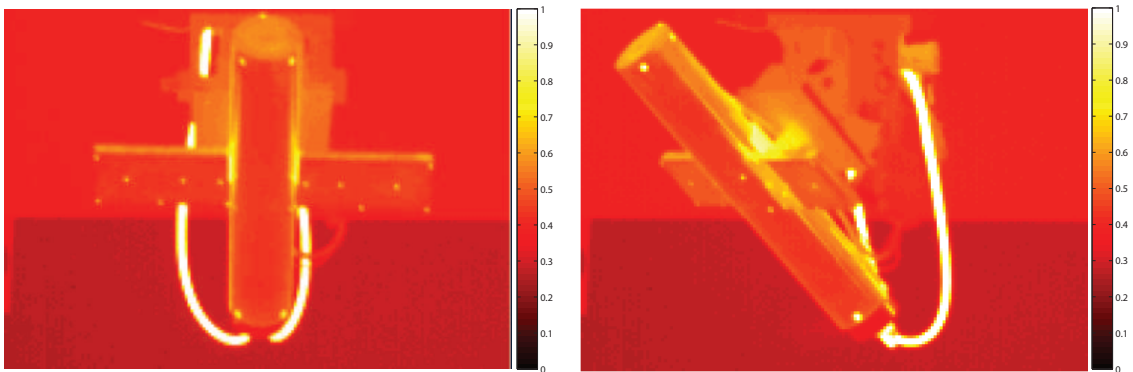
(a) Single Specular Bounce

(b) Single Specular Bounce



(c) Two Specular Bounces

(d) Two Specular Bounces



(e) IR Range Image

(f) IR Range Image

Figure 4.6: By including a second specular bounce, all reflected rays now exit to a highly emissive background facet. Thus, the reflected radiance term of Equation (3.6) is approximated well. Colormap units are $[W/(m^2 - sr)]$. Subfigures (e) and (f) are reproduced from [3].

Figure 4.6 (a), where the first bounce hits another model facet, the 300K self emission is offset by the low emissivity of the aluminum and the result approximately equals the 96% emission of the range walls. This is the reason why there are no vertical black stripes in the simulation, and the models appear to be evenly colored.

This is purely a coincidence, and is a result of wave band, facet temperature, reflectivity and colormap choice. When the second bounce is added, the observed radiance (of facets which have another facet as the specular reflection) is increased beyond the others and produces the yellow glow that can be seen in the range image, Figure 4.6 (e and f). The result is an algorithm that is a closer simulation of the physical processes.

For purely specular reflections, the cylinder model only requires two bounces for all sample rays to exit to the background. After the two bounces, all rays meet the highly emissive background and Equation (3.6) is suitably approximated.

4.2.3 Single Bounce and Integrated BRDF. Figures 4.5 (a and b) show the single bounce simulations for the bare aluminum LWIR simulations. The change in magnitude of observed radiance between single and double bounce paths is sharp. This gradient is a result of the specular assumption, where one ray is used to sample (represent) the whole hemisphere. In reality, there is a gradual change from a facet which has all background in its hemispherical view and one which has some model facets. Additionally, the specular lobe has some width to it (recall Figure 2.9), thus, significant reflected radiance can come from off specular angles.

Relaxing the strict specular assumption and integrating across the BRDF smooths this gradient, to improve the algorithm further. Figure 4.7 shows the result of integrating across the hemisphere with the BRDF inside Equation (3.6), for the bare aluminum LWIR simulation, with a single bounce. The result is that the gradient between radiance values has been smoothed, but the single bounce reflected radiance contribution failure is still present. This figure was included to show that just purely integrating over the BRDF with a single bounce calculation does not automatically



(a) Single Specular Bounce



(b) Single Integrated BRDF Bounce

Figure 4.7: (a) Zoomed-in image of Figure 4.5 (a). Even when the BRDF is integrated over a single bounce (b), the same issues from a highly reflective facet occur. This indicates that the specular assumption is quite valid as the two results look similar. The effect of the integration can be seen in the gradient between the yellow and brown/black facets. In (b), there is a smoother gradient as there are some red facets that separate the yellow and brown/black ones. Colormap units are $[W/(m^2 - sr)]$.

provide an accurate simulation; integrating the BRDF over multiple bounces is required for the highest fidelity solution.

4.2.4 Multiple Bounces and Integrated BRDF. To gain the best result possible, multiple bounces whilst integrating the BRDF must be calculated. Previously, the cylinder model can only support two specular bounces before the paths exit to background. However, by integrating the BRDF over the full hemisphere, an infinite number of paths and bounces are created. Section 3.5.5 justified the choice for truncating the number of paths (as highly specular surfaces are being simulated) through only integrating across the BRDF peak region.

Calculating the multiple bounces (whilst integrating the BRDF) takes more time than using the purely specular assumption; however, as shown in the previous sections, it is more accurate. Similar to the multiple specular bounce algorithm, Figure 4.8 shows the LWIR bare aluminum result when two bounces are integrated across the BRDF peak region, previous figures are included for reference as subfigures. The bare aluminum MWIR result is included in Figure 4.9 also for comparison to Figure 4.6 where two specular bounces are calculated.

As the number of bounces is increased, the number of paths also increases, approximating the reflected radiance integral more accurately. Figure 4.10 shows the reflected radiance term of facet #1388 converging to the final result as the number of bounces increases. Previously, only two specular bounces were possible, however, with the wider angular search region, up to four bounces are possible. These further bounces have an appreciable effect on the integral approximation as they are in the peak region. The convergence rate slows as the geometry becomes more complex, thus more paths (more bounces) are required to evaluate the reflected radiance integral properly.

4.2.5 Algorithm of Choice. From the results above and Chapter III, the most efficient algorithm is very much dependent upon the BRDF of the material. The



(a) Two Specular Bounces

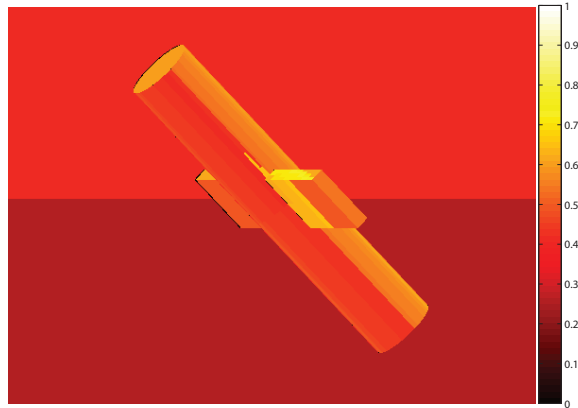


(b) Two BRDF Bounces

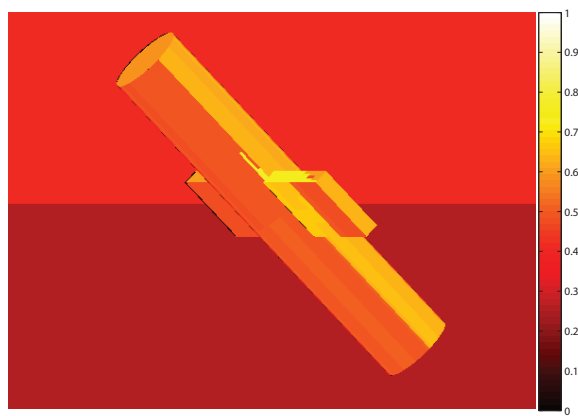


(c) IR Range Image

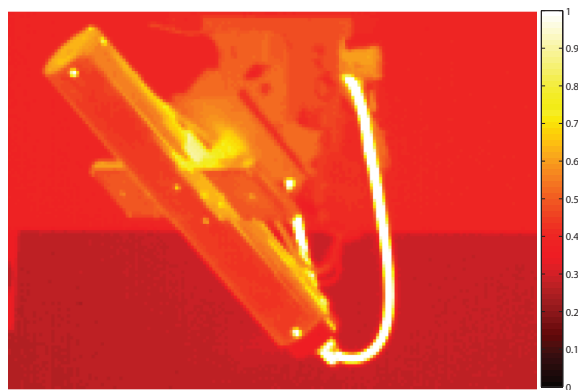
Figure 4.8: The addition of the second integrated BRDF bounce *fills in* the under prediction, similar to the specular reflectance case. When compared to the real image, the two BRDF bounce algorithm performs well, however, it is not superior to the double bounce specular algorithm. Colormap units are $[W/(m^2 - sr)]$. Subfigure (c) is reproduced from [3].



(a) Two Specular Bounces



(b) Two BRDF Bounces



(c) IR Range Image

Figure 4.9: The MWIR result is similar to the LWIR simulation, the second BRDF bounce provides the increased reflection in the wing fillet area. The MWIR range image is a much higher resolution image than the LWIR image. This increased resolution allows a greater comparison of the simulation results. Colormap units are $[W/(m^2 - sr)]$. Subfigure (c) is reproduced from [3].

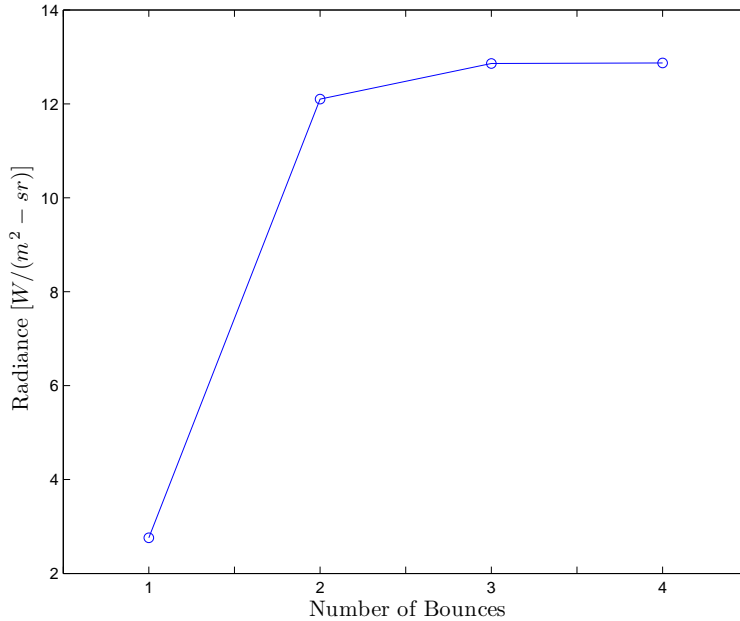


Figure 4.10: The convergence to the final result (to match the IR Range image) for facet #1388 is shown. Note that it takes four bounces to achieve the correct result as a result of integrating the BRDF over the peak region.

computation time is also dependent upon the number of paths that carry appreciable flux; for diffuse surfaces, this number can be considerable, and for more specular surfaces, the number is reduced.

The A340-300 to be simulated in the next section is assumed to be constructed with bare aluminum. Thus, the specular assumption will be valid and is used.

4.3 A340-300 Simulations

The final simulation that was performed is the engagement scenario of the A340-300 by a threat located outside a major airport. Section 3.7 dealt with the setup and theory of the simulation, and the results are included below. The simulations are performed to show the end application of the IR simulation process. The scenarios are broken into MWIR and LWIR simulations, and for position 1, the effect of increasing number of bounces will also be shown. The process of calculating the result will be shown for position 1, whilst only the final results for positions 2 and 3 will be shown.

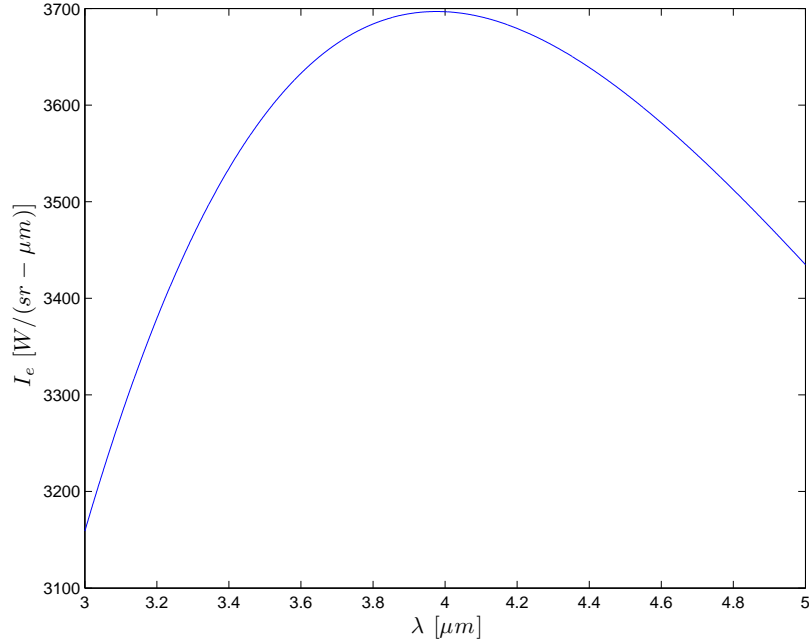


Figure 4.11: The output of the MWIR simulation at Position 1 is target intensity with no atmospheric included. Note the wavelength of the peak in the curve. $4\mu m$ corresponds to the peak emission of a 724K blackbody source. This temperature is a weighted combination of the exhaust plume and turbine hot parts annulus. The background spectral peak is dwarfed by the magnitude of the hotter Planckian curve, and is not visible.

4.3.1 Position 1 - MWIR. The first position simulates when the observer (detector) is behind the aircraft (refer to Figure 3.35), where the detector is 1km behind, 500m to the side and 50m below the aircraft. The aircraft also has a pitch of 10° to simulate the landing attitude.

The MWIR simulation ($3 - 5\mu m$) is performed and the results are included below. The output of the propagation algorithm is spectral intensity, $I_{e \text{ Target}}$ from Equation (3.13), observed from the wireframe model with no atmospheric added. This spectral intensity is shown in Figure 4.11. The path transmission, as computed by MODTRAN, is applied to gain the apparent target intensity, and is then converted to apparent target irradiance at the detector with Equation (3.16). The results of this process are shown in Figure 4.12. Once the spectral apparent target irradiance is calculated, the background and path radiances, again computed by MODTRAN,

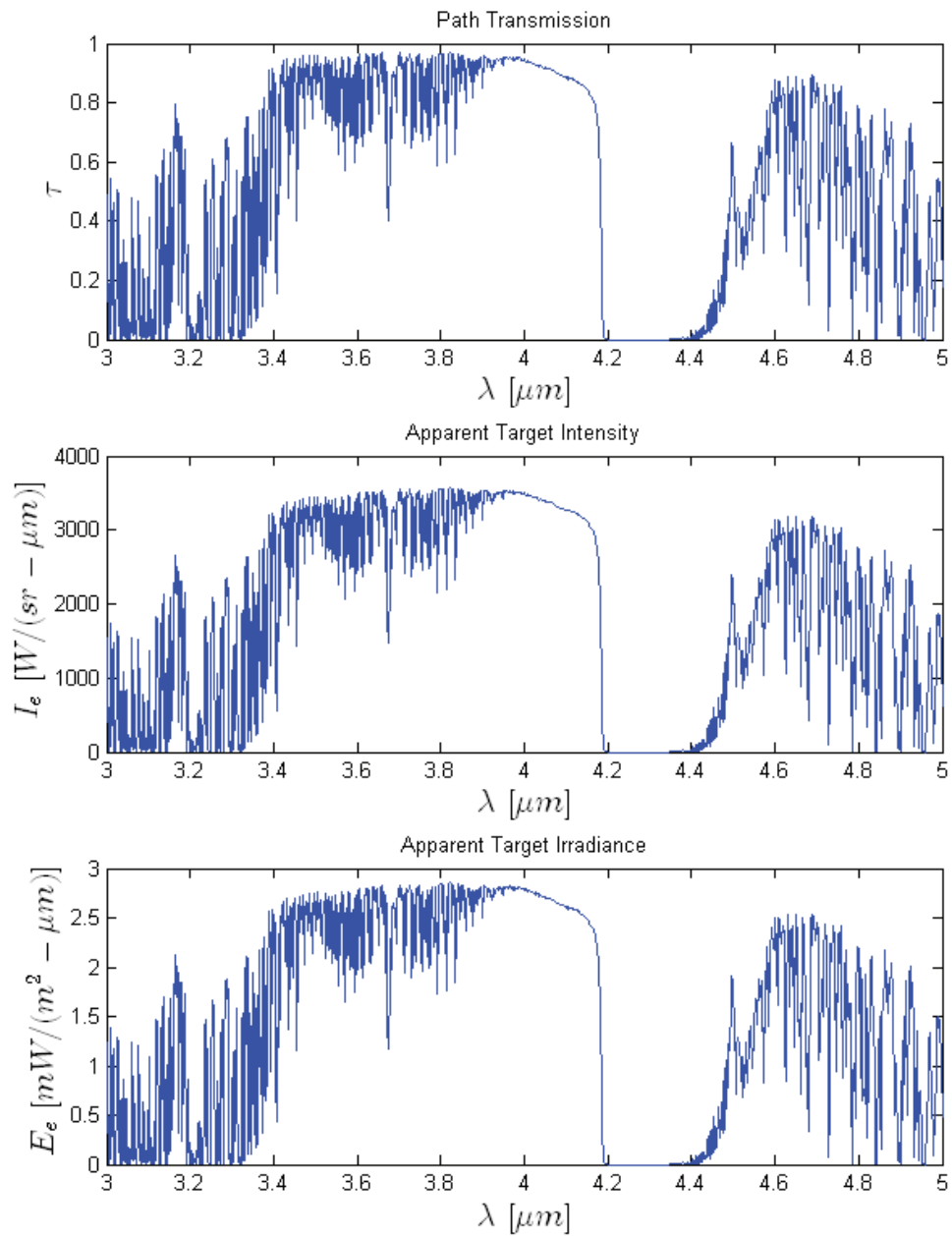


Figure 4.12: Spectral transmission, as computed by MODTRAN, is applied to the target intensity, from Position 1, and is converted to irradiance at the optic.

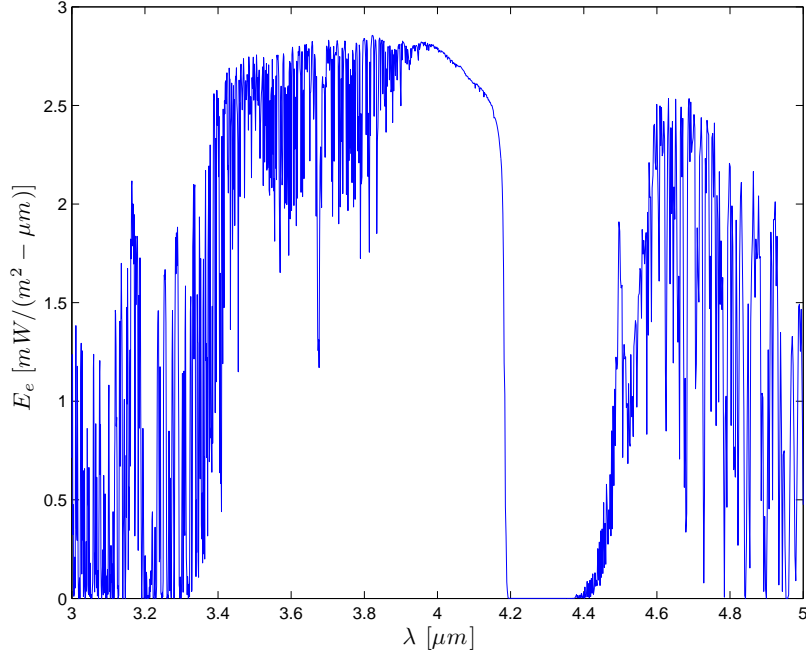


Figure 4.13: The spectral irradiance as measured at the detector, from Position 1, with all atmospheric included.

are passed to Equation (3.18) to gain the total received irradiance at the optic which is shown in Figure 4.13.

These figures all show spectral irradiance or intensity. To calculate the output of the single-pixel detector, the spectrum must be integrated to calculate total irradiance across the band. To give a feel for the scalar magnitudes involved between the different terms of Equation (3.18), they are listed in Table 4.1 for each simulation. The total MWIR irradiance received at the detector is $3.034 \times 10^{-3} W/m^2$; thus, the required NEI with a SNR of 10 is $3.034 \times 10^{-4} W/m^2$. The integrated irradiance in the MWIR band does not vary within three significant figures when varying the number of calculated bounces. This is because the observation angle only supports specularly reflected paths that hit the exhaust plume or hot parts annulus on the first bounce. There are paths with up to four bounces possible, however, they do not carry significant radiance and do not contribute appreciably to the result.

Figure 4.14 shows the image of the aircraft rotated to the view angle of position 1. An image where the background is also drawn is included to show contrast between

Table 4.1: Position 1 Detector Irradiance.

Band	# Bounces	$E_e Tgt App$ [W/m^2]	$E_e Bg App$ [W/m^2]	$E_e Path App$ [W/m^2]	$E_e Total App$ [W/m^2]
MWIR	1	3.03×10^{-3}	5.64×10^{-7}	3.23×10^{-7}	3.03×10^{-3}
	2	3.03×10^{-3}	5.64×10^{-7}	3.23×10^{-7}	3.03×10^{-3}
	3	3.03×10^{-3}	5.64×10^{-7}	3.23×10^{-7}	3.03×10^{-3}
	10	3.03×10^{-3}	5.64×10^{-7}	3.23×10^{-7}	3.03×10^{-3}
LWIR	10	3.61×10^{-3}	6.55×10^{-5}	2.23×10^{-5}	3.56×10^{-3}

the aircraft and background irradiance. It is important to remember that the detector has to integrate over the whole FOV, which includes the background. Figure 4.14 (b) shows this view, where the exhaust direct emission and reflections off the fuselage are what lifts the signature out of the atmospheric background and electronic noise to enable detection.

4.3.2 Position 1 - LWIR. The previous section demonstrated the process and results for the MWIR case. For the LWIR case, the process is the same, however, the balance between the signature elements differs and magnitudes change. In the LWIR band, the background becomes more important as the background self emission peaks in the LWIR band. Figure 4.15 shows the spectral target intensity for the LWIR case, and is applied to the spectral transmission of Figure 4.16 to calculate the total apparent irradiance at the optic from Position 1, which is shown in Figure 4.17. Figure 4.20 shows the view of the aircraft at Position 1 in this LWIR case. Note the increased contribution from the terrain. The terrain's temperature is $300K$ which has a self-emission peak at $10\mu m$. This peak lies in the middle of the LWIR band, hence, the increased earth shine reflection off the aircraft compared to the MWIR case.



(a) Aircraft Only



(b) Aircraft plus Background

Figure 4.14: The two MWIR images show the orientation of the aircraft at Position 1 when viewed from the observer with (a) the background removed, and (b) the background included to show contrast between the aircraft emission and reflection, and the background irradiance. Colormap units are $[W/(m^2 - sr)]$.

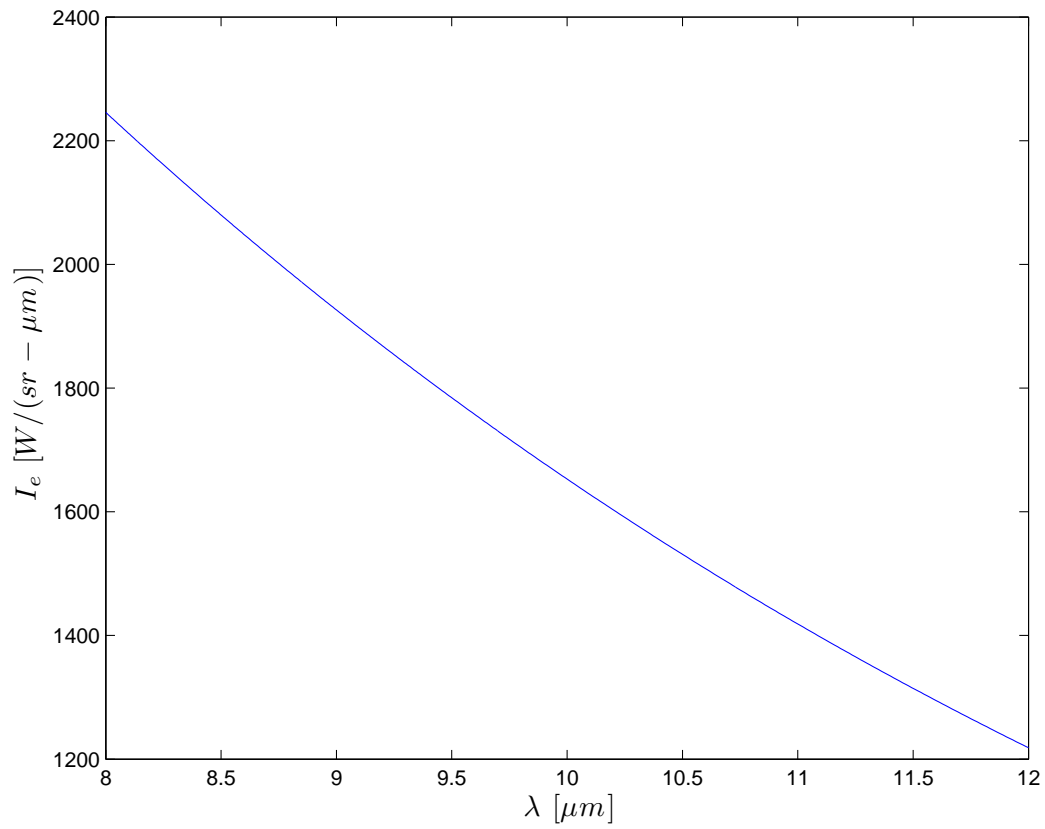


Figure 4.15: The output of the LWIR simulation from Position 1 is target intensity with no atmospherics included.

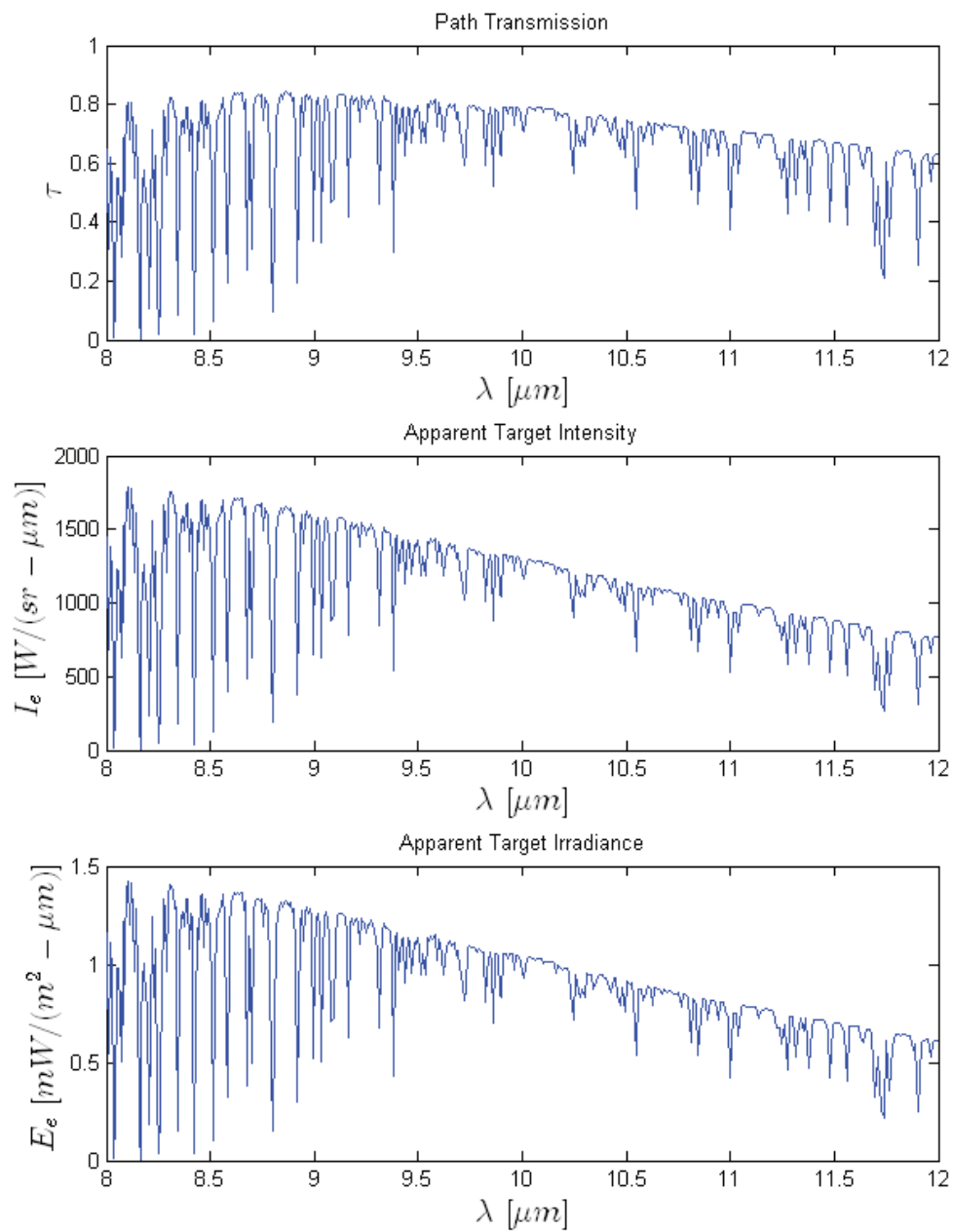


Figure 4.16: Spectral transmission, as computed by MODTRAN, is applied to the target intensity and converted to irradiance at the optic from Position 1.

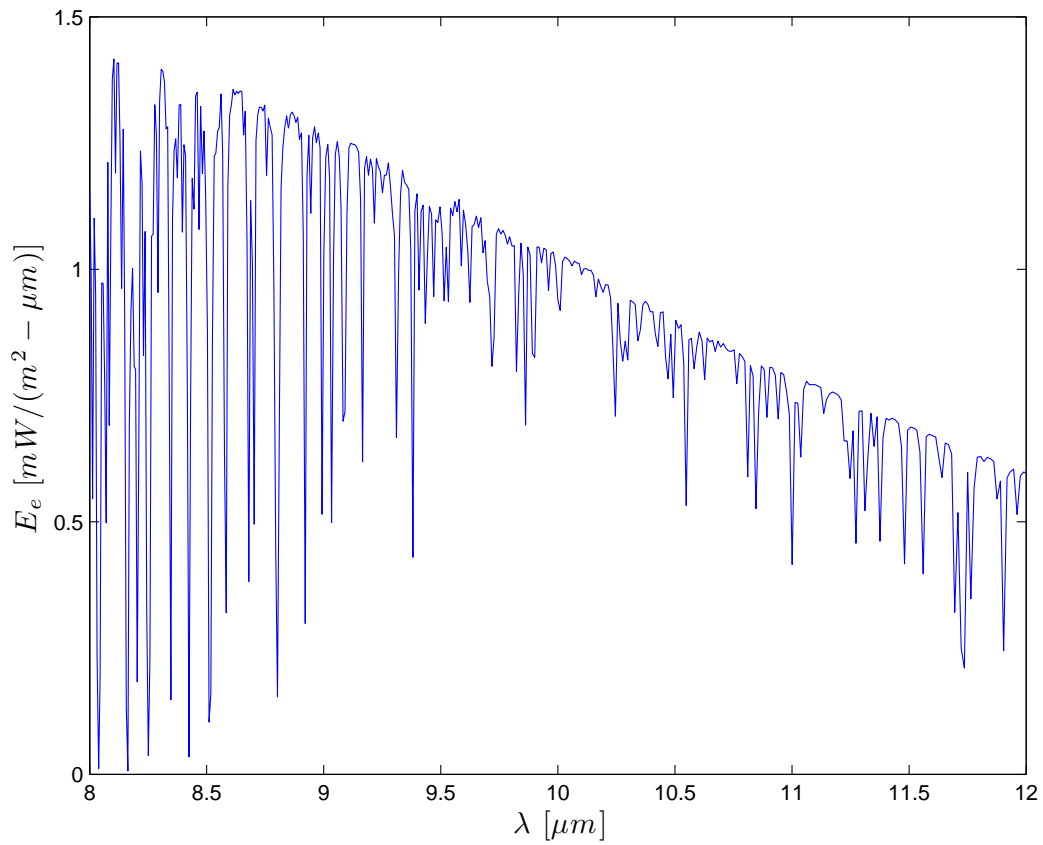


Figure 4.17: The total irradiance as measured at the optic, from Position 1, with all atmospheric included.



(a) Aircraft Only



(b) Aircraft plus Background

Figure 4.18: The two LWIR images show (a) the background removed, and (b) the background included to show contrast between the aircraft emission and reflection, and the background irradiance at Position 1. Note the increased contribution in the LWIR band from the ground reflection off the aircraft. The ground (302.5K) has its peak emission at about $10\mu m$. Colormap units are $[W/(m^2 - sr)]$.

Table 4.2: Position 2 Detector Irradiance.

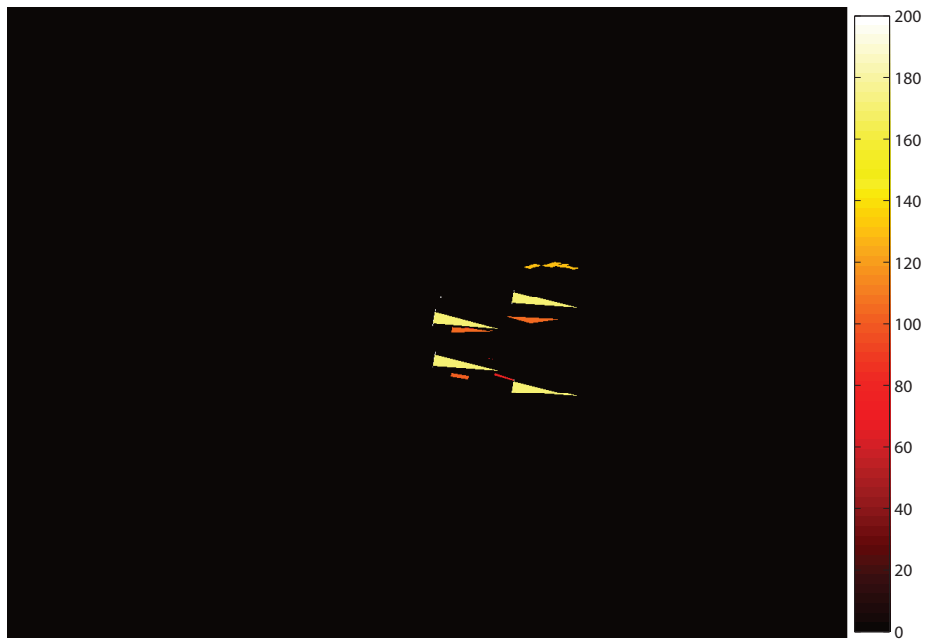
Band	# Bounces	$E_e Tgt App$ [W/m^2]	$E_e Bg App$ [W/m^2]	$E_e Path App$ [W/m^2]	$E_e Total App$ [W/m^2]
MWIR	10	7.13×10^{-3}	5.08×10^{-6}	2.19×10^{-6}	7.12×10^{-3}
LWIR	10	4.18×10^{-2}	5.90×10^{-4}	1.09×10^{-4}	4.13×10^{-2}

4.3.3 Position 2. The second position provides a side-on view of the aircraft, this time at a closer range, 509 *m* compared to 1,119 *m* for the first position. Figures 4.19 and 4.20 show the view of the aircraft at Position 2 from the observer's position in the MWIR and LWIR bands, respectively. Again, note that in the LWIR case the terrain reflection is increased. Also note, that from this angle (Position 2), all four exhaust plumes are visible. However, as the hot engine internals are not visible at this angle, the intensity emitted from the aircraft is much less, 1852 *W/sr* versus 3800 *W/sr* for Position 1 in the MWIR case. However, as the range is reduced, the irradiance at the detector increases to be comparable to the first position, a coincidence of the two ranges. The results for this second position are listed in Table 4.2.

4.3.4 Position 3. The third and final case simulated is Position 3. The aircraft is 3 km out from the runway at a height of 150 *m*, and the detector is viewing the aircraft from front on. Figures 4.21 and 4.22 show the attitude of the aircraft as viewed from the observer. Note the large contribution from the background and reduced contribution from the engines, because of the aircraft orientation. Table 4.3 lists the results from the simulations. The LWIR case was simulated several times, whilst varying the number of bounces, similar to the MWIR simulation at Position 1. This time, the integrated irradiance does vary with the number of bounces. The observation angle in this case can support multiple bounces and the observed irradiance increases as each bounce is included, up to four bounces where all paths of appreciable radiance exit to the background. These multiple bounce paths occur as the reflected rays bounce between the fuselage, wings and engines. Figure 4.23 shows



(a) Aircraft Only



(b) Aircraft plus Background

Figure 4.19: The two MWIR images show (a) the background removed, and (b) the background included to show contrast between the aircraft emission and reflection, and the background irradiance at Position 2. Colormap units are $[W/(m^2 - sr)]$.



(a) Aircraft Only



(b) Aircraft plus Background

Figure 4.20: The two LWIR images show (a) the background removed, and (b) the background included to show contrast between the aircraft emission and reflection, and the background irradiance at Position 2. Note the increased contribution in the LWIR band from the ground reflection off the aircraft. The ground (302.5K) has its peak emission at about $10\mu m$, in the middle of the LWIR band. Colormap units are $[W/(m^2 - sr)]$.

Table 4.3: Position 3 Detector Irradiance.

Band	# Bounces	$E_e Tgt App$ [W/m^2]	$E_e Bg App$ [W/m^2]	$E_e Path App$ [W/m^2]	$E_e Total App$ [W/m^2]
MWIR	10	5.73×10^{-4}	7.09×10^{-7}	4.03×10^{-7}	5.72×10^{-4}
LWIR	1	4.89×10^{-3}	8.25×10^{-5}	2.77×10^{-5}	4.83×10^{-3}
	2	5.27×10^{-3}	8.25×10^{-5}	2.77×10^{-5}	5.22×10^{-3}
	3	5.38×10^{-3}	8.25×10^{-5}	2.77×10^{-5}	5.33×10^{-3}
	4	5.43×10^{-3}	8.25×10^{-5}	2.77×10^{-5}	5.38×10^{-3}
	10	5.43×10^{-3}	8.25×10^{-5}	2.77×10^{-5}	5.38×10^{-3}

the different signature between a single bounce and ten bounces, where the single bounce signature is 10% less than the multiple bounce simulation.

4.3.5 A340-300 Simulation Summary. The simulations which calculate the IR signature of the A340-300 aircraft all produce similar values of irradiance at the detector. The strongest signal is from Position 2 in the LWIR band, $4.13 \times 10^{-2} W/m^2$, and the smallest is from Position 3 in the LWIR, $5.72 \times 10^{-4} W/m^2$. The MWIR irradiance was on the order of $10^{-3} W/m^2$. Thus, when applying the SNR condition, a detector must have an NEI no greater than $5 \times 10^{-5} W/m^2$ to detect and track the aircraft at all three positions.

4.4 Chapter Summary

This Chapter has shown the results of the cavity blackbody source, IR Range, and the A340-300 engagement simulations. The cavity blackbody simulations demonstrated that the propagation algorithm is numerically accurate, and thus, provides a correct result. The IR Range simulation showed that the propagation algorithms, through increasing the number of bounces, were able to more accurately predict the IR signature of the cylinder model when compared to the LCAIR algorithm of [3] and [17]. Finally, the A340-300 simulations show the utility of the IR signature sim-



(a) Aircraft Only



(b) Aircraft plus Background

Figure 4.21: The two MWIR images show (a) the background removed, and (b) the background included to show contrast between the aircraft emission and reflection, and the background irradiance at Position 3. Colormap units are $[W/(m^2 \cdot sr)]$.



(a) Aircraft Only

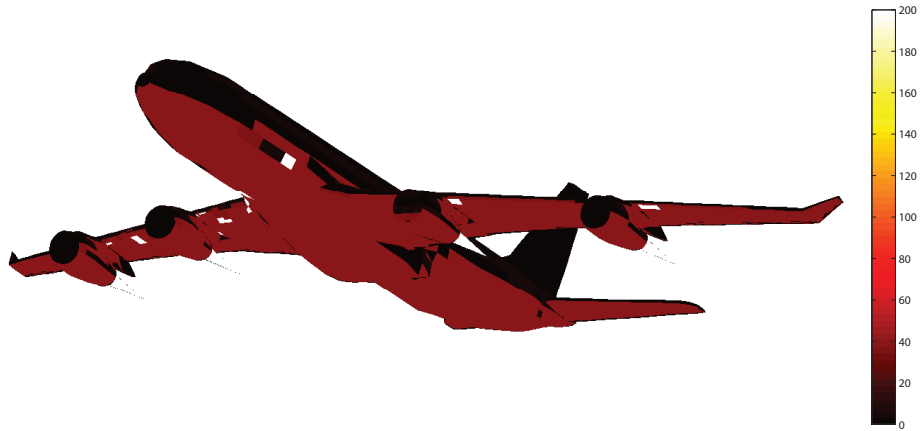


(b) Aircraft plus Background

Figure 4.22: The two LWIR images show (a) the background removed, and (b) the background included to show contrast between the aircraft emission and reflection, and the background irradiance at Position 3. Note the increased contribution in the LWIR band from the ground reflection off the aircraft. The ground (302.5K) has its peak emission at about $10\mu m$. Colormap units are $[W/(m^2 - sr)]$.



(a) Single Bounce



(b) 10 Bounces

Figure 4.23: The two LWIR images show the increased signature level with the multiple bounce simulation at Position 3. Note the reduced number of black facets and the specular reflection off the fuselage in (b). Colormap units are $[W/(m^2 - sr)]$.

ulation code, by calculating the irradiance of the aircraft at the optic of the observer, for several scenarios.

These results will be analyzed and discussed in detail in Chapter V.

V. Conclusions and Recommendations

The aim of this thesis was to show how BRDFs affect IR signature models. Chapter IV showed the effects of including the BRDF versus a specular reflection assumption. For the most part, the specular assumption worked quite well for the bare aluminum and gloss black surfaces as their reflectance distributions were very close to specular. Secondly, the effect of the number of bounces was shown and proved important when a highly reflective surface was simulated. Recall that each time the reflected radiance term dominates, through a high reflectance, $\rho(\theta)$, value, another bounce must be calculated to ensure the observed radiance properly evaluated.

Additionally, computation time was investigated and was highly dependent upon the number of paths carrying appreciable radiance. For a perfectly specular surface, there is only one path per facet, and for a diffuse surface, every path ($\#\text{facets}^{\#(\text{bounces})}$) is important. This was shown in the cavity blackbody analysis, where the simulation was stopped after four bounces.

Considerable work was also performed to optimize the sampling rate to ensure the BRDF was sampled appropriately, ensuring a correct result, whilst keeping the simulation time to a minimum. It is possible to write an algorithm that is capable of solving every combination of BRDF, geometry and required accuracy. However, it would not be efficient, but with a few simplifications (similar to the ones described in Chapter III), the algorithm could be tailored to provide a much improved run time.

For bare aluminum and gloss black painted surfaces, the specular assumption works well and negates having to integrate the full BRDF.

5.1 LCAIR Algorithm Summary

Overall, LCAIR, with its single bounce algorithm and purely specular assumption, predicted the observed radiance well for situations where the following two conditions are satisfied.

- The specular bounce from the first facet must hit a facet with a high emissivity, whether background or another model facet.
- The reflectance distribution of the surface must satisfy the specular assumption. This means that the BRDF of the surface must resemble a delta function centered on the specularly reflected direction.

When these two conditions are met, then the LCAIR algorithm calculates the correct result rather well. However, when one or both of the conditions are not met, then the result is incorrect. The second requirement was not demonstrated, however, Sections 3.3 and 3.3.3 have dealt with the form of the BRDF, regarding computation time, sampling resolution and hemispherical irradiance integral approximations.

A simple improvement to the LCAIR algorithm would be to include multiple bounces. The specular assumption removes the BRDF integration overhead by simply using reflectance data on each bounce. Increasing the number of bounces from one to many would not affect the run time appreciably as most facets only support a few bounces. This would still allow trend analysis as a function of azimuth (that was demonstrated in [17]) to be performed in a comparable timeframe.

5.2 *Lessons Learned*

Similar to the lack of *a priori* information that hinders an algorithm's performance, the same can be said of the education process, and hindsight is always 20/20.

Most open source or even commercial ray-tracing programs are written in C. The decision to write a ray-tracer in Matlab[®] proved problematic, and more time than perhaps was warranted was spent on the 3D wireframe and ray-tracing portions of the software. This decision was made due to the author's unfamiliarity with C. The extra effort involved with coding in Matlab[®] compared with the learning curve of C meant that time was spent on the framework of the code, rather than implementing the propagation algorithms through exercising the model. An improvement to this would be to utilize the power of a commercial product and write a plug-in (or similar

code) to interface with the 3D and ray-tracing engine. Matlab[®] is not optimal for complex 3D graphics when thousands of facets are involved. A move to C or another software product is recommended.

Additionally, time was spent attempting use the radiosity algorithm because of the property that it calculates a solution for every observation angle. The radiosity method was rejected because of the sampling resolution requirement of the specular BRDFs. A better approach would have been to implement the POV solution first, and then experiment later with global illumination algorithms. Global illumination algorithms typically are more complex, whether numerical quadrature based like radiosity, or probabilistically based like the Monte Carlo method.

5.3 Recommendations for Future Work

The first recommendation for future efforts in this area is to optimize the ray-tracing algorithm, which will provide a more timely solution. OpenGL software routines provide access to the computer's graphics hardware, which could be used to ray-trace the scene many orders of time faster. One method previously discussed is to write a plugin (for Blender3D or similar product) that exploits the power of the 3D engine.

Another area that provides promise for accurate BRDF calculations is a technique called Photon Mapping. It is a probabilistic technique where many photons are emitted from each source and traced through the model. Each surface interaction (reflection) is recorded in a photon map, and the photon density (observed radiance) from each surface is estimated. The estimate improves as the number of photons increases. This method can provide accurate results, however, as it is a Monte Carlo technique, it does not provide the quick solution required for trend analysis.

LCAIR was originally developed as a quick IR signature trend analysis tool, to be used instead of higher fidelity models like Spectral and Inband Radiometric Imaging of Targets and Scenes (SPIRITS). However, this thesis has shown that having

to integrate the BRDF for each facet is time consuming, and probably unsuitable for trend analysis work, where hundreds of observation angles are required. To provide a timely trend analysis result, the specular assumption should be used, however, this assumption requires the reflectance distribution of the material to be highly specular. This requirement limits the range of materials that can be simulated, as not all materials are highly specular.

Aside from the accuracy of the algorithms, the LCAIR software has not been used in a thorough analysis of a specific aircraft's IR signature. Simulations with physically measured surface reflectance distributions and correctly measured temperatures could be performed to analyze, in detail, the signature from an aircraft or other targets of interest. Other additions to the model could include the detector system, including material spectral efficiency, optics transmissivity, and electronic noise sources. This would provide a whole electro-optical system simulation, which would be able to simulate engagement scenarios and evaluate various detection strategies. Additionally, including an imaging detector model, whether a scanning mirror or focal plane array, would provide even greater scope for system simulation and analysis.

5.4 Conclusion

Several algorithms have been presented and implemented for simulating IR signatures. Assumptions of specular reflectance can reduce computation times significantly, however, the BRDF must very closely resemble a delta-function at the specularly reflected angle.

Trend analysis requires a fast algorithm, and works well with the specular assumption, however, a balance between processing time and accuracy is required.

Finally, multiple bounce calculations are important when the geometry is enclosed or complex (which will support the multiple bounces), and also when highly reflective surfaces are used which require the reflected radiance term to be calculated with additional bounces.

Appendix A. Simple Geometric Analytical Proofs

Two of the simulations performed to provide a qualitative check of the algorithms are included in this appendix for reference. They were chosen as an analytical solution can be gained to compare with the numerical result. In both cases, any contribution from the background is ignored.

A.1 Two Plates

The first simulation is two $20\text{ cm} \times 10\text{ cm}$ rectangular plates that are joined at their short edges at right angles. Figure A.1 is a depiction of the setup. The first plate has a temperature of 800 K and is a perfect blackbody Lambertian emitter. The second plate is a perfect diffuse reflector with $\rho = 1$. The temperature is 300 K , although, it does not matter as $\varepsilon = 0$. The observer is located normal to the reflecting surface such that the emitting surface is not visible.

To analytically calculate the intensity viewed by the observer, the irradiance onto the second plate must be calculated. Small angle approximations cannot be used as the geometry is too small and a diffuse reflectance is being used, thus the integral must be evaluated. The irradiance on the second plate is calculated in Equation (A.1), and the radiance emitted from a perfectly diffuse surface is simply the irradiance multiplied by the reflectance and divided by π (Equation (A.2)). The intensity as viewed at the observer's location is calculated with Equation (A.3) from the emitted radiance.

$$E_e = \int_{A_{\text{source}}} \frac{L_e(T = 800\text{K}) \cos(\theta_s) \cos(\theta_d)}{R^2} dA_s \quad (\text{A.1})$$

$$L_e = \rho \frac{E_e}{\pi} \quad (\text{A.2})$$

$$I_e = \int_{A_{\text{source}}} L_e \cos(\theta_s) dA_s = \int_{A_{\text{source}}} \rho \frac{E_e}{\pi} dA_s = 21.53 \left[\frac{\text{W}}{\text{sr}} \right] \quad (\text{A.3})$$

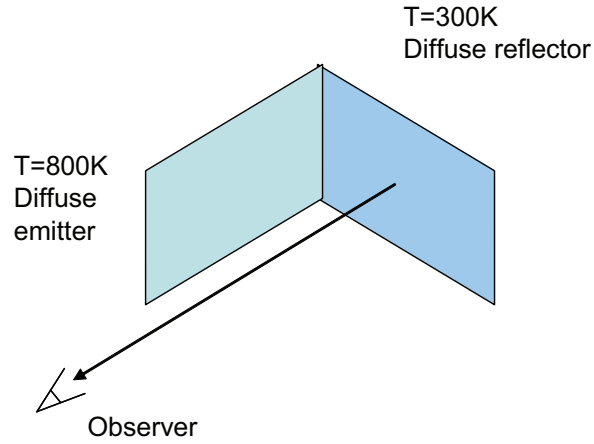


Figure A.1: Geometrical setup for the two plates simulation. The observer cannot see the emitting plate, only the diffuse reflection from the other.

The intensity at the observer is then 21.53 W/sr . The results from the simulation is shown in Figure A.2, where the intensity from each differential piece of area is shown. The output from the simulation is 22.05 W/sr which is 102% of the analytical result.

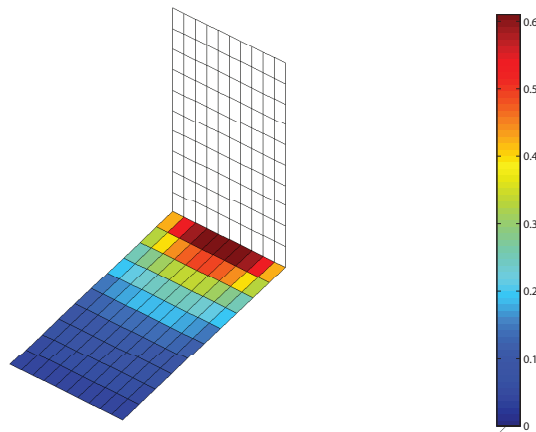


Figure A.2: The result of the two plates simulation is shown. Note the gradient profile in the irradiance on the second plate. The observer is looking vertically down in this figure. Colormap units are $[W/sr]$.

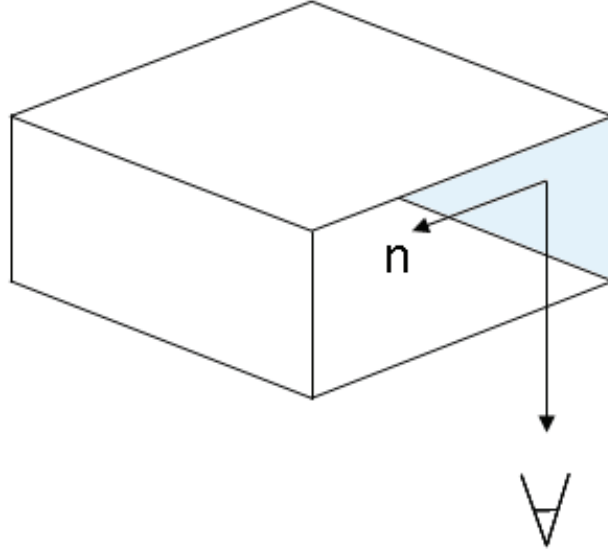


Figure A.3: The geometry of the second simulation is shown. The observer is now at a 45° angle and the reflectance is now $\rho = 0.5$.

A.2 Open Box with Rear Wall Emitting

The second analytical simulation starts with the same two plates as before, however, they are now surrounded by a box. Figure A.3 shows the geometry of this situation. The emitting plate is the rear wall of the box and the reflecting plate is the blue colored wall. The observer has rotated to 45° from normal. The side walls of the box shield the observer from the direct emission of the emitting wall, thus, the only signal that the observer can see is the reflection again, but this time the reflectance of the second plate is $\rho = 0.5$. Thus, the observed intensity contains reflected and self-emitted radiance. The analytical solution is shown in Equations (A.4) and (A.5).

$$I_{e \text{ Self-Emitted}} = \int_{A_{\text{source}}} L_e(T = 300K) \cos(45) dA_s \quad (\text{A.4})$$

$$I_{e \text{ Observed}} = \rho I_{e \text{ Reflected}} + (1 - \rho) I_{e \text{ Self-Emitted}} = 13.7 \left[\frac{W}{sr} \right] \quad (\text{A.5})$$

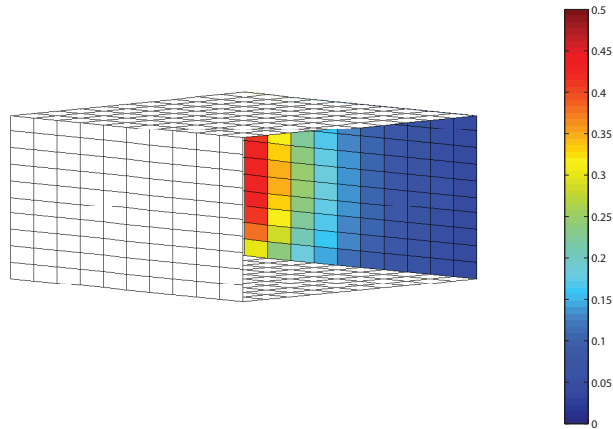


Figure A.4: The result of the open box simulations is shown. In this simulation, the observed intensity is a combination of reflected and self-emitted radiance. Colormap units are $[W/sr]$.

The analytical solution is $13.7 W/sr$ and the computer simulation using the radiosity algorithm is $13.1 W/sr$. Again, the simulation is accurate, 96% in this case. To gain greater accuracy, the number of differential areas must be increased. In this simulation, only 100 areas are calculated.

Appendix B. Blackbody Cavity Source Calculations

This appendix details the analytical calculations necessary to produce Figure 3.33 during the blackbody cavity source simulation.

B.1 s/S Ratios

Table B.1 calculates the s/S ratios for input into Equation (3.12).

B.2 Emissivity Calculations

An example calculation of the analytical emissivity and simulated emissivity, for a specific s/S ratio is included below for clarity. To start, the cavity with four facets removed is chosen for the simulation. The internal emissivity is $\varepsilon = 0.5$, and the equations are taken from Section 4.1. The internal temperature of the cavity is 800 Kelvin.

$$\begin{aligned}
 s &= 0.0487[m^2] \\
 S &= 3.106[m^2] \\
 S_0 &= 4\pi r^2 = 4\pi(0.5)^2 = \pi[m^2] \\
 k &= (1 - \varepsilon) \left[\frac{s}{S} - \frac{s}{S_0} \right] = (1 - 0.5) \left[\frac{0.0487}{3.106} - \frac{0.0487}{\pi} \right] = 8.88 \times 10^{-5} \\
 \varepsilon'_0 &= \frac{\varepsilon}{\varepsilon \left[1 - \frac{s}{S} \right] + \left(\frac{s}{S} \right)} = \frac{0.5}{0.5 \left[1 - 0.0157 \right] + 0.0157} = 0.9845 \\
 \varepsilon_0 &= \varepsilon'_0(1 + k) = 0.9845(1 + 8.88 \times 10^{-5}) = 0.9846
 \end{aligned}$$

Analytically, the emissivity of the cavity should be 0.9846. After the simulations were performed, the emissivity of the cavity was calculated using the observed radiance and the analytical radiance of the aperture. The cavity was set to a temperature of 800K. The following calculates the intensity that should be visible from a perfect blackbody with an aperture, $s = 0.0487m^2$.

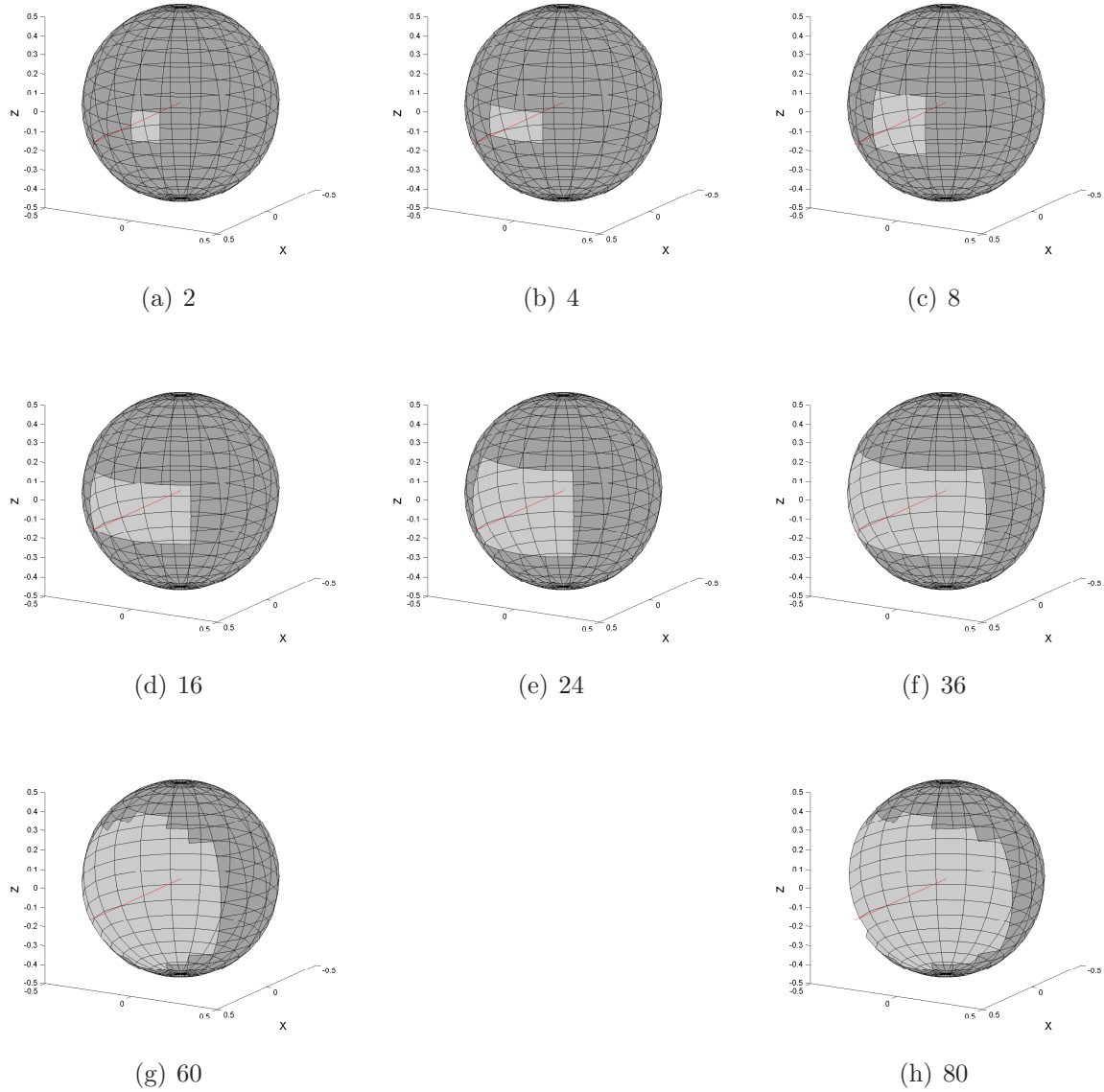


Figure B.1: Eight different aperture sizes were constructed for the simulation, and are displayed above. Each figure shows the size of the aperture in relation to the radius of the cavity, the s/S ratio. The sub-caption for each figure lists how many facets were removed to create the aperture. The line from the center of the cavity is the view direction vector, it starts at the center of the cavity and extends out through the center of the aperture.

Table B.1: Gouffé variables for each of the Blackbody Cavity Simulations.

Removed Facets	$s [m^2]$	$S [m^2]$	$S_0 [m^2]$	s/S
2	0.0244	3.106	π	0.0079
4	0.0487	3.106	π	0.0157
8	0.0963	3.106	π	0.0310
16	0.1926	3.106	π	0.0620
24	0.2820	3.106	π	0.0910
36	0.4240	3.106	π	0.1366
60	0.6540	3.106	π	0.2110
80	0.8749	3.106	π	0.2810

$$\begin{aligned}
 L_{e \text{ BB}} &= \frac{\sigma_e T^4}{\pi} \left[\frac{W}{sr - cm^2} \right] \\
 &= \frac{5.67 \times 10^{-12} \cdot 800^4}{\pi} = 0.7393 \left[\frac{W}{sr - cm^2} \right] \\
 I_{e \text{ BB}} &= L_{e \text{ BB}} \left[\frac{W}{sr - cm^2} \right] \cdot A_{\text{aperture}}[m^2] \cdot 1 \times 10^4 \left[\frac{cm^2}{m^2} \right] \\
 &= 0.7393 \cdot 0.0487 \cdot 1 \times 10^4 \\
 &= 360.04 \left[\frac{W}{sr} \right] \\
 I_{e \text{ Greybody Self Emission}} &= \varepsilon \cdot I_{e \text{ BB}} \\
 &= 0.5 \times 360.04 = 180.02 \left[\frac{W}{sr} \right]
 \end{aligned}$$

A perfect blackbody should be emitting 360.04 $[W/sr]$ on the centerline. From above, the direct emission of a $\varepsilon = 0.5$ greybody should be 180.02 $[W/sr]$, which is the simulation result after zero bounces. After one bounce the viewed intensity from the aperture is 270.54 $[W/sr]$. The ratio of the viewed intensity and the analytical blackbody intensity is the apparent emissivity of the cavity, in this case 0.75. This data point is the second point on the single bounce curve of Figure 3.33.

To complete the rest of the simulations to fill in Figure 3.33, this process is repeated for all combinations of the eight s/S ratios and the four different number of bounces.

Appendix C. Ray Tracing

This appendix demonstrates the technique of *ray tracing*, and how it is used to sample the hemispherical view of each facet. The ray tracing technique is taken from [9,15]. These techniques are the basis of classical computer graphics algorithms, which are used to render artificial scenes from a 3D wireframe.

The propagation algorithm needs to know what model facets are viewable from each of the facets in the wireframe model. To achieve this, the 2D hemisphere is sampled to produce a hemispherical view matrix for each facet. The matrix has a sample every degree in θ and ϕ , making $360 \times 90 = 32400$ samples per facet.

C.1 Wireframe Model Primitives

The wireframe model contains the vertex and normal vector information for every facet. Vertices must be coplanar, which produces a flat surface which creates either a triangle or quadrilateral. The ray tracing algorithm must then be able to calculate intersections with triangles and quadrilaterals.

C.2 Ray Tracing Algorithm

To calculate what facet is visible in a certain direction from a facet, the algorithm must know the starting position and direction of the *sample* ray. Figure C.1 defines the geometry that will be assumed for the description of the ray tracing routine. Three sample rays are also defined in the figure to aid in the description.

Once a sample direction and the starting location (facet A's center) are selected, every other facet must be tested to see if that vector passes through the facet. To do this, the algorithm calculates the intersection between the sample vector (ray) and the infinite plane that the four vertices create. Then, the intersection point is checked to see if it is inside the polygon or not. If so, the distance from facet A's center to the intersected polygon's center is recorded. The next polygon is checked against the sample ray, and the process continues until all polygons are checked for

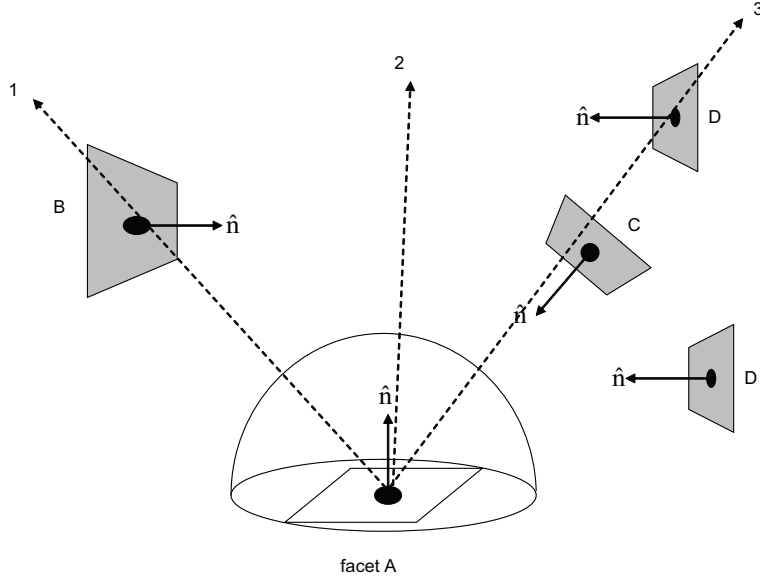


Figure C.1: Three sample rays are drawn to aid in the ray tracing example. The facets found by the rays are facet B, background and facet C for sample rays 1, 2 and 3, respectively.

an intersection. The polygon that has the closest intersection to the parent facet is then the facet that is in view.

For example, sample ray #1 will find facet B. Sample ray #2 will not find any of the model facets, and thus, background will be assigned in that direction. Sample ray #3 is slightly more complex as the piecewise algorithm will find facets C and D. Clearly facet C is the closest and should be assigned to this ray. The algorithm calculates the distance to each facet and chooses the closest one, facet C.

This process is repeated for each facet in the model and creates a data structure where the hemispherical view for each facet as a function of θ and ϕ is indexed against the other facets. The variable names are `geomFile` for the model facets and `bgGeomFile` for the background facets. This precalculation creates a simple lookup table that the algorithms evaluate when sampling or integrating the hemisphere to allow the simulation to render a solution faster. This process is the most demanding computational process in the simulation.

Bibliography

1. *Federal Standard 595 Rev B - Colors Vol 1 (FED-STD-595)*. 1989.
2. Beercroft, M. T., J. T. Neu, and J. Jafolla. “Bidirectional reflectance data to support paint development and signature calculations”. R. P. Breault (editor), *Stray radiation in optical systems II; Proceedings of the Meeting, San Diego, CA, July 20-22, 1992 (A93-55176 24-74)*, p. 304-316., 304–316. February 1993.
3. Bortle, Capt Jonathan. *A Measurement- and Prediction-Based Validation of the AFIT Large Commercial Aircraft Infrared Trend Analysis Tool*. Master’s thesis, Graduate School of Engineering and Management, Air Force Institute of Technology (AETC), Wright-Patterson AFB, OH, March 2006. AFIT/GE/ENP/06-01.
4. Dereniak, E L and G D Boreman. *Infrared Detectors and Systems*. Wiley Interscience, 1996.
5. Dutre, Philip, Kavita Bala, and Philippe Bekaert. *Advanced Global Illumination*. A. K. Peters, Ltd., Natick, MA, USA, 2002. ISBN 1568811772.
6. Evans, M and T Swartz. *Approximating Integrals via Monte Carlo and Deterministic Methods*. Oxford University Press, 2000.
7. Forrai, David P. and James J. Maier. “Generic models in the advanced IRCM assessment model”. *WSC '01: Proceedings of the 33rd conference on Winter simulation*, 789–796. IEEE Computer Society, Washington, DC, USA, 2001. ISBN 0-7803-7309-X.
8. Gallo, L., B. Barrat, S. Berthier, N. Cambou, and G. Schalow. “Open-ended tools for IR sensors, scenes, and systems design”. *Proc. SPIE Vol. 4130, p. 587-600, Infrared Technology and Applications XXVI, Bjorn F. Andresen; Gabor F. Fulop; Marija Strojnik; Eds.*, 587–600. December 2000.
9. Glassner, Andrew. *An Introduction to Ray Tracing*. Academic Press Ltd., 1989.
10. Goral, Cindy M, Kenneth E Torrance, Donald P Greenberg, and Bennett Battaille. “Modeling the Interaction of Light Between Diffuse Surfaces”. *Computer Graphics*, 18(3):10, July 1984.
11. Gouffé, Andre. “Corrections d’Ouverture des Corps-noir Artificiels Compte Tenu des Diffusions Multiples Internes”. *Revue d’Optique*, Vol. 24, 1945.
12. He, Xiao D, Kenneth E Torrance, François X Sillion, and Donald P Greenberg. “A comprehensive physical model for light reflection”. *SIGGRAPH Comput. Graph.*, 25(4):175–186, 1991. ISSN 0097-8930.
13. Hines, N R and D N Mavris. “A Parametric Design Environment for Including Signatures Analysis in Conceptual Design”. *5th World Aviation Congress and Exposition, San Diego, CA*. 2000.

14. Klein, C. A. "How infrared missile windows degrade the noise-equivalent irradiance of infrared seeker systems". *Proc. SPIE Vol. 2286, p. 458-470, Window and Dome Technologies and Materials IV, Paul Klocek; Ed.*, 458–470. September 1994.
15. Lindley, Craig. *Practical Ray tracing in C*. Wiley, 1992.
16. Mahulikar, S P, G A Rao, and P S Kolhe. "Infrared Signatures of Low-Flying Aircraft and Their Rear Fuselage Skins Emissivity Optimization". *Journal of Aircraft, Vol. 43, No. 1, JanuaryFebruary 2006*. 2006.
17. Martinez, Capt Ruben. *Modeling the Infrared Intensity of a Large Commercial Aircraft*. Master's thesis, Graduate School of Engineering and Management, Air Force Institute of Technology (AETC), Wright-Patterson AFB, OH, March 2005. AFIT/GE/ENP/05-01.
18. Maxwell, J, J Beard, S Weiner, and D Ladd. *Bidirectional reflectance model validation and utilization*. Technical Report AFAL-TR-73-303, Environmental Research Institute of Michigan (ERIM), October 1973.
19. US Navy, Naval Air Warfare Center Weapons Division. *Electronic Warfare and Radar Systems Engineering Handbook*. TP9347, 2002.
20. Nicodemus, F E, J C Richmond, J J Hsia, I W Ginsberg, and T Limperis. *Geometrical considerations and nomenclature for reflectance*. NBS Monograph 160, National Bureau of Standards, Washington, D.C., October 1977.
21. Rao, G A and S P Mahulikar. "Effect of Atmospheric Transmission and Radiance on Aircraft Infrared Signatures". *Journal of Aircraft 2005, Vol.42 No.4, p.1046-1054*. 2005.
22. Rao, G A and S P Mahulikar. "New criterion for aircraft susceptibility to infrared guided missiles ". *Aerospace Science and Technology, Volume 9, Issue 8 , November 2005, Pages 701-712*. 2005.
23. Sandford, Brian P and David C Robertson. *Infrared Reflectance Properties of Aircraft Paints*. Technical report, Philips Laboratory, Geophysics Directorate/G-POA, August 1994.
24. Thomas, D. J., J. C. Jafolla, and P. J. Sarman. "Bidirectional reflectance measurements for high-resolution signature modeling". *Proc. SPIE Vol. 3062, p. 105-116, Targets and Backgrounds: Characterization and Representation III, Wendell R. Watkins; Dieter Clement; Eds.*, 105–116. June 1997.
25. Trowbridge, T S and K P Reitz. "Average Irregularity of a Rough Surface for Ray Reflections". *J Opt. Soc. Am.*, 65(531), 1975.
26. Wolfe, W and G J Zissis. *The Infrared Handbook*. Environmental Research Institute of Michigan, Ann Arbor, MI., 1995.

Index

This index lists the page where the item is introduced or defined.

- A340-300, 79, 98
- alpha angle, 17
- angle of attack, 82
- atmospheric transmission, 26

- background, 57
- blackbody, 6
- Blender3D, 36
- BRDF, 8

- cavity source, 38, 76, 84
- center, 34
- contrast detection, 80
- coplanar, 34
- cylinder model, 39

- diffuse reflectance, 13
- dimensionality reduction, 9

- emissivity, 7

- facet type, 35
- flight path, 82
- FOV, 33
- fractional specularity, 14

- geometry sampling, 55
- glideslope, 82
- glint angle, 17
- glint vector, 17

- hemispherical integration, 31
- hemispherical view, 44

- ILS, 82

- importance sampling, 50
- infrared signature, 33
- IR Range, 57
- IR Range simulation, 86

- Kirchoff, 6

- lessons learned, 117
- long wave infrared, 18

- material type, 35
- memory considerations, 76
- Method of Gouffé, 77
- mid wave infrared, 18
- MODTRAN, 27
- Monte Carlo integration, 27
- Monte Carlo Method, 52

- normal, 34
- numerical quadrature, 27

- positive vector, 35

- radiometry, 7
- radiosity, 70
- ray tracing, 128
- reciprocity, 10
- recommendations, 118
- reference vector, 34
- reflectance, 7
- reflectance distributions, 12
- rejection sampling, 52

- s/S ratio, 124
- Sandford-Robertson, 15

sky, 63
SNR, 33
specular reflectance, 12
spherical geometry, 30
stratified numerical quadrature, 54
surface isotropy, 10

temperature, 36
terrain, 59

wavelength, 10
wireframe model, 34
world sphere, 58

REPORT DOCUMENTATION PAGE

Form Approved
OMB No. 0704-0188

The public reporting burden for this collection of information is estimated to average 1 hour per response, including the time for reviewing instructions, searching existing data sources, gathering and maintaining the data needed, and completing and reviewing the collection of information. Send comments regarding this burden estimate or any other aspect of this collection of information, including suggestions for reducing this burden to Department of Defense, Washington Headquarters Services, Directorate for Information Operations and Reports (0704-0188), 1215 Jefferson Davis Highway, Suite 1204, Arlington, VA 22202-4302. Respondents should be aware that notwithstanding any other provision of law, no person shall be subject to any penalty for failing to comply with a collection of information if it does not display a currently valid OMB control number. **PLEASE DO NOT RETURN YOUR FORM TO THE ABOVE ADDRESS.**

1. REPORT DATE (DD-MM-YYYY) 22-03-2007		2. REPORT TYPE Master's Thesis		3. DATES COVERED (From — To) Aug 2006 — Mar 2007	
4. TITLE AND SUBTITLE A Study of Bi-Directional Reflectance Distribution Functions and Their Effect on Infrared Signature Models				5a. CONTRACT NUMBER	
				5b. GRANT NUMBER	
				5c. PROGRAM ELEMENT NUMBER	
				5d. PROJECT NUMBER	
6. AUTHOR(S) Samuel I Harkiss, Flight Lieutenant, RAAF				5e. TASK NUMBER	
				5f. WORK UNIT NUMBER	
				8. PERFORMING ORGANIZATION REPORT NUMBER AFIT/GE/ENP/07-01	
7. PERFORMING ORGANIZATION NAME(S) AND ADDRESS(ES) Air Force Institute of Technology Graduate School of Engineering and Management 2950 Hobson Way WPAFB OH 45433-7765				10. SPONSOR/MONITOR'S ACRONYM(S) AFRL/SNS	
9. SPONSORING / MONITORING AGENCY NAME(S) AND ADDRESS(ES) AFRL/SNS Bldg 254, 2951 K Street Wright-Patterson AFB, OH 45433-7765				11. SPONSOR/MONITOR'S REPORT NUMBER(S)	
				12. DISTRIBUTION / AVAILABILITY STATEMENT APPROVED FOR PUBLIC RELEASE; DISTRIBUTION UNLIMITED.	
13. SUPPLEMENTARY NOTES					
14. ABSTRACT Since 2004, AFIT has been developing a trend-analysis tool to assess large commercial aircraft infrared (LCAIR) signatures. In many cases, this code predicted signatures to within 10% of measured data. However, other results indicated that the single-bounce, specular-reflection algorithm being used failed to adequately simulate interactions between aircraft parts where either the specular component is dominated by diffuse reflection or part-to-part multiple-bounce reflections contribute significantly to the signature; discrepancies greater than 100% were observed. This research incorporates Bi-Directional Reflectance Distribution Functions (BRDF's) and multiple-bounce calculations into the LCAIR model. A physical aircraft model was constructed from aluminum, and measurements were taken before and after a surface treatment in gloss black paint. The Sandford-Robertson model is used to parameterize the BRDF's of both the bare aluminum and gloss black paint. Since the most efficient method of integrating a BRDF depends upon the reflectance distribution of the aircraft material, the sampling resolution of the BRDF integral is crucial to an accurate simulation. Additionally, care is taken to ensure that the integration of the hemispherical irradiance onto each facet of the computational model is sampled at a sufficient resolution to achieve convergence in the solution.					
15. SUBJECT TERMS BRDF, Bi-Directional Reflectance Distribution Function, Infrared Radiation, Infrared Imaging, Signature Modeling, Infrared Measurement, Propagation Algorithms, Computer Graphics, Wireframe.					
16. SECURITY CLASSIFICATION OF:			17. LIMITATION OF ABSTRACT UU	18. NUMBER OF PAGES 153	19a. NAME OF RESPONSIBLE PERSON Dr. Michael A. Marciniak, AFIT/ENP
a. REPORT U	b. ABSTRACT U	c. THIS PAGE U			19b. TELEPHONE NUMBER (include area code) (937) 255-3636, ext 4529